Synthetic Air Data Estimation

A case study of model-aided estimation

A DISSERTATION
SUBMITTED TO THE FACULTY OF THE GRADUATE SCHOOL
OF THE UNIVERSITY OF MINNESOTA
BY

F. Adhika Pradipta Lie

IN PARTIAL FULFILLMENT OF THE REQUIREMENTS
FOR THE DEGREE OF
DOCTOR OF PHILOSOPHY

Demoz Gebre-Egziabher, Adviser

September 2014

Acknowledgements

First and foremost, I thank my adviser, Prof. Demoz Gebre-Egziabher, for his guidance and support for the past five years. He allowed me to direct my research in the areas that interest me, infected me with his passions, and above all believed in me. This has made my Ph.D process both fruitful and enjoyable. I also thank Prof. Gary Balas, Prof. Peter Seiler, and Prof. Rajesh Rajamani for their insightful comments during my preliminary oral exam and sitting in my thesis committee.

Being a part of the University of Minnesota's Unmanned Aerial Vehicle laboratories was one of the most rewarding aspect of my thesis work. Special thanks to Brian Taylor, Will Johnson, Arion Mangio, and Danny Chryst for their help in the flight test campaign. Their camaraderie has made flight testing in the frigid Minnesota winter fun and enjoyable. My gratitude also goes to the rest of my colleagues at the UAV lab, in particular Curt Olson, Austin Murch, Karen Hamidun, John Jackson, David Escobar, Janos Polgar, Paw Yew Chai, and Andrei Dorobantu.

I thank my friends at the Navigation lab, past and present, for their friendship, and unique perspective and experience: Hamid Mokhtarzadeh, Trevor Layh, Andrew Stewart, Jordan Larson, Jason Chu, Zhefeng Li, and Guijin Zheng. I owe special thanks to Hamid Mokhtarzadeh. Hamid's collaboration was instrumental in devising a carrier phase differential GPS system we use at the lab. He helped me to keep my sanity in check whenever things got rough and frustration grew high.

My research has been partially funded by the University of Minnesota's Center for Transportation Studies, Department of Homeland Security under grant number 2008-ST-061-BS0002, and the University of Minnesota Doctoral Dissertation Fellowship. Any opinions, findings, and conclusions or recommendations expressed in this thesis are mine and do not necessarily reflect the views of these organizations. Their support is gratefully acknowledged.

I owe a debt of gratitude to my friends: Kim and Eric Kroetsch, Anthony Kho, Randy Hidayat, Kelsen Bastari, Hans Pramudita, Anthony Lie, and Astrini Sie. They

are my source of strength and inspiration, and I am blessed to have them in my life. Indeed, the next best thing to being wise oneself is to live in a circle of those who are. Finally, my deepest thanks go to my parents, Irawan and Siska, and my sister, Citta. Their unending support and encouragement have been invaluable throughout my life. It is to them, with heartfelt thanks, that I dedicate this thesis.

Abstract

A method for estimating airspeed, angle of attack, and sideslip without using conventional, pitot-static airdata system is presented. The method relies on measurements from GPS, an inertial measurement unit (IMU) and a low-fidelity model of the aircraft's dynamics which are fused using two, cascaded Extended Kalman Filters. In the cascaded architecture, the first filter uses information from the IMU and GPS to estimate the aircraft's absolute velocity and attitude. These estimates are used as the measurement updates for the second filter where they are fused with the aircraft dynamics model to generate estimates of airspeed, angle of attack and sideslip. Methods for dealing with the time and inter-state correlation in the measurements coming from the first filter are discussed. Simulation and flight test results of the method are presented. Simulation results using high fidelity nonlinear model show that airspeed, angle of attack, and sideslip angle estimation errors are less than 0.5 m/s, 0.1 deg, and 0.2 deg RMS, respectively.

Factors that affect the accuracy including the implication and impact of using a low fidelity aircraft model are discussed. It is shown using flight tests that a single linearized aircraft model can be used in lieu of a high-fidelity, non-linear model to provide reasonably accurate estimates of airspeed (less than 2 m/s error), angle of attack (less than 3 deg error), and sideslip angle (less than 5 deg error). This performance is shown to be relatively insensitive to off-trim attitudes but very sensitive to off-trim velocity.

Contents

List of Tables vii

List of Figures viii

1 Introduction 1

1.1 Air Data System . . . 2
1.2 Air Data System Failure . . . 6
1.3 Significance of Model-based Air Data System . . . 8
1.4 Thesis Contribution . . . 9
1.5 Thesis Organization . . . 10

2 Non-traditional Air Data Systems 11

2.1 Overview . . . 11
2.2 Ultrasonic Airspeed Sensors . . . 12
2.3 Laser-based Air Data Systems . . . 13
2.4 Model-based Air Data Systems . . . 15
2.4.1 Prior Art . . . 16
2.4.2 Challenges with Model-based Systems . . . 19
2.5 Summary . . . 21

3 Synthetic Air Data Systems 22

3.1 Basics of Synthetic Air Data Estimation . . . 22
3.2 Aircraft Dynamic Model . . . 26
3.2.1 Nonlinear Aircraft Dynamics . . . 27

3.2.2 Linear Aircraft Dynamics 34
3.3 Wind Model 43
3.4 Summary 44

4 Filter Architectures **45**
4.1 Single Filter Architecture 45
4.2 Federated Filter Architecture 50
4.3 Architecture Validation 55
4.4 Summary 62

5 Experimental Validation **63**
5.1 Flight Test Setup 63
5.2 Nominal Filter Performance 65
5.3 Limitation 70

6 Conclusion **73**
6.1 Conclusion 73
6.2 Future Work 74

A Simulation Model **76**
A.1 Force and Moment Coefficient Model 76
A.2 Cessna 172 Properties 77

B Nonlinear Dynamics Covariance Propagation Model **78**
B.1 Jacobian matrix 78
B.2 Noise Shaping matrix 80
B.3 Aerodynamic derivatives 81

C Linear Dynamics Covariance Propagation Model **82**
C.1 Jacobian matrix 82
C.2 Noise Shaping matrix 83

D Ultra Stick 120 Model **85**
D.1 Aircraft's Geometry 85

D.2 Propeller Model 85
D.3 Trim Condition 86
D.4 Stability Derivatives 86

E Flight Test Results **87**
E.1 Ibis Flight 18 87
E.2 Ibis Flight 26 89

Bibliography **92**

List of Tables

1.1 Examples of aircraft accidents that have been caused by air data system failure 6

4.1 Simulation Maneuvers 58

A.1 Simulated Cessna 172 Aerodynamic Parameters 77
A.2 Physical and Geometric Properties of Simulated Cessna 172 77

D.1 Physical and Geometric Properties of Ultrastick 120 85
D.2 Identified Stability Derivatives 86

List of Figures

1.1 Airspeed vector components in the aircraft's body axes 2
1.2 Air data sensor arrangement on an Airbus A350XWB. (Photo courtesy of Benny Zheng) 4
1.3 Airspeed Algorithm 4
1.4 Five hole pitot tube on a 5-16A 5
1.5 A schematic of Airbus A330 air data system [1] 7

2.1 Single axis ultrasonic air data sensor 12
2.2 Laser-based air data system in [2] 14
2.3 Simulated performance of Zeis Angle of Attack Estimator 17
2.4 Complementary filter used in [3, 4] 17
2.5 Wise's Computational α/β system 20
2.5(a) 20
2.5(b) 20

3.1 The wind triangle 23
3.2 Synthetic air data system formulated as an error state Kalman filter . 24
3.3 Thrust line 28
3.4 First-order Gauss Markov Process 40

4.1 Single filter architecture for synthetic air data estimation 46
4.2 Federated filter architecture for synthetic air data estimation 51
4.3 Simulation trajectory depicting position and airspeed correlation . . . 56
4.3(a) 56

4.3(b) . . . 56
4.3 Simulation Trajectory . . . 57
4.3(c) . . . 57
4.3(d) . . . 57
4.4 Accuracy of air data estimates using single filter architecture . . . 60
4.5 Accuracy of air data estimates with a high quality IMU ($\sigma_{\text{Accel}} = 0.5$ mg) and a high fidelity dynamic model . . . 61
4.6 Performance of the federated architecture . . . 61
4.7 Sensor quality and filter architecture . . . 62

5.1 Ultra Stick 120 Testbed: Airframe 5.1(a), aerodynamic angle vane 5.1(b) 64
5.1(a) . . . 64
5.1(b) . . . 64
5.2 Performance of the synthetic air data estimator . . . 67
5.3 Performance of the synthetic air data estimator during steep turns. Flight description can be found on Appendix E.1 . . . 68
5.4 Improved filter performance during steep turns . . . 69
5.5 Accuracy of the air data estimate is bad at large deviation from trim airspeed (highlighted region). Flight description can be found on Appendix E.2 . . . 71
5.6 Angle of attack vs. Airspeed sensitivity . . . 72

E.1 Flight 18 North-East plane trajectory . . . 87
E.2 Flight 18 airspeed, angle of attack, and sideslip history . . . 88
E.3 Flight 18 roll, pitch, and yaw history . . . 88
E.4 Flight 26 North-East plane trajectory . . . 89
E.5 Flight 18 airspeed, angle of attack, and sideslip history . . . 90
E.6 Flight 18 roll, pitch, and yaw history . . . 90

Chapter 1

Introduction

Using feedback loop to control the behavior of a system is one of the foundations for automatic control. It works by comparing the current state of the system with the desired state and based on that take appropriate actions to steer the system towards the goal. For this reason, accurate feedback is crucial to control a system efficiently. The feedback mechanisms come from an estimator or an observer. The observer or estimator uses sensor measurements to estimate the system's state. Unfortunately, information collected from sensor measurements is always corrupted with errors or noise which could limit the performance that can be attained by the control system.

Model-aided estimator is one method that has been proposed to improve the performance of estimators. It is very attractive in applications where size, weight, power, and cost limit the number of sensors that can be carried on board. In the field of aircraft navigation, [5,6] are two seminal works that studied the feasibility of using an aircraft dynamic model, namely the aircraft's equations of motion (EOM) to aid an inertial navigation system (INS). Those papers showed using simulation that an aircraft dynamic model could indeed aid the long term stability of the INS outputs.

This thesis deals with the problem of designing a model-based air data system which outputs estimate of the aircraft's speed and orientation relative to the air mass in which it is flying. These quantities define the aircraft's air relative velocity vector, denoted $\mathbf{V}_{WB}$. They are alternatively described by three parameters: Airspeed (V), angle of attack (α), and sideslip angle (β).

Because they determine the performance of an airplane in flight, an accurate

estimate of V, α, and β is key to efficient and safe operation of aircraft regardless whether they are being operated by a human pilot or an automatic control system. For example, airspeed is used to define the minimum speed for safe operation (stall speed) and the maximum speed beyond which aircraft structural damage can occur. Angle of attack and sideslip measurements are used to ensure an airplane does not operate in a region from which recovery from a flight upset is not possible.

This chapter will motivate the work reported in this dissertation. Section 1.1 describes what an air data system is, followed by Section 1.2 which explains why we need a reliable non-pitot/static/vane-based air data system. The significance of a model-based air data system is presented in Section 1.3. Finally, we close this chapter by highlighting our contributions.

1.1 Air Data System

Airspeed, angle of attack and sideslip angle are an important subset of variables used to define the boundaries of the aircraft's flight envelope. They describe the aircraft's velocity vector relative to the air mass in which it is flying.

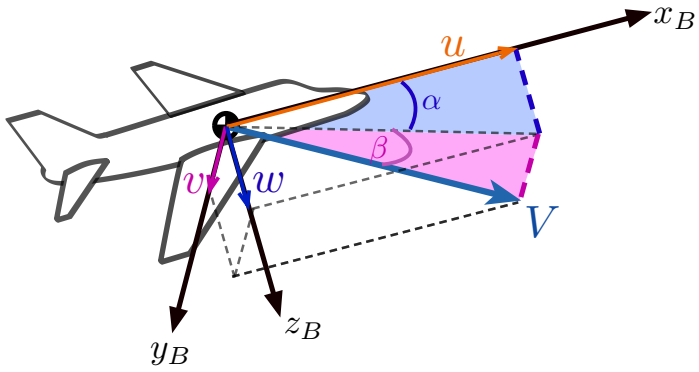

Figure 1.1: Airspeed vector components in the aircraft's body axes

Figure 1.1 depicts V, α, β and their relations to the aircraft's body frame, F_B. Let $\mathbf{V}_{WB}^{B}$ denote the resolution of $\mathbf{V}_{WB}$ on F_B with components:

$$\mathbf{V}_{WB}^{B} = \begin{bmatrix} u & v & w \end{bmatrix}^T \tag{1.1}$$

1.1. Air Data System

Angle of attack is defined as the angle between the x-component of $\mathbf{V}_{WB}^{B}$ and the vector's projection on the xz-plane or mathematically:

$$\alpha = \tan^{-1} \frac{w}{u} \tag{1.2}$$

Sideslip angle is defined as the angle between the projection of $\mathbf{V}_{WB}^{B}$ on the xz-plane and the vector itself, or:

$$\beta = \sin^{-1} \frac{v}{V} \tag{1.3}$$

Finally, airspeed is the magnitude of $\mathbf{V}_{WB}$, that is:

$$V = \sqrt{u^2 + v^2 + w^2} \tag{1.4}$$

The air data triplets are measured using an air data system that typically features a pitot/static system and mechanical vanes such as depicted in Figure 1.2. Assorted piping connects the pressure taps on the pitot tube and static ports to pressure transducers that, in turn, send signals to an air data computer.

A generic functional block diagram of airspeed estimation from pitot/static measurement system is shown on Figure 1.3. The Mach number is calculated using:

$$M = \sqrt{5 \left[\left(\frac{p_t - p_0}{p_0} + 1 \right)^{\frac{2}{7}} - 1 \right]} \tag{1.5}$$

where p_t and p_0 are the pitot and static pressure, respectively. A certified air data system needs to satisfy the accuracy requirements specified in [7] which requires compensating the pitot and static pressure measurements for errors due to local flow effect at their respective locations. The correction depends on the Mach number and the position of the sensor on the fuselage and it is obtained through an extensive testing and calibration process.

The angle of attack and sideslip vanes are free to rotate so they are aligned with the local flow direction. Because the sideslip vanes are usually constrained from rotating about the aircraft's y-axis, their measurements should be corrected to obtain the actual sideslip angle. When a sideslip vane is constrained to measure the angle

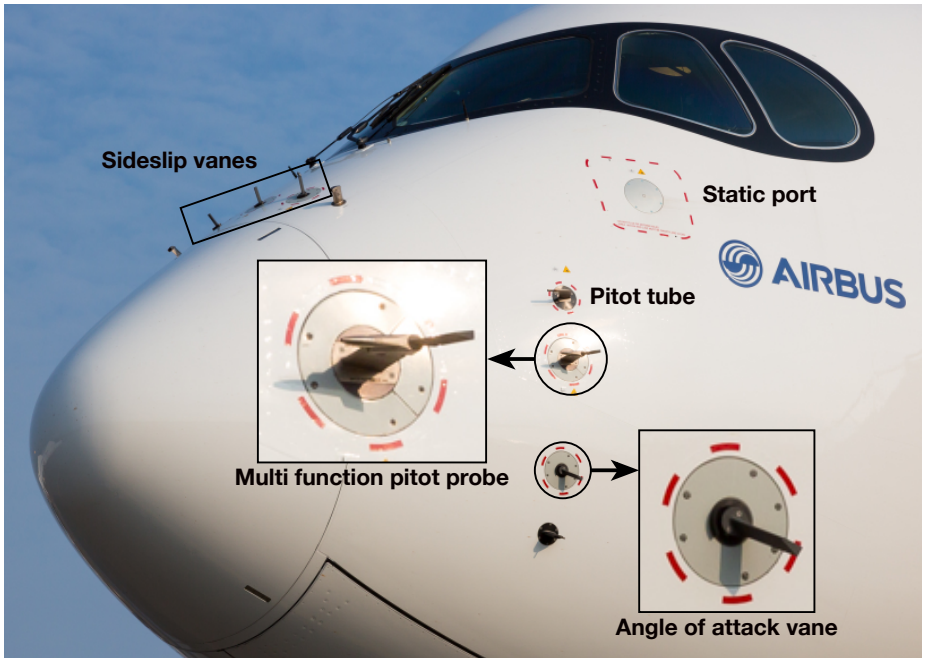

Figure 1.2: Air data sensor arrangement on an Airbus A350XWB. (Photo courtesy of Benny Zheng)

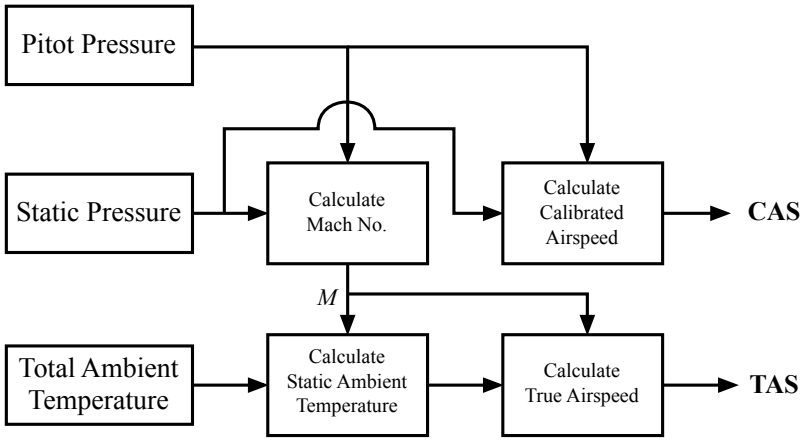

Figure 1.3: Airspeed Algorithm

on the xy-plane instead, the output is called the flank angle, β_f. Sideslip angle is obtained by using the following equation:

$$\tan\beta = \cos\alpha \tan\beta_f \tag{1.6}$$

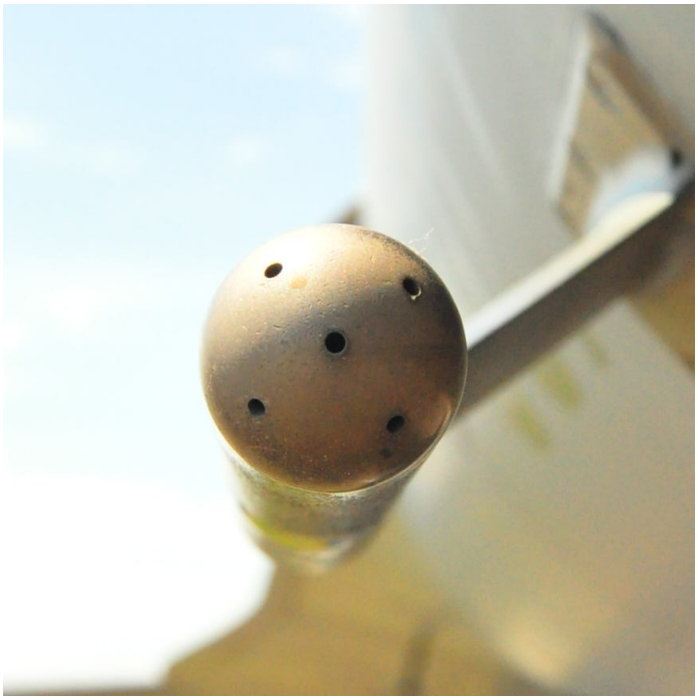

Figure 1.4: Five hole pitot tube on a 5-16A

Some variant architectures of the air data system exist and have been used in modern airplanes. A multi function pitot probe [8] like the one shown on Figure 1.2 has a pitot tube, static port, and angle of attack vane in a single unit. The five-hole pitot tube shown on Figure 1.4 is another example of a variation which combines multiple functions into one device. Angle of attack and sideslip angle are calculated using pressure difference from multiple pressure taps [9].

Recently, there are a number of products that give pilots color-coded display of the α zone they are flying at [10–12]. These products are targeted for small airplanes and uses pressure differential to determine the α regime (not the value) the airplane is flying at. These sensors work independently from the exisiting air data system on the airplane and they require post-installation calibration prior to usage. The price of one of these systems is as low as US$200 for the unheated version and US$450 for the heated version [11]. On July 2014, one set of Garmin's angle of attack indicator costs US$1,649.00. ICON Aircraft, a consumer sport plane manufacturer based in Los Angeles, includes this type of angle of attack indicator on its A5 aircraft design [13].

1.2 Air Data System Failure

A malfunctioning air data system can have severe consequences on the safety of flight. As shown on Table 1.1, one of the most often encountered fault mode on an air data system is pitot tube blockage which is often caused by ice accumulation. Moisture and foreign objects like insect nests could also cause blockage in the pitot/static system so, the pitot tube is covered when the aircraft is on the ground for an extended amount of time. To prevent inflight ice accumulation inside the pitot tube, it is usually equipped with a heating element. A small drain hole at the back of the pitot tube allows moisture to drain from the system.

Date	Type	Flight	Probable Cause	Result
Dec 1, 1974	B727	Northwest Orient 6231	Pitot icing	LOC, total fatalities
Jul 28, 1984	LJ25	N1JR	Pitot cover not removed	RTO, hull loss
Feb 6, 1996	B752	Birgen Air 301	Pitot blocked by wasp nest	LOC, total fatalities
Oct 2, 1996	B752	Aero Peru 603	Static port blockage	LOC, total fatalities
Oct 7, 2008	A330	Qantas 72	Temporary Data spikes	Multiple injuries
Nov 27, 2008	A320	XL 888T	Frozen α vane	LOC, total fatalities
Jun 1, 2009	A330	Air France 447	Pitot icing	LOC, total fatalities

LOC: Loss of Control, RTO: Rejected Take Off

Table 1.1: Examples of aircraft accidents that have been caused by air data system failure

When there is an excessive amount of ice in the pitot tube, the heating element might not be able to remove the ice accumulation completely. In this situation, the obstruction would cause erroneous total pressure measurement p_t. If the drain hole remains clear, the pressure inside the pitot tube will start to equalize with the static ambient air pressure. In this situation, the airspeed estimate will become very low because p_t is approximately p_0. While the apparent loss of airspeed is not instantaneous, it does happen relatively quickly [14, Ch. 7]. On the other hand, if both the drain hole and the pitot tube are completely blocked, p_t will remain constant and how the airspeed varies depends on the vertical movement of the aircraft. As the aircraft climbs, p_0 decreases resulting in increase in airspeed estimate, and vice versa. In the former case, this can lead to inadvertent stall because the pilot would react by increasing the angle of attack to reduce the apparent increase in airspeed.

1.2. Air Data System Failure

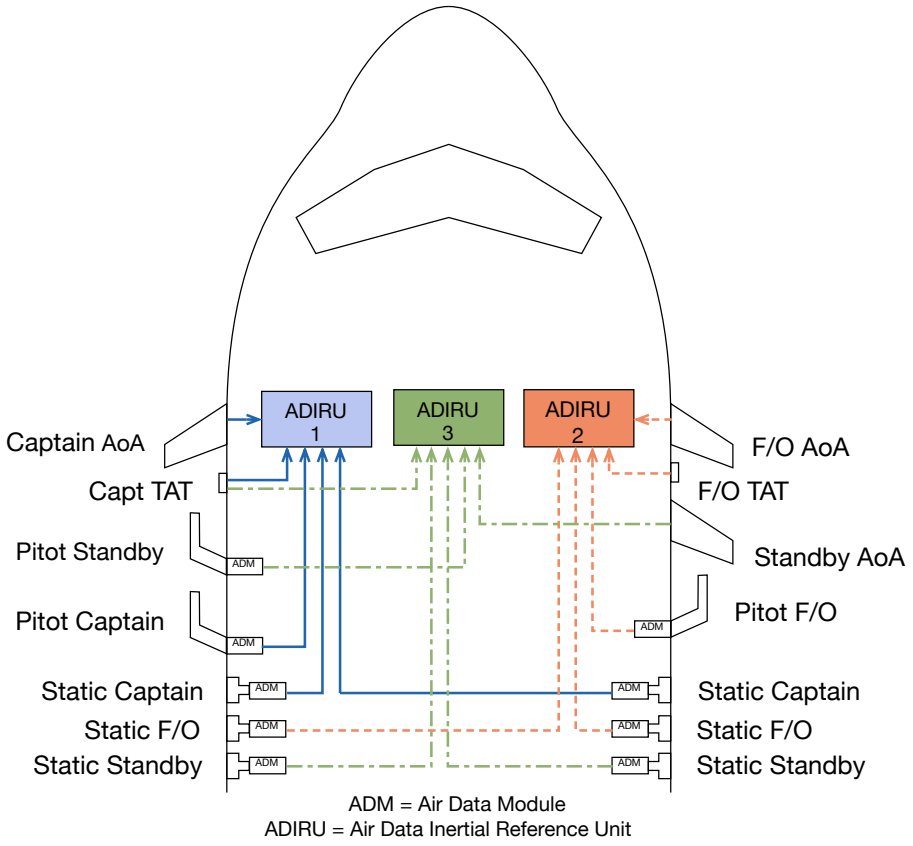

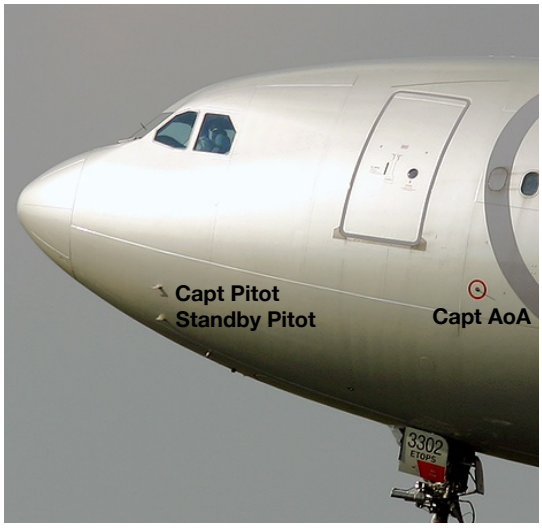

Photo Courtesy of Aart Langevoort

Photo Courtesy of Ron Baak

Figure 1.5: A schematic of Airbus A330 air data system [1]

From the general aviation perspective, aerodynamic stall that results in loss of control of the airplane has been the major cause of mishaps. Data from the National Transportation Safety Board shows that there have been 1,190 fatal accidents in the last 10 years caused by loss of control [15]. On February 5, 2014 FAA streamlined the design approval requirements to install angle of attack indicator on small aircraft which allows aircraft owners to install a non-certified supplemental angle of attack system as long as it is operated as an independent and stand-alone system [16]. It is believed that this new, streamlined process could reduce loss of control type of accidents in general aviation by 40%.

It is clear now that a reliable air data system is key to ensure an aircraft flies within the safe flight enevlope. Currently, the approach used to achieve the required level of reliability is through extensive physical redundancy on sensors, actuators, and flight computers. The Airbus A330, for instance, has an air data system that is triply redundant. As shown in Figure 1.5, each air data computer (denoted ADIRU which is an acronym for Air Data and Inertial Reference Unit) is completely independent from the others and could be used to control the airplane.

1.3 Significance of Model-based Air Data System

The recent interest in small, uninhabited aerial vehicles (UAVs) and the potential of operating them in the national airspace system (NAS) have given rise to an interest in how to design a low cost and highly reliable avionics. This is motivated by the need to develop avionics which meets the size, weight and power (SWAP) constraints of UAVs. For example, the use of triply redundant avionics is not always possible in these small vehicles, so the idea of analytical redundancy has received some attention. Analytical redundancy is a term used to describe the idea of replacing physical hardware with analytical models in multiple-redundant, safety critical systems [17]. A low-cost device or method capable of making reliable estimates of these three air data quantities, namely V, α, and β is highly desirable in its own right. Not only it is useful for SWAP constrained applications such as unmanned aerial system (UAS), but it is also very attractive for cost-sensitive applications such as general aviation.

The enablers of a low-cost solution to airdata estimation are inexpensive sensors and powerful computers which allow real-time sensor fusion. The result of this is a statistical blending of information from different sensors to generate optimum unbiased estimates of the desired quantities. The work reported here uses this technique to provide a low-cost synthetic estimate of V, α, and β from an inertial measurement unit (IMU) and a global positioning system (GPS) receiver. The independence of this system from the conventional airdata system allows a great number of potential applications. For example, aside from providing a back up to the primary airdata computers, this synthetic estimate can also enhance fault detection and isolation in the event of a failure in the primary or traditional airdata system.

1.4 Thesis Contribution

The contribution of our research is twofold. Firstly, it introduced a more realistic approach to model dynamic model uncertainty in a model-based estimator setting, as opposed to ignoring model uncertainty or assuming the error to be white. Secondly, we successfuly designed a model-based air data estimator that could complement the existing system for added redundancy. The estimator is validated using both simulation and flight test data.

Specific to the latter contribution, this work provides:

1. A completely independent air data system that is formulated in a formal estimation framework,

2. Design guidelines for selecting the appropriate estimator architecture given the quality of the sensor used,

3. Practical considerations that should be taken into account when using low fidelity dynamic model to do air data estimation.

The formulation of the designed system allows direct estimation of the output's uncertainty through the covariance matrix. This has the potential to enhance other work in fault detection and isolation area.

1.5 Thesis Organization

This dissertation is organized as follows. Chapter 2 contains a brief survey of alternative air data systems that could be used to enhance the existing system's reliability. Next, an overall description of the proposed synthetic air data system is provided in Chapter 3. Chapter 4 describes two different filter architectures that could be used to mechanize the synthetic air data system. This chapter shows how the quality of the sensor components drives the decision on which architecture to use. The results presented in this chapter is verified using simulation. Finally, the estimator is validated using flight test data. Chapter 5 describes the flight test setup and validation results. Finally, Chapter 6 concludes this dissertation and describes some future works in this area.

Chapter 2

Non-traditional Air Data Systems

This chapter presents an overview of some non-traditional air data systems. This serves as a basis for comparing the main contribution of this thesis; software based solution which will be described in more details in Chapters 3 and 4.

2.1 Overview

The aviation industry and government regulating agencies continuously seek ways to improve the accuracy and reliability of air data systems. Special attention is made to ensure that they are fault tolerant. A very recent accident involving an Airbus A330-200 operated as Air France Flight 447 shows that the current architecture is still prone to external common mode failures like icing [18]. Multiple pitot tube failures on Flight 447 presented the pilots with confusing air data information that eventually led to irrecoverable stall condition.

Investigations following the Flight 447 accident have convinced researchers that a new approach to air data system redundancy is required. This is motivated by studies like the one in [19] which shows that there are changes in upper atmosphere weather patterns which portend more frequent inflight icing encounters. This indicates the need for a new certification standard and novel fault detection techniques to prevent accidents like Flight 447 from happening again. NASA Glenn Research Center, for example, is pursuing a hardware solution to detect pitot tube obstructions through small business innovation research funds with Analysis Measurement

Services Corporation of Knoxville, Tenn. [20].

In most current architectures, faults are detected using an algorithm that would vote out the malfunctioning sensor. In the case of a common mode failure that affects multiple system like that of Flight 447, the algorithm might not be able to detect the fault correctly. More frequent icing encounters warrants re-evaluation of the air data system redundancy. One approach is to have systems that do not have similar failure modes to the pitot/static system. In this chapter, we describe sensor systems that have potentials to complement the pitot/static system because they can independently provide estimates of V, α, and/or β; and have dissimilar failure modes with the pitot/static system.

2.2 Ultrasonic Airspeed Sensors

Japan Aerospace Exploration Agency reported in [21] a design of ultrasonic air data sensor that can be used in aircraft. It is a modification of the ground-based anemometer and has been shown to work well in the 0 - 200 knots range. This sensor can sense all three axis components of the airspeed vector.

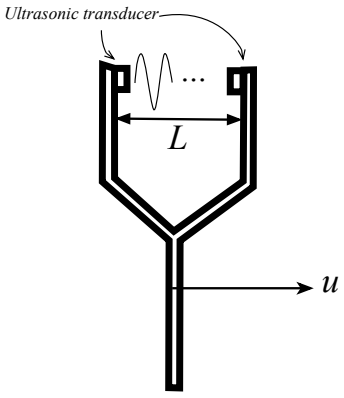

Figure 2.1: Single axis ultrasonic air data sensor

The working principle of this sensor is shown on Figure 2.1. The system consists of two ultrasonic transducers positioned at a distance L opposite to each other. Ultrasonic pulses are sent back and forth between the transducers at fixed time intervals.

When the aircraft is moving forward at velocity u, the time the pulse takes to travel from the fore to the aft transducer is given by:

$$T_1 = \frac{L}{a+u} \tag{2.1}$$

and to travel in the opposite direction, the pulse takes:

$$T_2 = \frac{L}{a-u} \tag{2.2}$$

where a is the speed of sound. The forward velocity u can be calculated using:

$$u = \frac{L}{2}\left(\frac{1}{T_1} - \frac{1}{T_2}\right) \tag{2.3}$$

The capability of this type of sensor to work at low airspeed makes it very suitable for rotorcraft and small aircraft. The sensor has error less than 0.5 m/s in each axis. The main challenge of using this sensor lies in positioning the sensor because downwash can significantly affect the accuracy of the measurements.

2.3 Laser-based Air Data Systems

Air data measurements can be made using laser. Based on their working principle, there are two kinds of laser-based air data systems. The first class of sensors determines airspeed, angle of attack, and sideslip angle from scattered reflection due to air particles around the airplane. This technique of estimating airspeed stems out of the remote sensing field where laser radar and light detection and ranging (LIDAR) system have become the state-of-the-art technique for meteorological measurements for detecting aerosol concentrations or profiling low altitude wind shear. The system works by detecting the Doppler shift in the returned signals reflected by particles in the airflow (aerosols, water, and ice particles). Thus, the signal-to-noise ratio is directly a function of particle concentration and size [22].

One of the earliest development of this system was done by Boeing Defense and Space Group who flight tested a 500mW (output power) diode-pumped solid-state

Nd:YAG laser aboard a NASA Dryden's DC-8. It is reported in [23] that the system's accuracy is better than 1.8 m/s (1-σ) at the aircraft's cruise speed of 265 knots (approx. 136.3 m/s). [22] showed success at an altitude slightly less than 40,000 ft. Flight testing on a helicopter, as reported in [24], was a success and the accuracy of the system is in the order of 1 to 2 m/s on each axis.

Recent developments of the former have been supported by the Europen Commission under the NESLIE (New Standby LIDAR Instrument) and DANIELA (Demonstration of Anemometry Instrument based on LASER) consortia. The goal of this effort is to develop a standby air data instrument. The participants include, among others, Thales Avionics, NLR, and Airbus.

This air data system uses four LiDARs that are focused on a very small volume approximately 35 cm from the aircraft fuselage (Figure 2.2). As such, only local measurements of V, α, and β can be determined. Looking further away in the free stream requires a more powerful laser system which is not practical for a standby instrument system. Based on the report in [2], the configuration shown on Figure 2.2 would not give accurate estimate of the free stream sideslip angle because most of the effect would be blocked by the fuselage. On the other hand, if the lasers are positioned on top of the fuselage, the situation is reversed. In this case, angle of attack estimate would be inaccurate. The flight tested system is shown to have accuracy better than 4 knots.

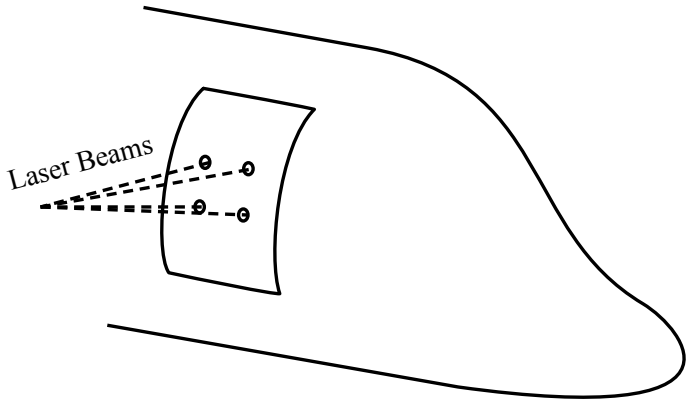

Figure 2.2: Laser-based air data system in [2]

The second category of laser-based air data system uses tunable diode laser absorption spectroscopy concept to measure the flow properties. Mach number and angle of attack are estimated based on the measured absorption spectrum of oxygen molecules on the flow [25]. Researchers at the University of New South Wales, Canberra, Australia developed this method initially for supersonic vehicles but it has been reported that they have successfully tested the same method at subsonic velocity [26].

2.4 Model-based Air Data Systems

Another approach which is the focus of this research is a model-based estimator that blends information from aircraft's EOM and other sensors to estimate V, α, and β. Unlike the physical redudancy scheme shown on Figure 1.5, this method of estimating the air data triplet is very promising for applications constrained by size, weight, power, and cost which include small (general aviation) aircraft and UAVs. For these applications, model-based air data systems could be an effective way to improve the systems' reliability. These model-based air data estimators, also known as synthetic air data systems, are software-based solutions and they work by fusing the information from the aircraft's equations of motion (EOM) with measurements from other motion sensors that already exist on the airplane (e.g. GPS, inertial sensors, compass, etc).

The idea of synthetic air data systems has been around since the 1980s. Airbus has patented a method and device to estimate airspeed from aircraft model [27, 28]. The device uses aircraft parameters such as mass and load factor to estimate the so-called aerodynamic airspeed. The estimate is claimed to be accurate enough that it can be used by other aircraft systems when the main pitot system fails. The air data system on Boeing 787 calculates a synthetic airspeed estimate "from angle of attack and inertial data" [29]. These measurements are used to form an accurate estimate of the lift coefficient from which the synthetic airspeed estimate is derived.

2.4.1 Prior Art

To understand the novelty of the estimator proposed in this work, it is worthwhile to review some existing methods and algorithms for generating synthetic estimates of V, α, and β. Due to the limited computational power at that time, the approach taken in [30] broke the problem into two and uses two separate estimators: One to estimate α in real-time (inflight estimator), and another for post-flight estimation of both α and β. The online estimator generates a snapshot estimate of α from a model of C_L for the aircraft. The load factor $n = \dfrac{L}{mg}$ computed from a vertical accelerometer with attitude and gravity compensation and rate gyro measurements are used to replace the complex model of the wing and horizontal stabilizer interaction in generating lift. The equation relating C_L to α is at the heart of this estimator and has the following mathematical form.

$$C_L = \frac{n \cdot mg \cdot x_t + \dot{q} I_y + pr(I_x - I_z) - C_{m_0} \frac{1}{2} \rho V^2 S \bar{c}}{\frac{1}{2} \rho V^2 S x_t \left[1 + \frac{x_{wb}}{x_t}\right]}$$
$$\hat{\alpha} = Fn\left(C_L, M, h\right) \tag{2.4}$$

where x_{wb} is the distance between the center of gravity of the aircraft and the wing-body aerodynamic center and x_t is the distance between the center of gravity of the aircraft and the aerodynamic center of the horizontal stabilizer. The function, $Fn(\cdot)$, that relates C_L to α can be empirical and determined by curve-fitting available aerodynamic data. With the navigation-grade INS installed on the F-15 and available C_L vs. α relationship, this inflight estimator was reported to generally satisfy the 0.5° accuracy requirement on α. Further, an accurate knowledge of C_{m_0} was found to be a critical factor to accurately estimate α. Simulations using this architecture produces α error histogram like the one shown in Figure 2.3.

Similar approach was taken by NASA Langley Research Center to develop an angle of attack command augmentation system for the AirSTAR flight test facility [31]. Although this approach showed success in estimating angle of attack in real time, this method also relies on the presence of a pitot-static system to take airspeed out of the equations. Moreover, the process is algebraic and does not take into account

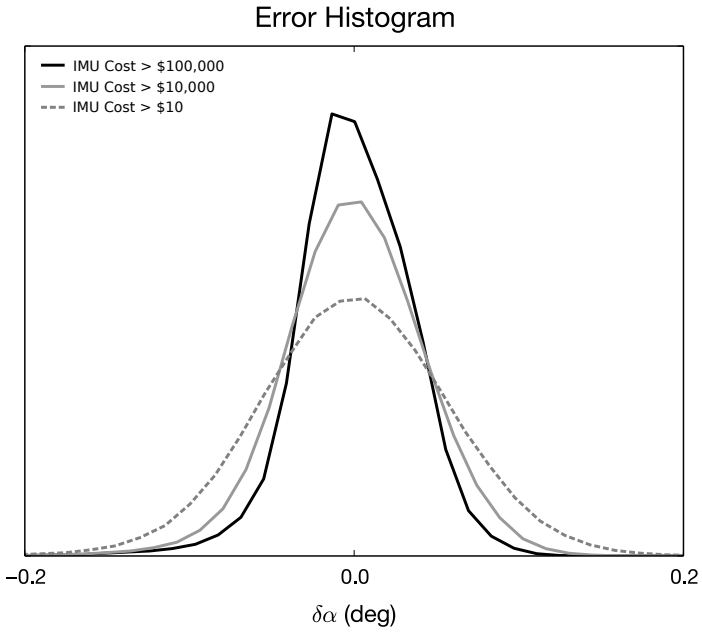

Figure 2.3: Simulated performance of Zeis Angle of Attack Estimator

the stochastic nature of the sensor measurement errors. Presumably, this is also the method used in Boeing 787.

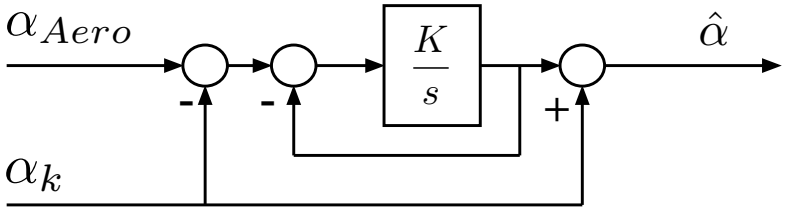

Figure 2.4: Complementary filter used in [3, 4]

Researchers at the Institute of Flight Mechanics and Flight Control at Technische Universität München synthesized an integrated air data and navigation system using low cost commercial-off-the-shelf (COTS) sensors: MEMS IMU, single frequency GPS receiver, and an airspeed sensor in the form of a pitot/static system [3, 4]. Angle of attack and sideslip angle are determined using inertial sensor outputs and an aerodynamic coefficient model.

An aerodynamic angle of attack (α_{Aero}) is calculated using an approach similar

to Equation (2.4). It is then combined with kinematic angle of attack, α_K, using a complementary filter like the one shown on Figure 2.4 to increase the system's bandwidth. A complementary filter essentially puts a low pass filter on the aerodynamic angle of attack and a high pass filter on the kinematic angle of attack, α_K, to enhance the filter performance across the frequency of interest. Mathematically, the output of the filter in the Laplace domain is given by

$$\hat{\alpha}(s) = \underbrace{\frac{K}{K+s}\alpha_{Aero}(s)}_{\text{Low Pass Filter}} + \underbrace{\frac{s}{s+K}\alpha_K(s)}_{\text{High Pass Filter}} \tag{2.5}$$

where

$$\alpha_K = \frac{\theta - \tan^{-1}\left(\frac{-V_D}{\sqrt{V_N^2+V_E^2}}\right)}{\cos\phi} \tag{2.6}$$

Because the complementary filter does not take into account the statistical error in the sensor measurements, there is no stochastic metric to quantify the filter output's uncertainty. Similar architecture is used to estimate the sideslip angle.

Unlike the method proposed in this dissertation, these works treated the triplet V, α, and β separately. They assume the availability of independent airspeed measurement and an accurate lift coefficient (C_L) model to estimate α and β using IMU measurements. As a a result, the accuracy of α and β estimates depends on the fidelity of the C_L model and the quality of the inertial sensor used. The requirement to have an airspeed measurement in this type of architecture is a major drawback because this means the (alternate) system is not completely independent. Additionally, owning to its architecture, estimating the error statistics in real time can be difficult.

Colgren in [32–34] presented a series of papers on using inertial sensors to estimate angle of attack and sideslip angle. In order to estimate these angles, gust compensation must be made. This calls for the aerodynamic model of the aircraft to subtract (algebraically) the dynamic acceleration from the total acceleration as measured by an accelerometer. As a consequence, an accurate dynamic model must be available. These works culminated in a US Patent in 2001 [35].

An important work is by Wise in which the air data estimation problem is cast into

a formal filtering framework [36, 37]. Wise's architecutre used an extended Kalman filter (EKF) to estimate α and β from pitch and roll angles derived from an inertial navigation system (INS); and IMU outputs (rotation rates and specific forces). The filter used an aircraft dynamic model for time update which takes dynamic pressure measurement from a pitot/static system to calculate the aerodynamic forces and moments. A functional block diagram that depicts this architecture and a simulated performance of this filter is shown on Figures 2.5(a) and 2.5(b), respectively. This work becomes a starting point for the estimator proposed here. In subsequent chapters, this estimator is extended to operate without a pitot/static system to supply the dynamic pressure.

2.4.2 Challenges with Model-based Systems

There are several drawbacks associated with model-based estimators such as those described in this section. First, the system is not "platform agnostic" meaning it is tied down to a specific dynamical system and may not be transferrable from one system to another. Additionally, obtaining an accurate model for estimation purpose is not trivial.

Because the dynamic model use EOM to predict the aircraft's responses to control input, it is necessary that the EOM's parameters such as mass, force, and moment coefficients are known very well. Moreover, the control input must be known almost perfectly. When this is not the case, then the statistics of the EOM prediction have to be evaluated. This is clearly not a straightforward process as it requires the engineer to develop a stochastic model of the system.

Finally, because there are some degrees of variation in the type of dynamic model that can be used in the estimator, model-based estimators can be realized in many different ways. Not all these realizations are fully observable. Chapters 3 and 4 report our studies on some of these issues and provide guideliness that can be used to design an accurate synthetic air data estimator.

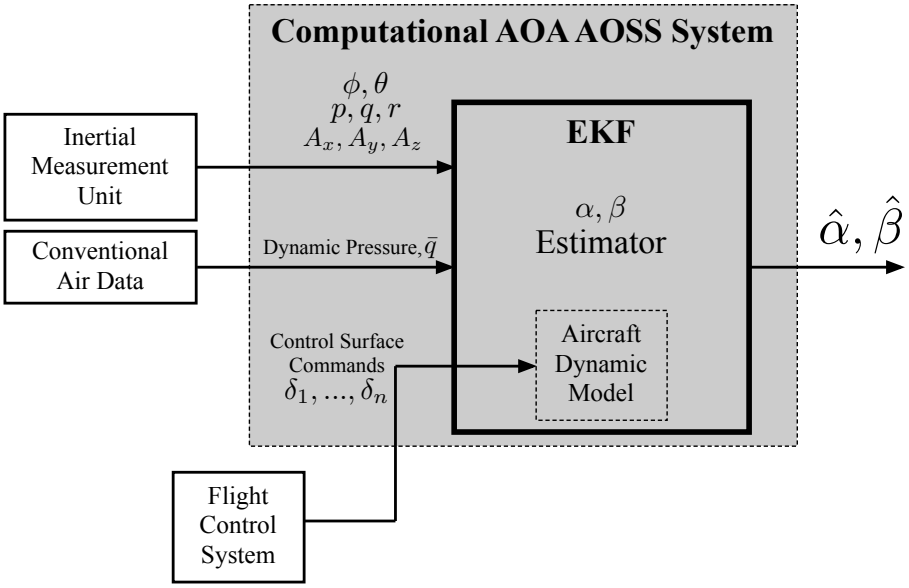

2.5(a)

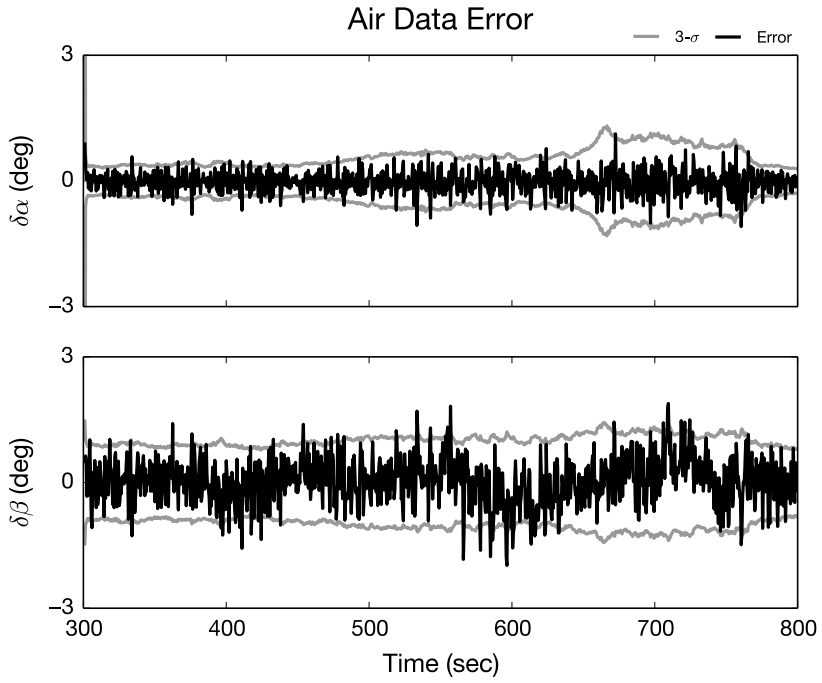

2.5(b)

Figure 2.5: Wise's Computational α/β system

2.5 Summary

An overview of alternative air data systems has been presented. The idea of using dynamic model to aid air data estimation is clearly not new. Prior work in this area, however, still relies on the availability of pitot/static system to operate. In the following chapters, we will present a model-based air data system that is completely independent from the pitot/static system.

Chapter 3

Synthetic Air Data Systems

Chapters 3 and 4 detail our model-based air data system. The *synthetic* air data system is different from prior work described in Section 2.4 in that it is completely independent from the conventional air data system. The system derives the air data quantities solely from the aircraft's EOM and motion sensors, hence the name. This chapter focuses on the modeling aspect of the estimator. Chapter 4 will focus on the sensor fusion architecture.

3.1 Basics of Synthetic Air Data Estimation

In theory, it is not difficult to generate a synthetic estimate (i.e., without using conventional pitot/static system) of the V, α, and β triplet by fusing the outputs from an inertial navigation system (INS) with information about wind speed. The INS generates an estimate of the absolute velocity (or groundspeed) of the airplane. A vector subtraction of the wind speed velocity from the absolute velocity will yield airspeed. In practice, however, this presents two challenges. First, it is difficult (if not, impossible) to obtain measurements of wind speed for each and every point in space in which an airplane will fly. Even if wind speed measurements at discrete points in space (a grid, for example) were available, models for extrapolating wind speed to arbitrary points in space may not be sufficiently accurate to allow generating usable estimates of the V, α, and β triplet [38–40]. Secondly, the synthetic estimate of V, α, and β rapidly becomes unusable as the inertial sensor quality degrades.

An alternate approach would be to include an aiding sensor, such as a GPS receiver, to aid the long term stability of the INS. To improve the quality of the estimates, this approach should also include wind velocity in the state vector. These additional states allow us to estimate wind continuously so the estimator does not depend on external wind information to work accurately. The synthetic air data system developed in this thesis uses IMU outputs (specific forces and rotation rates) and GPS outputs (position and velocity) along with a dynamic model of the aircraft to estimate V, α, and β. Outputs from these sensors are fused in an estimator.

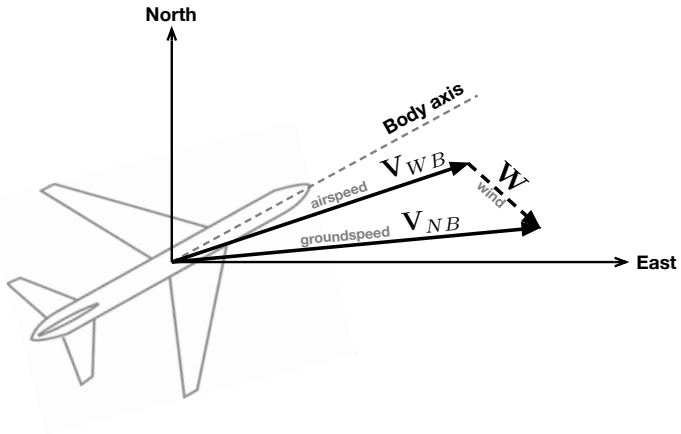

Figure 3.1: The wind triangle

Before going into the details of the estimator, we begin with reviewing the key equation that enable us to estimate V, α, and β from navigation sensors that output groundspeed measurements. Groundspeed (denoted $\mathbf{V}_{NB}^{N}$) is the resultant vector of adding the true airspeed vector and the wind vector (denoted $\widetilde{\mathbf{W}}^{N}$). This is illustrated in Figure 3.1 (2-Dimensional) and shown mathematically in Equation (3.1). The principle of synthetic air data estimation is this. Given the control inputs history, the EOM could predict the time evolution of $\mathbf{V}_{WB}^{B}$. The job of the estimator is to separate airspeed and wind from the groundspeed observation using Equation (3.1).

$$\mathbf{V}_{NB}^{N} = \mathbf{C}_{B}^{N}\mathbf{V}_{WB}^{B} + \widetilde{\mathbf{W}}^{N} \tag{3.1}$$

To achieve this, in the work reported here the estimator is formulated as an error

state Kalman filter which derives the errors in the air data information using the difference between the EOM's predictions and external measurements from the IMU and GPS [41]. In other words, the Kalman filter's state variables are, the difference between the true state and the estimated states, or:

$$\underbrace{\delta(\cdot)}_{\text{Error}} = \underbrace{(\cdot)}_{\text{True}} - \underbrace{(\hat{\cdot})}_{\text{Estimate}} \tag{3.2}$$

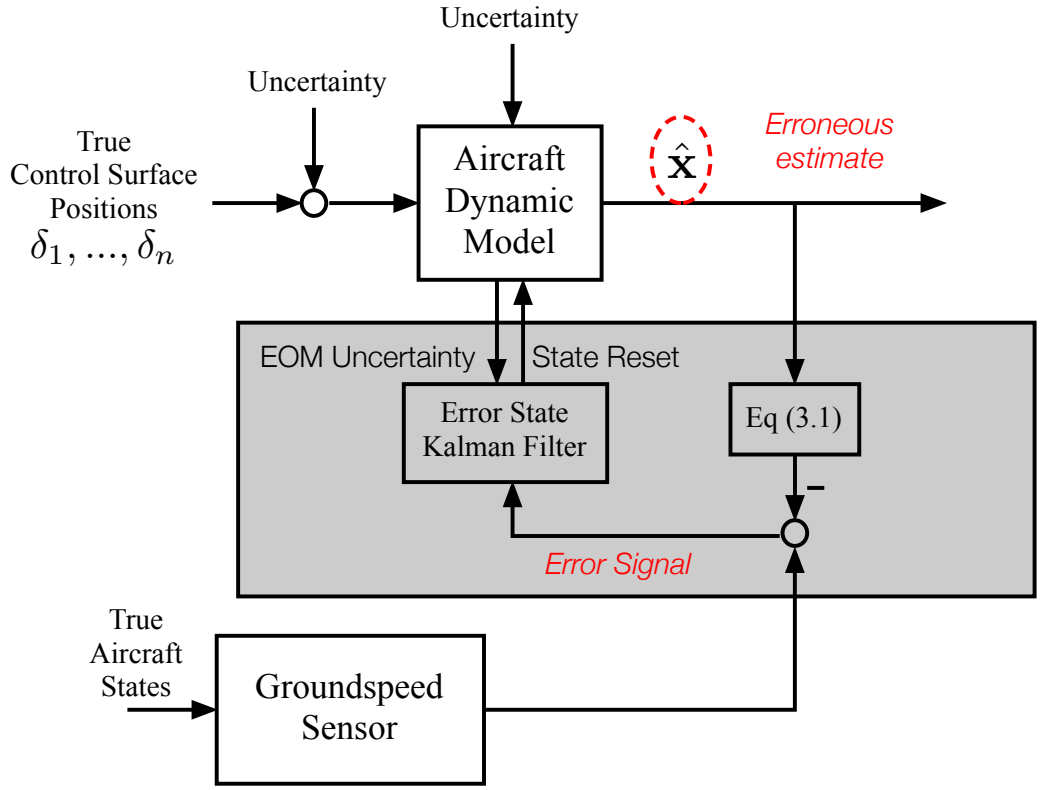

Figure 3.2: Synthetic air data system formulated as an error state Kalman filter

Figure 3.2 depicts the error state Kalman filter formulation for synthetic air data estimation. The "erroneous estimate" label on the output signal of the aircraft dynamic model indicates that it is not perfect. To illustrate this error state formulation, consider a situation where the true aircraft dynamics is described by the following

linear discrete state space model:

$$\mathbf{x}(k+1) = \mathbf{\Phi}\ \mathbf{x}(k) + \mathbf{G}\ \boldsymbol{\mathcal{U}}(k) \tag{3.3}$$

For the sake of simplicity, let's also assume that attitude and wind are known which, without loss of generality, could be set equal to zero. These assumptions allow us to exclude attitude and wind from the state vector so to end up with a linear filter. These assumptions will be relaxed later and the resulting nonlinearity will be handled accordingly. Thus, the state vector only consists of the air data vector components, that is:

$$\mathbf{x} = \mathbf{V}_{WB}^{B} \tag{3.4}$$

Finally, let's consider the situation where the discrepancy between the true and estimated output of the EOM is only caused by noisy control surface position measurements. That is, the EOM prediction (i.e., the erroneous estimates) is given by:

$$\begin{aligned} \hat{\mathbf{x}}(k+1) &= \mathbf{\Phi}\ \hat{\mathbf{x}}(k) + \mathbf{G}\ \boldsymbol{\mathcal{U}}_{\text{measured}}(k) \\ &= \mathbf{\Phi}\ \hat{\mathbf{x}}(k) + \mathbf{G}\ (\boldsymbol{\mathcal{U}}(k) - \mathbf{n}_k) \end{aligned} \tag{3.5}$$

where $\mathbf{n}_k$ denotes the noise in the control input measurement.

The Kalman filter is based upon the EOM error dynamics which is essentially a set of equations that describe the EOM prediction error. In other words, the filter's state vector is the difference between the true and estimated quantities (Equation (3.2)). Thus, we have the following error dynamics which in the Kalman filtering parlance becomes the filter's time update model:

$$\begin{aligned} \delta\mathbf{x}(k+1) &= \mathbf{x}(k+1) - \hat{\mathbf{x}}(k+1) \\ &= \mathbf{\Phi}\ (\mathbf{x}(k) - \hat{\mathbf{x}}(k)) + \mathbf{G}\ \mathbf{n}(k) \\ &= \mathbf{\Phi}\ \delta\mathbf{x}(k) + \mathbf{G}\ \mathbf{n}(k) \end{aligned} \tag{3.6}$$

The goal of the Kalman filter is to estimate $\delta\mathbf{x}$ and use it to correct the EOM prediction, $\hat{\mathbf{x}}$.

The groundspeed measurement model is given by:

$$\mathbf{z}_{\text{sensor}}(k) = \mathbf{H}\mathbf{x}(k) + \mathbf{v}(k) \tag{3.7}$$

where $\mathbf{H}$, in this case, is the direction cosine matrix $\mathbf{C}_B^N$ (known) and $\mathbf{v}$ is the measurement noise. Defining $\delta\mathbf{z}$ as the difference between the sensor measurement and the groundspeed prediction from the aircraft dynamic model, we have:

$$\begin{aligned} \delta\mathbf{z}(k) &= \mathbf{z}_{\text{sensor}}(k) - \mathbf{C}_B^N\hat{\mathbf{x}}(k) \\ &= \mathbf{H}\ \delta\mathbf{x}(k) + \mathbf{v}(k) \end{aligned} \tag{3.8}$$

$\delta\mathbf{z}$ becomes the measurements fed into the filter. The next two sections derive the aircraft dynamic model and its corresponding error model (i.e., Equation (3.6)) in details.

3.2 Aircraft Dynamic Model

There are two types of aircraft EOM that can be used for the synthetic air data estimator. The first type is the six degrees-of-freedom rigid body aircraft dynamic model. This is often regarded as a good model for non-flexible aircraft where aero-structure interaction can be neglected. Although the equations are nonlinear and coupled, they are valid for a broad range of flight condition and so results in the most accurate synthetic air data estimator. The process of obtaining the aerodynamic forces and moments model, however, can be a long and expensive endeavor. The second type of aircraft model is the linear aircraft dynamic model which approximates the first model around a certain trim condition. It is simpler than the nonlinear model, but it is not as accurate because it is valid only in the region around equilibrium or trim condition. In the description below, methods that would improve the air data estimator that uses the linear model are discussed.

3.2.1 Nonlinear Aircraft Dynamics

Under the flat earth assumption, the 6 degrees-of-freedom rigid body model for a propeller driven fixed wing aircraft is summarized by Equations (3.9) and (3.10) [42]. Here, the aircraft is assumed to be symmetric about the $x_B z_B$-plane, so I_{xy} and I_{yz} are both zero.

$$\begin{aligned} T + X - mg\sin\theta &= m\left(\dot{u} + qw - rv\right) \\ Y + mg\cos\theta\sin\phi &= m\left(\dot{v} + ru - pw\right) \\ Z + mg\cos\theta\cos\phi &= m\left(\dot{w} + pv - qu\right) \end{aligned} \tag{3.9}$$

$$\begin{aligned} \mathcal{T} + \mathcal{L} &= I_x\dot{p} - I_{xz}\left(\dot{r} + pq\right) - \left(I_y - I_z\right)qr \\ r_z T + \mathcal{M} &= I_y\dot{q} - I_{xz}\left(r^2 - p^2\right) - \left(I_z - I_x\right)rp \\ -r_y T + \mathcal{N} &= I_z\dot{r} - I_{xz}\left(\dot{p} - qr\right) - \left(I_x - I_y\right)pq \end{aligned} \tag{3.10}$$

The aerodynamic forces and moments along the aircraft's body axes are denoted $\mathbf{F}^B_{\text{Aero}} = [\ X \quad Y \quad Z\ ]^T$ and $\mathbf{M}^B_{\text{Aero}} = [\ \mathcal{L} \quad \mathcal{M} \quad \mathcal{N}\ ]^T$, respectively, while T and $\mathcal{T}$ denote the propeller's thrust and torque acting on the aircraft.

The thrust line is assumed to be aligned with x_B-axis and acts on a point $\mathbf{r}^B_{\text{Propulsion}} = [\ r_x \quad r_y \quad r_z\ ]^T$ relative to the CG (see Figure 3.3). The offsets r_y and r_z are non-zero because the descending propeller blades produce more thrust than the ascending ones resulting in the left turning tendency on propeller aircraft known as the P-factor [14, Ch. 4]. If any of these assumption are not valid (e.g., the thrust is not aligned with x_B), then Equations (3.9) and (3.10) should be modified accordingly. Both T and $\mathcal{T}$ are functions of the air density (ρ), the blade diameter (d), and its rotational speed (f in rotations per second or Hertz). They can be written in terms of the thrust (C_T) and torque coefficients (C_P) as follows:

$$\begin{aligned} T &= \rho f^2 d^4 C_T \\ \mathcal{T} &= -\frac{\rho f^2 d^5 C_P}{2\pi} \end{aligned} \tag{3.11}$$

These coefficients, C_T and C_P, are typically functions of the advance ratio J, defined

as:

$$J = \frac{V}{fd} \tag{3.12}$$

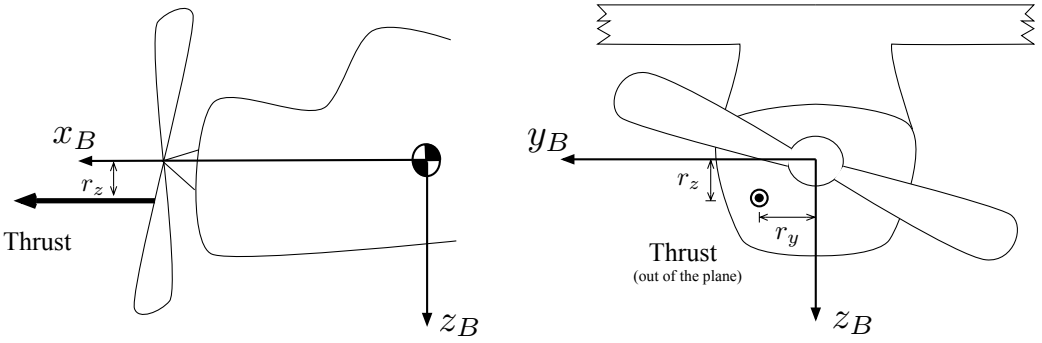

Figure 3.3: Thrust line

The aerodynamic forces and moments are in general functions of air density, airspeed, angle of attack, sideslip, body rates, and control surface deflections; and their dependence on some of these variables is non-linear. Assuming small angle of attack and sideslip angle, the aerodynamic forces are given in terms of the drag (C_D), side force (C_Y), and lift coefficients (C_L) by:

$$\begin{aligned} X &= -\frac{1}{2}\rho V^2 S C_D \\ Y &= \frac{1}{2}\rho V^2 S C_Y \\ Z &= -\frac{1}{2}\rho V^2 S C_L \end{aligned} \tag{3.13}$$

And similarly, the aerodynamic moments are given by:

$$\begin{aligned} \mathcal{L} &= \frac{1}{2}\rho V^2 S b\ C_l \\ \mathcal{M} &= \frac{1}{2}\rho V^2 S \bar{c}\ C_m \\ \mathcal{N} &= \frac{1}{2}\rho V^2 S b\ C_n \end{aligned} \tag{3.14}$$

where C_l, C_m, and C_n are the rolling, pitching, and yawing moment coefficients, respectively. b is the wing span and $\bar{c}$ is the mean aerodynamic chord length. These

coefficients are typically linear functions of α, β, and the control surface deflections. Their functional relationships can be obtained from wind tunnel or flight testings.

Finally, the aircraft's attitude, $\mathbf{\Psi}$, is propagated using the attitude kinematics which is nonlinear in $\mathbf{\Psi}$ and the body rates, $\boldsymbol{\omega}^B = [\ p \quad q \quad r\ ]^T$. Equation (3.9) parameterizes the attitude using Euler angles:

$$\mathbf{\Psi} = \begin{bmatrix} \phi \\ \theta \\ \psi \end{bmatrix} \tag{3.15}$$

And, the rate of change of these angles are given by:

$$\begin{bmatrix} \dot{\phi} \\ \dot{\theta} \\ \dot{\psi} \end{bmatrix} = \begin{bmatrix} 1 & \sin\phi\tan\theta & \cos\phi\tan\theta \\ 0 & \cos\phi & -\sin\phi \\ 0 & \sin\phi\sec\theta & \cos\phi\sec\theta \end{bmatrix} \begin{bmatrix} p \\ q \\ r \end{bmatrix} \tag{3.16}$$

Other attitude parameterization like the quaternions have their corresponding propagation equations that can be found in textbooks such as [43].

As seen on Figure 3.2, the exogeneous inputs to the EOM which determine the history of the aircraft's states are the elevator (δ_e), aileron (δ_a), and rudder deflections (δ_r) as well as the propeller's rotational speed (RPM). When the values of these input variables are not known accurately, the outputs of the EOM would become more uncertain as the integration time gets longer. One source of this input uncertainty is noise present in the measured values of these inputs (Figure 3.2). Additionally, aircraft experience gust and turbulence during flights. Because they cannot be modeled with sufficient accuracy, they are often neglected. This also contributes to error in the state prediction. Finally, the contribution of model imperfection cannot be discounted. Unmodeled dynamics and error in model parameters, however small, would eventually cause the EOM prediction to diverge from the true value. These are errors that should be taken into account when determining the dynamic model output uncertainty.

Of these, model imperfection is one of the most complicated error sources to

account for accurately. Even though its contribution is not negligible, quantifying the contribution of each parameter in the EOM and deriving an analytical model for its propagation are very challenging for such nonlinear problems. One way to make this problem more tractable is by using input uncertainty to account for the contribution of model imperfection. The following simple example tries to illustrate this point.

Consider a static pitching moment coefficient model as follows:

$$\underbrace{C_m + \delta C_m}_{\text{Calculated } C_m} = [C_{m_0} + \delta C_{m_0}] + [C_{m_\alpha} + \delta C_{m_\alpha}](\alpha + \delta\alpha) + \left[C_{m_{\delta_e}} + \delta C_{m_{\delta_e}}\right](\delta_e + n_{\delta_e}) \tag{3.17}$$

where $\delta(\cdot)$ denotes deviation from the true value and n_{δ_e} denotes the elevator position measurement error. The sum of the true value of the pitching moment coefficient, C_m, and its error, δC_m, on the right hand side is the calculated value of C_m. Contributing to δC_m are n_{δ_e}; errors in the coefficients C_{m_0}, C_{m_α}, and $C_{m_{\delta_e}}$; and errors in the state variables. Retaining only the linear terms:

$$\delta C_m \approx \delta C_{m_0} + \delta C_{m_\alpha}\alpha + \delta C_{m_{\delta_e}}\delta_e + C_{m_\alpha}\delta\alpha + C_{m_{\delta_e}}n_{\delta_e} \tag{3.18}$$

Accounting for errors in the aerodynamic coefficients $C_{m_{(\cdot)}}$ are not easy because of two reasons. First, their uncertainty is seldom available. Secondly, considering these coefficients as stochastic makes the problem highly nonlinear. To simplify this situation, this work assumes that all of their contributions can be overbounded using n'_{δ_e}. Mathematically, it is written as:

$$\delta C_m \preceq C_{m_\alpha}\delta\alpha + C_{m_{\delta_e}}n'_{\delta_e} \tag{3.19}$$

where $\preceq$ indicates the overbounding relationship between the left hand side and the right hand side. The statistics of n'_{δ_e} is chosen to enforce the relationship in Equation (3.19) and hence, n'_{δ_e} is not the same as n_{δ_e}. This ensures the resulting statistics of pitching moment coefficient error is conservative relative to the actual statistics.

Statistical overbounding is the subject of research such as in [44–48]. It is a very

important concept for navigation systems because they must be accurate and have integrity or bounded accuracy. Loss of integrity is undesirable because when this happens, the system fails to detect inaccurate or erroneous solutions. This occurs when the filter is overly confident with its solution. Overbounding minimizes the probability that such hazardously misleading events occur. One of the method that can be used for the air data estimation problem follows the techniques for the INS described in [48]. This is achieved by choosing the statistics of n'_{δ_e} so that the integrated tail probability (i.e., the cumulative distribution function or CDF) of δC_m exceeds the integrated tail probability of the actual error distribution of C_m.

Equations (3.9), (3.10), and (3.16) can be written compactly in discrete form as:

$$\mathbf{x}_{\text{ac}}(k+1) = \boldsymbol{\mathcal{F}}(\mathbf{x}_{\text{ac}}(k), \boldsymbol{\mathcal{U}}_{\text{measured}}(k)) \tag{3.20}$$

where $\mathbf{x}_{\text{AC}}$ and $\boldsymbol{\mathcal{U}}$ are the aircraft's state vector and the flight control vector, respectively. $\mathbf{x}_{\text{AC}}$ contains the following variables:

$$\mathbf{x}_{\text{ac}} = \begin{bmatrix} \mathbf{V}_{WB}^{B} \\ \boldsymbol{\omega}^{B} \\ \boldsymbol{\Psi} \end{bmatrix} \tag{3.21}$$

and $\boldsymbol{\mathcal{U}}$ is defined as:

$$\boldsymbol{\mathcal{U}} = \begin{bmatrix} \delta_e \\ \delta_a \\ \delta_r \\ f \end{bmatrix} \tag{3.22}$$

$$\boldsymbol{\mathcal{U}}_{\text{measured}}(k) = \boldsymbol{\mathcal{U}}(k) - \mathbf{n}(k) \tag{3.23}$$

Equation (3.20) is stochastic because it uses measured value of the control inputs. In this work, the measured value is assumed to be corrupted by noise only (Equation (3.23)). In reality, it can be biased or have scale factor errors. The noise vector $\mathbf{n}$ is

a Gaussian random vector with the following properties:

$$\begin{aligned} \mathbb{E}(\mathbf{n}(k)) &= 0, \qquad \forall k \\ \mathbb{E}(\mathbf{n}(k)\mathbf{n}^T(k)) = \mathbf{Q}_{\text{ac}} &= \begin{bmatrix} \sigma_e^2 & 0 & 0 & 0 \\ 0 & \sigma_a^2 & 0 & 0 \\ 0 & 0 & \sigma_r^2 & 0 \\ 0 & 0 & 0 & \sigma_f^2 \end{bmatrix} \\ \mathbb{E}(\mathbf{n}(k)\mathbf{n}^T(l)) &= 0, \qquad \forall k \neq l \end{aligned} \tag{3.24}$$

The error state dynamics is derived as follows. A Taylor's series expansion of Equation (3.20) about the best known values (or estimates) of $\mathbf{x}_{\text{ac}}(k)$ and $\boldsymbol{\mathcal{U}}(k)$ is given by Equation (3.25).

$$\begin{aligned} \hat{\mathbf{x}}_{\text{ac}}(k+1) + \delta\mathbf{x}_{\text{ac}}(k+1) = \; & \boldsymbol{\mathcal{F}}(\hat{\mathbf{x}}_{\text{ac}}(k), \; \boldsymbol{\mathcal{U}}_{\text{measured}}(k)) + \\ & \left.\frac{\partial \boldsymbol{\mathcal{F}}}{\partial \mathbf{x}_{\text{ac}}}\right|_{\hat{\mathbf{x}}_{\text{ac}}(k)} (\mathbf{x}_{\text{ac}}(k) - \hat{\mathbf{x}}_{\text{ac}}(k)) + \\ & \left.\frac{\partial \boldsymbol{\mathcal{F}}}{\partial \boldsymbol{\mathcal{U}}}\right|_{\hat{\mathbf{x}}_{\text{ac}}(k)} (\boldsymbol{\mathcal{U}}(k) - \boldsymbol{\mathcal{U}}_{\text{measured}}(k)) + \ldots \end{aligned} \tag{3.25}$$

$\hat{\mathbf{x}}_{\text{ac}}(k)$ is the best estimate of the aircraft's state vector at time step k and $\boldsymbol{\mathcal{U}}_{\text{measured}}(k)$ is the best known value of the flight control vector at time k. The sum of the terms on the left hand side of Equation (3.25) is the true value of the aircraft state vector (cf. Equation (3.2)). By choosing $\hat{\mathbf{x}}_{\text{ac}}(k+1) = \boldsymbol{\mathcal{F}}(\hat{\mathbf{x}}_{\text{ac}}(k), \; \boldsymbol{\mathcal{U}}_{\text{measured}}(k))$ and ignoring higher order terms, we obtain:

$$\begin{aligned} \delta\mathbf{x}_{\text{ac}}(k+1) &= \left.\frac{\partial \boldsymbol{\mathcal{F}}}{\partial \mathbf{x}_{\text{ac}}}\right|_{\hat{\mathbf{x}}_{\text{AC}}(k)} \delta\mathbf{x}_{\text{ac}}(k) + \left.\frac{\partial \boldsymbol{\mathcal{F}}}{\partial \boldsymbol{\mathcal{U}}}\right|_{\hat{\mathbf{x}}_{\text{AC}}(k)} \mathbf{n}(k) \\ &= \boldsymbol{\Phi}_{\text{ac}}(k) \; \delta\mathbf{x}_{\text{ac}}(k) + \mathbf{G}_{\text{ac}}(k) \; \mathbf{n}(k) \end{aligned} \tag{3.26}$$

where $\boldsymbol{\Phi}_{\text{ac}}$ and $\mathbf{G}_{\text{ac}}$ are the Jacobian and noise shaping matrices, respectively, and their entries are defined on Appendix B.

Equation (3.26) is a linear approximation of the state error propagation dynamics. It becomes the basis of the extended Kalman filter (EKF) architecture as described

in estimation textbooks such as [49, 50]. The EKF's time update process is done in the following manner. First, after being initialized appropriately, the aircraft state variables defined in Equation (3.21) are propagated according to:

$$\hat{\mathbf{x}}_{\text{ac}}(k+1) = \boldsymbol{\mathcal{F}}(\hat{\mathbf{x}}_{\text{ac}}(k),\ \ \boldsymbol{\mathcal{U}}_{\text{measured}}(k)) \tag{3.27}$$

The error state's estimate $\delta\hat{\mathbf{x}}_{\text{ac}}$ is propagated using:

$$\begin{aligned}\delta\hat{\mathbf{x}}_{\text{ac}}(k+1) &= \mathbb{E}(\delta\mathbf{x}_{\text{ac}}(k+1)) \\ &= \mathbb{E}(\boldsymbol{\Phi}_{\text{ac}}(k)\ \delta\mathbf{x}_{\text{ac}}(k) + \mathbf{G}_{\text{ac}}(k)\ \mathbf{n}(k)) \\ &= \boldsymbol{\Phi}_{\text{ac}}(k)\ \delta\hat{\mathbf{x}}_{\text{ac}}(k)\end{aligned} \tag{3.28}$$

It is assumed that although the initialization might contain random error, but on average it is unbiased. In other words, $\delta\hat{\mathbf{x}}_{\text{ac}}(0) = \mathbb{E}(\delta\mathbf{x}_{\text{ac}}(0)) = 0$. As such, using the time update process only, $\delta\hat{\mathbf{x}}_{\text{ac}}(k) = 0$, $\forall k$. It does not mean that $\hat{\mathbf{x}}_{\text{ac}}(0)$ is perfect or does not have any error, but the average error over multiple realizations is zero. The filter's objective is to estimate $\delta\hat{\mathbf{x}}_{\text{ac}}$ given the observations $\{\delta\mathbf{z}(0)\ \ldots\ \mathbf{z}(k)\}$ (cf. Equation (3.8)).

The uncertainty or the covariance of the error state, denoted $\mathbf{P}_{\text{ac}} = \mathbb{E}(\delta\mathbf{x}_{\text{ac}} \cdot \delta\mathbf{x}_{\text{ac}}^T)$, can be propagated using the Lyapunov equation:

$$\mathbf{P}_{\text{ac}}(k+1) = \boldsymbol{\Phi}_{\text{ac}}(k)\mathbf{P}_{\text{ac}}(k)\boldsymbol{\Phi}_{\text{ac}}^T(k) + \mathbf{G}_{\text{ac}}(k)\mathbf{Q}_{\text{ac}}\mathbf{G}_{\text{ac}}^T(k) \tag{3.29}$$

The values of σ_f, σ_e, σ_a, and σ_r in Equation (3.24) are design parameters chosen so that the covariance estimates of $\delta\mathbf{x}_{\text{ac}}$ overbound the actual output uncertainty. In the context of a synthetic air data estimator, this can be achieved by tuning the entries of the covariance matrix $\mathbf{Q}_{\text{ac}}$ so that the estimation errors of V, α, and β (i.e., after the measurement update) are small and bounded by its estimated covariance.

As the model parameters become more uncertain, the σ's have to be inflated to account for it. Consequently, the usefulness of the dynamic model as a virtual sensor is limited by the accuracy of the model parameters. Unfortunately, the process to obtain these parameters can be a time consuming and expensive endeavor, especially

because it has to be done at regular intervals to ensure the validity of the model.

3.2.2 Linear Aircraft Dynamics

The linear aircraft dynamic model is an approximation of the nonlinear model around a certain trim condition. Because the linear model is a local approximation of the aircraft dynamics, its model parameters can be identified more quickly than in the nonlinear setting. This makes the linear model very practical. When linearized about straight and level flight, the dynamics decouple into two modes: The longitudinal and the lateral/directional modes. The state vector of each mode is a subset of the aircraft's total state vector.

There are two sets of differential equations for the linear model where each corresponds to the dynamic modes. The longitudinal mode is governed by the following differential equation:

$$\Delta\dot{\mathbf{x}}_{\text{lon}} = \mathbf{A}_{\text{lon}}\Delta\mathbf{x}_{\text{lon}} + \mathbf{B}_{\text{lon}}\Delta\boldsymbol{\mathcal{U}}_{\text{lon}} + \Delta\mathbf{F}_{\text{prop}} \tag{3.30}$$

where the state vector, $\Delta\mathbf{x}_{\text{lon}}$, is given by:

$$\Delta\mathbf{x}_{\text{lon}} = [\ \Delta u \quad \Delta w \quad \Delta q \quad \Delta\theta\ ]^T \tag{3.31}$$

and the control vector, $\Delta\boldsymbol{\mathcal{U}}_{\text{lon}}$, and thrust contribution $\Delta\mathbf{F}_{\text{prop}}$ are given by

$$\Delta\boldsymbol{\mathcal{U}}_{\text{lon}} = \Delta\delta_e, \qquad \Delta\mathbf{F}_{\text{prop}} = \left[\ \frac{\Delta T}{m} \quad 0 \quad 0 \quad 0\ \right]^T \tag{3.32}$$

The lateral/directional dynamics is governed by:

$$\Delta\dot{\mathbf{x}}_{\text{lat}} = \mathbf{A}_{\text{lat}}\Delta\mathbf{x}_{\text{lat}} + \mathbf{B}_{\text{lat}}\Delta\boldsymbol{\mathcal{U}}_{\text{lat}} + \Delta\mathbf{M}_{\text{prop}} \tag{3.33}$$

where the state and control vectors are given by

$$\begin{gathered}\Delta\mathbf{x}_{\text{lat}} = [\ \Delta v \quad \Delta p \quad \Delta r \quad \Delta\phi\ ]^T \\ \Delta\boldsymbol{\mathcal{U}}_{\text{lat}} = [\ \Delta\delta_a \quad \Delta\delta_r\ ]^T, \quad \Delta\mathbf{M}_{\text{prop}} = \begin{bmatrix} \dfrac{\Delta\mathcal{T}}{I_x} & 0 & 0 & 0 \end{bmatrix}^T\end{gathered} \tag{3.34}$$

Unlike the nonlinear model, the variables in Equations (3.30) and (3.33) are perturbations from the trim condition, that is

$$\Delta\mathbf{x}_{\text{ac}} = \mathbf{x}_{\text{ac}} - \bar{\mathbf{x}}_{\text{ac}} \tag{3.35}$$

where $\bar{\mathbf{x}}_{\text{ac}}$ is the value of $\mathbf{x}_{\text{ac}}$ at the trim condition. It means the state variables must be adjusted for trim before and after they are used in Equations (3.30) and (3.33). To integrate the state vector from time step k to $k+1$, the trim condition is first subtracted off of the state vector:

$$\Delta\mathbf{x}_{\text{ac}}(k) = \mathbf{x}_{\text{ac}}(k) - \bar{\mathbf{x}}_{\text{ac}} \tag{3.36}$$

Next, the derivatives $\dot{\mathbf{x}}_{\text{ac}}(k)$ is obtained using Equations (3.30) and (3.33). After numerically integrating $\dot{\mathbf{x}}_{\text{ac}}(k)$, the state vector at time $k+1$ is given by:

$$\mathbf{x}_{\text{ac}}(k+1) = \Delta\mathbf{x}_{\text{ac}}(k+1) + \bar{\mathbf{x}}_{\text{ac}} \tag{3.37}$$

Similar to the treatment in the nonlinear model, $\Delta\boldsymbol{\mathcal{U}}_{\text{lon}}$ and $\Delta\boldsymbol{\mathcal{U}}_{\text{lat}}$ used to propagate these differential equations are noisy. The noise statistics (i.e., $\mathbf{Q}_{\text{ac}}$) is chosen to overbound the EOM prediction uncertainty.

The advantage of using the state space formulation shown in Equations (3.30) and (3.33) is that the $\mathbf{A}$ and $\mathbf{B}$ matrices could be identified or estimated from aircraft's response alone. In other words, the entries of these matrices could be estimated only by applying appropriate control inputs and observing the aircraft's behavior (using sensors) resulting in a very quickly identifiable model. In contrast, the parameters for the nonlinear model is estimated in two steps. The aircraft's mass and inertia properties has to be known *a priori* to the aerodynamic coefficient identification.

Because mass and inertia properties change from flight to flight, the linear model has an advantage that it can be updated very quickly. This is especially true for aircraft with varying payload like manned aircraft. Airbus's synthetic air data system, for example, will recalibrate its internal aircraft parameters when a traditional air data system (i.e. a pitot/static system) is available (not faulty) [28]. For these reasons, it is judged that the linear model would be more practical than the nonlinear model for synthetic air data application.

System identification techniques are subject of discussions in the literature such as [51–55]. So, only the summary of the technique used in this work is presented here. Here, the output error method such as described in [52] is used to identify the model parameters of the aircraft used in the experimental validation. Although this method works well for the work reported in this thesis, it is not generally true for all type of aircraft. For example, it does not work when the aircraft is unstable. It has to be modified for the algorithm to converge.

The output error system identification algorithm essentially estimates the vector of parameters $\boldsymbol{\xi}$ by minimizing the cost function $J(\boldsymbol{\xi})$ defined as:

$$J(\boldsymbol{\xi}) = \frac{1}{2} \sum_{k=0}^{N-1} \left[\mathbf{z}(k) - \tilde{\mathbf{z}}_{\boldsymbol{\xi}}(k)\right]^T \mathbf{R}^{-1} \left[\mathbf{z}(k) - \tilde{\mathbf{z}}_{\boldsymbol{\xi}}(k)\right] \tag{3.38}$$

where $\mathbf{z}(k)$, $k = 0, 1, \ldots, N-1$ are N measurement samples made using onboard sensors; $\tilde{\mathbf{z}}_{\boldsymbol{\xi}}(k)$, $k = 0, 1, \ldots, N-1$ is the output predicted by the EOM; and $\mathbf{R}$ is the covariance matrix of $[\mathbf{z}(k) - \tilde{\mathbf{z}}_{\boldsymbol{\xi}}(k)]$. The elements of the covariance matrix $\mathbf{R}$ also have to be estimated because $\tilde{\mathbf{z}}_{\boldsymbol{\xi}}$ will not be completely error free (although it is assumed to be the case to avoid numerical problem). The cost function is a function of the unknown parameter vector $\boldsymbol{\xi}$ because $\tilde{\mathbf{z}}_{\boldsymbol{\xi}}$ depends on $\boldsymbol{\xi}$. As such, $J(\boldsymbol{\xi})$ is more complicated than quadratic in the unknown parameters and so, the minimization has to be done iteratively. At each iteration step, the cost function is minimized using a slightly modified Newton-Raphson algorithm [52] described in the following algorithm.

- **Initialization**

Initialize $\boldsymbol{\xi}$ using linear regression method described in [51, Chapter 5]. Also, initialize the matrix $\mathbf{R}$ as a diagonal value to a reasonable measurement noise covariance value.

- **Optimization**
  - Step 1: (Iteration step L) Calculate $\tilde{\mathbf{z}}_{\boldsymbol{\xi}}(k)$ for $k = 0,\ 1,\ \ldots,\ N-1$ using the current value of the parameter vector $\boldsymbol{\xi}_L$.
  - Step 2: Calculate $J(\boldsymbol{\xi}_L)$, $\nabla_{\boldsymbol{\xi}} J(\boldsymbol{\xi}_L)$, and $\nabla^2_{\boldsymbol{\xi}} J(\boldsymbol{\xi}_L)$. The Jacobian and the Hessian are calculated as follows:

$$\nabla_{\boldsymbol{\xi}} J(\boldsymbol{\xi}) = -\sum_{k=0}^{N-1} \left[\mathbf{z}(k) - \tilde{\mathbf{z}}_{\boldsymbol{\xi}}(k)\right]^T \mathbf{R}^{-1} \left[\nabla_{\boldsymbol{\xi}} \tilde{\mathbf{z}}_{\boldsymbol{\xi}}(k)\right] \tag{3.39}$$

$$\begin{aligned} \nabla^2_{\boldsymbol{\xi}} J(\boldsymbol{\xi}) &= \sum_{k=0}^{N-1} \left[\nabla_{\boldsymbol{\xi}} \tilde{\mathbf{z}}_{\boldsymbol{\xi}}(k)\right]^T \mathbf{R}^{-1} \left[\nabla_{\boldsymbol{\xi}} \tilde{\mathbf{z}}_{\boldsymbol{\xi}}(k)\right] - \sum_{k=0}^{N-1} \left[\mathbf{z}(k) - \tilde{\mathbf{z}}_{\boldsymbol{\xi}}(k)\right]^T \mathbf{R}^{-1} \left[\nabla^2_{\boldsymbol{\xi}} \tilde{\mathbf{z}}_{\boldsymbol{\xi}}(k)\right] \\ &\approx \sum_{k=0}^{N-1} \left[\nabla_{\boldsymbol{\xi}} \tilde{\mathbf{z}}_{\boldsymbol{\xi}}(k)\right]^T \mathbf{R}^{-1} \left[\nabla_{\boldsymbol{\xi}} \tilde{\mathbf{z}}_{\boldsymbol{\xi}}(k)\right] \end{aligned} \tag{3.40}$$

    The Gauss-Newton approximation shown on the second line of Equation (3.40) is computationally simpler because the second gradient of the EOM output needs not be computed. It has also been shown to speed up convergence without sacrificing performance [52].
  - Step 3: Update the vector $\boldsymbol{\xi}$ using:

$$\boldsymbol{\xi}_{L+1} = \boldsymbol{\xi}_L - \left[\nabla^2_{\boldsymbol{\xi}} J(\boldsymbol{\xi}_L)\right]^{-1} \left[\nabla_{\boldsymbol{\xi}} J(\boldsymbol{\xi}_L)\right]^T \tag{3.41}$$

  - Repeat Step 1 until convergence is reached.
- **Recalculate Covariance Matrix**

The matrix $\mathbf{R}$ is recalculated using:

$$\mathbf{R} = \frac{1}{N}\sum_{k=0}^{N-1}\left[\mathbf{z}(k) - \tilde{\mathbf{z}}_{\boldsymbol{\xi}}(k)\right]\left[\mathbf{z}(k) - \tilde{\mathbf{z}}_{\boldsymbol{\xi}}(k)\right]^T \tag{3.42}$$

- Repeat Optimization step until convergence is reached.

Once the unknown elements of the $\mathbf{A}$ and $\mathbf{B}$ matrices are identified, we have a linear model for the synthetic air data system. However, since the linear model is a local approximation of the actual dynamics around the trim condition, it is only valid when the aircraft is flying close to the trim condition. As it gets farther away from trim, the model becomes less accurate which can make it ineffective to estimate the air data triplets. There are three improvements that could enhance the accuracy of the synthetic air data estimator during maneuvers in which the aircraft is far away from the trim condition.

1. **Attitude Kinematics**
   In the linear model, the attitude kinematics are greatly simplified. The longitudinal model approximates $\dot{\theta}$ as q and the lateral/directional model approximates $\dot{\phi}$ as p. This, however, is only true when ϕ and θ are small which is rarely the case in practice because the aircraft will have a significant roll angle during a turn. The error from using the small angle approximation can be quite large so the model needs to be modified to handle this situation. This can easily be improved by using the nonlinear attitude kinematics equations such as Equation (3.16) to obtain the attitude. Unlike the linearized equations, these are valid for -90° $< \theta <$ 90° and -180$\leq \phi \leq$180. This allows more accurate prediction of the aircraft's attitude over a longer period of time and thus, would result in more accurate air data estimates.

2. **Nonlinear Gravity Term**
   The next improvement to the linear model can be made by modifying the contribution of the acceleration due to gravity on the linear aircraft dynamic model. Closer examinations of the linear model show that the terms $X_\theta \Delta\theta$, $Y_\phi \Delta\phi$,

and $Z_\theta \Delta\theta$ are obtained by using small angle perturbation of the projection of gravity on F_B. As the aircraft's attitude gets further away from trim, this approximation would result in erroneous airspeed estimate.

The modification shold retain the higher order terms when expanding the gravity contribution. Fortunately, when attitude is propagated using the nonlinear kinematics equation as previously suggested, this could easily achieved by using,

$$\Delta \mathbf{F}_{\text{grav}} = \begin{bmatrix} -g\sin\theta \\ g\cos\theta\sin\phi \\ g\cos\theta\cos\phi \end{bmatrix} - \begin{bmatrix} -g\sin\bar{\theta} \\ g\cos\bar{\theta}\sin\bar{\phi} \\ g\cos\bar{\theta}\cos\bar{\phi} \end{bmatrix} \tag{3.43}$$

which effectively gets rid of the small angle approximation.

3. **Stochastic Aircraft Model**

   Because the entries of **A** and **B** matrices are estimated using noisy sensor measurement data, they might be erroneous. Thus, treating aircraft dynamics as a deterministic model would be naive. One way to improve the dynamic model is by augmenting each differential equations with a bias term that is constantly estimated by the filter. While this term might be small and negligible for the nonlinear model, it might not always be the case for the linear aircraft dynamic model. The local approximation effect such as trim mismatch and dynamic decoupling could be significant in some maneuvers. Adding this bias term allows us to account for these errors so that the quality of the aircraft state prediction is improved.

   Trim mismatch is an issue that would affect the accuracy of the prediction from the dynamic model. In practice, the trim condition could vary slightly from one flight to another. Because the trim values must be subtracted off of the actual values before being used in Equations (3.30) and (3.33), error in the actual trim value will affect the accuracy of the aircraft states. The addition of a bias state

on $\Delta\dot{u}$ can be justified as follows.

$$\begin{aligned}\Delta\dot{u}_k &= X_u(u-(\bar{u}-\delta\bar{u}))+X_w(w-(\bar{w}-\delta\bar{w}))+X_q(q-(\bar{q}-\delta\bar{q}))+\dots \\ &= X_u(u-\bar{u})+X_w(w-\bar{w})+X_q(q-\bar{q})+\cdots+\underbrace{(X_u\delta\bar{u}+X_w\delta\bar{w}+X_q\delta\bar{q}+\dots)}_{X_b}\end{aligned} \tag{3.44}$$

where $\delta\bar{u}$, $\delta\bar{w}$, $\delta\bar{q}$, etc are error in trim values. Individually they are not observable, however their aggregate contribution on the error in u could be estimated.

In addition to trim mismatch, the parameters X_u, X_w, etc., as obtained from the system identification process are not perfect. Their effects on $\Delta\dot{u}$ is given by:

$$\begin{aligned}\Delta\dot{u}_k &= (X_u+\delta X_u)\Delta u+(X_w+\delta X_w)\Delta w+(X_q+\delta X_q)\Delta q+\dots \\ &= X_u\Delta u+X_w\Delta w+X_q\Delta q+\cdots+\underbrace{(\delta X_u\Delta u+\delta X_w\Delta w+\delta X_q\Delta q+\dots)}_{X_b}\end{aligned} \tag{3.45}$$

In this case, X_b is time varying. A similar argument can be made to augment the equations for $\Delta\dot{v}$, $\Delta\dot{w}$, $\Delta\dot{p}$, $\Delta\dot{q}$, $\Delta\dot{r}$ with Y_b, Z_b, $\mathcal{L}_b$, $\mathcal{M}_b$, and $\mathcal{N}_b$ respectively.

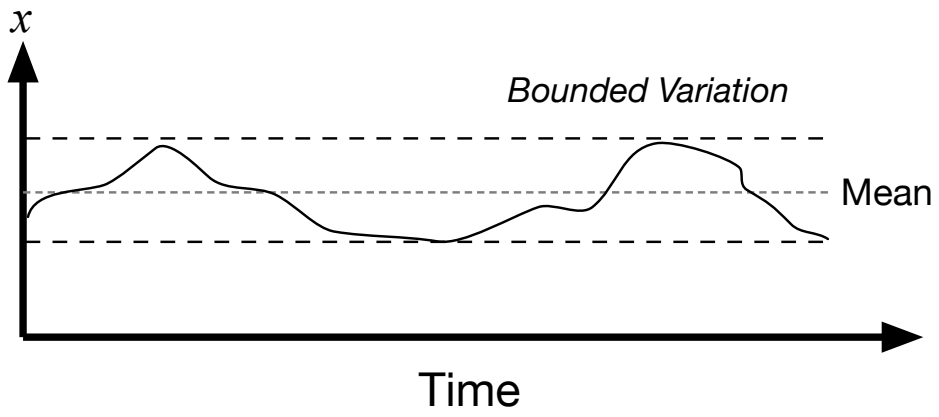

Figure 3.4: First-order Gauss Markov Process

The combination of error in the trim condition and error in parameters results in bias terms that are time varying about a certain mean value like shown on Figure 3.4. Here, the dynamics variation is not known ahead of time but it is bounded. Such process is often modeled as a first-order Gauss Markov process [56]. This process models the vector of bias terms, $\mathbf{b}_{\text{Aero}}$, as:

$$\mathbf{b}_{\text{Aero}} = \bar{\mathbf{b}}_{\text{Aero}} + \delta\mathbf{b}_{\text{Aero}} \tag{3.46}$$

where $\bar{\mathbf{b}}_{\text{Aero}}$ is the bias's mean value and $\delta\mathbf{b}_{\text{Aero}}$ is a variation around the mean. The mean value is assumed to be constant and $\delta\mathbf{b}_{\text{Aero}}$ is a zero-mean stochastic process defined as follows:

$$\delta\dot{\mathbf{b}}_{\text{Aero}} = \mathbf{\Phi}_b \cdot \delta\mathbf{b}_{\text{Aero}} + \mathbf{n}_{\text{Aero}} \tag{3.47}$$

where $\mathbf{n}_{\text{Aero}}$ is a vector of uncorrelated, zero mean Gaussian white noise with covariance matrix $\mathbf{Q}_{\text{Aero}}$. The matrix $\mathbf{\Phi}_b$ is a diagonal matrix that has the correlation time constant of each bias terms, that is:

$$\mathbf{\Phi}_b = \text{diag}\left[-\frac{1}{\tau_X}, \quad -\frac{1}{\tau_Y}, \quad -\frac{1}{\tau_Z}, \quad -\frac{1}{\tau_{\mathcal{L}}}, \quad -\frac{1}{\tau_{\mathcal{M}}}, \quad -\frac{1}{\tau_{\mathcal{N}}} \right] \tag{3.48}$$

The matrix $\mathbf{Q}_{\text{Aero}}$ is a diagonal matrix given by:

$$\mathbf{Q}_{\text{Aero}} = \text{diag}\left[\frac{2\sigma_X^2}{\tau_X}, \quad \frac{2\sigma_Y^2}{\tau_Y}, \quad \frac{2\sigma_Z^2}{\tau_Z}, \quad \frac{2\sigma_{\mathcal{L}}^2}{\tau_{\mathcal{L}}}, \quad \frac{2\sigma_{\mathcal{M}}^2}{\tau_{\mathcal{M}}}, \quad \frac{2\sigma_{\mathcal{N}}^2}{\tau_{\mathcal{N}}} \right] \tag{3.49}$$

This process has been widely used to model similar process such as to model inertial sensor bias [43, 57].

The time update process for the linear dynamic model used in the synthetic air

data estimator can be summarized as follows. Consider an augmented $\mathbf{x}_{\text{ac}}$ defined as:

$$\mathbf{x}_{\text{ac}} = \begin{bmatrix} \mathbf{V}_{WB}^{B} \\ \boldsymbol{\omega}^{B} \\ \boldsymbol{\Psi} \\ \mathbf{b}_{\text{Aero}} \end{bmatrix} \tag{3.50}$$

and the same flight control input vector as defined in (3.22). The perturbation of $\mathbf{x}_{\text{ac}}$ defined in Equation (3.50) is updated using the following equations. The differential equations for the airspeed vector components are:

$$\begin{bmatrix} \Delta\dot{u} \\ \Delta\dot{v} \\ \Delta\dot{w} \end{bmatrix} = \begin{bmatrix} X_u & 0 & X_w \\ 0 & Y_v & 0 \\ Z_u & 0 & Z_w \end{bmatrix} \begin{bmatrix} \Delta u \\ \Delta v \\ \Delta w \end{bmatrix} + \begin{bmatrix} 0 & X_q & 0 \\ Y_p & 0 & Y_r \\ 0 & Z_q & 0 \end{bmatrix} \begin{bmatrix} \Delta p \\ \Delta q \\ \Delta r \end{bmatrix} + \Delta\mathbf{F}_{\text{grav}} + \begin{bmatrix} X_{\delta_e} & 0 & 0 \\ 0 & Y_{\delta_a} & Y_{\delta_r} \\ Z_{\delta_e} & 0 & 0 \end{bmatrix} \begin{bmatrix} \Delta\delta_e \\ \Delta\delta_a \\ \Delta\delta_r \end{bmatrix} + \begin{bmatrix} \frac{\Delta T}{m} \\ 0 \\ 0 \end{bmatrix} + \begin{bmatrix} X_b \\ Y_b \\ Z_b \end{bmatrix} \tag{3.51}$$

and for the rotation rates:

$$\begin{bmatrix} \Delta\dot{p} \\ \Delta\dot{q} \\ \Delta\dot{r} \end{bmatrix} = \begin{bmatrix} 0 & \mathcal{L}_v & 0 \\ \mathcal{M}_u & 0 & \mathcal{M}_w \\ 0 & \mathcal{N}_v & 0 \end{bmatrix} \begin{bmatrix} \Delta u \\ \Delta v \\ \Delta w \end{bmatrix} + \begin{bmatrix} \mathcal{L}_p & 0 & \mathcal{L}_r \\ 0 & \mathcal{M}_q & 0 \\ \mathcal{N}_p & 0 & \mathcal{N}_r \end{bmatrix} \begin{bmatrix} \Delta p \\ \Delta q \\ \Delta r \end{bmatrix} + \begin{bmatrix} 0 & \mathcal{L}_{\delta_a} & \mathcal{L}_{\delta_r} \\ \mathcal{M}_{\delta_e} & 0 & 0 \\ 0 & \mathcal{N}_{\delta_a} & \mathcal{N}_{\delta_r} \end{bmatrix} \begin{bmatrix} \Delta\delta_e \\ \Delta\delta_a \\ \Delta\delta_r \end{bmatrix} + \begin{bmatrix} \frac{\Delta\mathcal{T}}{I_x} \\ 0 \\ 0 \end{bmatrix} + \begin{bmatrix} \mathcal{L}_b \\ \mathcal{M}_b \\ \mathcal{N}_b \end{bmatrix} \tag{3.52}$$

The Euler angles are propagated using Equation (3.16), and the aerodynamic bias terms are propagated as constants (because $\mathbb{E}(\delta\mathbf{b}_{\text{Aero}}) = 0$).

The Kalman filter is still formulated in terms of the error states and the covariance of these error states are updated using an equation similar to Equation (3.29) that has matrices defined in Appendix C.

3.3 Wind Model

As has been noted earlier in this chapter, wind is an integral part of synthetic air data estimation without which the estimates of V, α, and β would be inaccurate. If direct wind measurement of wind as a function of position were available, this would enable its use in the synthetic air data estimator. Providing wind measurements to the estimator in this manner is not practical. In practice, wind information is only available at discrete points separated miles away from each other. Thus, it has to be included in the state vector of the synthetic air data estimator so it could be estimated in real time. In the estimator, the wind field is modeled as a three dimensional vector that in the North-East-Down (NED) coordinate frame has the following components:

$$\widetilde{\mathbf{W}}^N = \begin{bmatrix} \widetilde{W}_N & \widetilde{W}_E & \widetilde{W}_D \end{bmatrix}^T \tag{3.53}$$

When flying in a local area, the wind field usually does not change very significantly in a short amount of time. Thus, it can be perfectly modeled as a constant value plus some variations [38–40]. It is, however, not possible to derive a useful model for this variation. For this reason, each component of $\widetilde{\mathbf{W}}^N$ is modeled as first-order Gauss Markov process to overbound the actual process. Each component has two tuning parameters (τ and σ) that could be designed to ensure the filter's robustness to variation in flying conditions.

Mathematically, the wind is modeled as follows:

$$\widetilde{\mathbf{W}}^N = \overline{\widetilde{\mathbf{W}}}^N + \delta\widetilde{\mathbf{W}}^N \tag{3.54}$$

where $\overline{\widetilde{\mathbf{W}}}^N$ is the mean wind field and $\delta\widetilde{\mathbf{W}}^N$ is the slow variation about that mean value. The first-order Gauss Markov process for the variation is given as follows:

$$\dot{\delta\widetilde{\mathbf{W}}}^N = \mathbf{\Phi}_W \cdot \delta\widetilde{\mathbf{W}}^N + \mathbf{n}_{\text{Wind}} \tag{3.55}$$

where

$$\mathbf{\Phi}_W = \text{diag}\begin{bmatrix} -\frac{1}{\tau_{W_N}}, & -\frac{1}{\tau_{W_E}}, & -\frac{1}{\tau_{W_N}} \end{bmatrix} \tag{3.56}$$

and the covariance matrix of the zero-mean Gaussian noise $\mathbf{n}_{\text{Wind}}$ is given by:

$$\mathbf{Q}_{\text{Wind}} = \text{diag}\left[\frac{2\sigma_{W_N}^2}{\tau_{W_N}}, \quad \frac{2\sigma_{W_E}^2}{\tau_{W_E}}, \quad \frac{2\sigma_{W_D}^2}{\tau_{W_D}} \right] \tag{3.57}$$

3.4 Summary

Aircraft dynamics is an essential component of a synthetic air data system. The EOM predict the time evolution of airspeed, angle of attack, and sideslip angle so the estimator can separate them from wind velocity vector. The estimator used in the system is an error state Kalman filter which can use either the nonlinear or linear aircraft dynamic model in its time update process. The equations for both nonlinear and the modified linear model has been detailed in this chapter. The next chapter presents challenges associated with fusing sensors with large output errors. As would be shown later, different fusion architecture is required in this case.

Chapter 4

Filter Architectures

There are several ways to mechanize a sensor fusion architecture to estimate V, α, and β from IMU outputs, GPS velocity measurements, and an aircraft dynamic model. What architecture a designer selects depends on many things including sensor quality and the availability (or lack thereof) of computational resources. There are tradeoffs involved in selecting one estimator architecture over another. The purpose of this chapter is to explore one of these key tradeoffs, namely the impact of inertial sensor quality.

4.1 Single Filter Architecture

One candidate is an estimator that has the functional block diagram in Figure 4.1. This is a logical extension of Wise's architecture [37] described earlier where airspeed, V is now an additional state to be estimated by the filter.

This filter architecture, in contrast with the second architecture which will be presented in the next section, is comprised of a single error state Kalman filter that uses the nonlinear aircraft dynamic model for its time update process. It has the

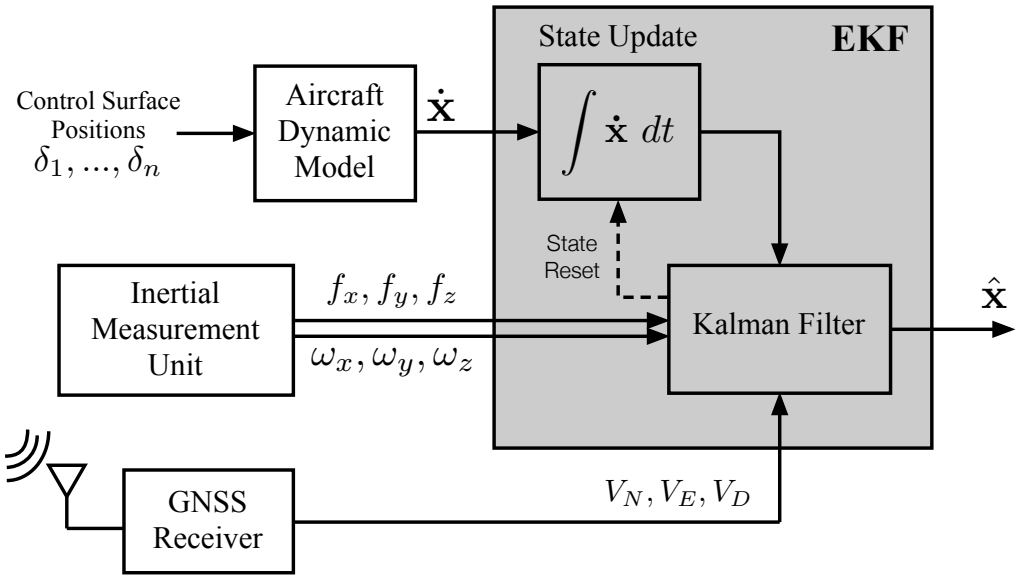

Figure 4.1: Single filter architecture for synthetic air data estimation

following state vector.

$$\mathbf{x} = \begin{bmatrix} \mathbf{V}_{WB}^{B} \\ \boldsymbol{\omega}^{B} \\ \boldsymbol{\Psi} \\ \widetilde{\mathbf{W}}^{N} \\ \mathbf{b}_a \\ \mathbf{b}_g \end{bmatrix} \tag{4.1}$$

where $\mathbf{b}_a$ and $\mathbf{b}_g$ are the accelerometer and gyro biases, respectively. The first three elements of $\mathbf{x}$ are parts of the aircraft state vector described in the previous chapter. Both $\mathbf{b}_a$ and $\mathbf{b}_g$ become part of the state vector when inertial sensors in the category identified by the moniker *automotive/consumer grade* (as defined in [57]) are used. The EOM propagate $\mathbf{V}_{WB}^{B}$ and $\boldsymbol{\omega}^{B}$ in time; attitude is propagated using the attitude kinematics; and, finally, wind, accelerometer bias, and gyro bias are assumed to be first order Gauss Markov processes.

Ground velocity vector measurement from a GPS receiver, specific force measurements from an accelerometer triad, and rotation rates from a gyro triad are used for measurement update which occurs at a rate lower than the time update rate.

In addition to Equation (3.1), gyro and accelerometer measurements can be related to the state vector as follows. Measurements from the rate gyros, $\boldsymbol{\omega}_{\text{gyro}}$, are direct observations of $\boldsymbol{\omega}^B$ plus bias (or null shift) and noise, or mathematically:

$$\boldsymbol{\omega}_{\text{gyro}} = \boldsymbol{\omega}^B + \mathbf{b}_g + \mathbf{n}_{\text{gyro}} \tag{4.2}$$

where $\mathbf{n}_{\text{gyro}}$ denotes the random noise that corrupts the gyro outputs.

The accelerometers output specific force measurements along each of the body axes of the aircraft. Specific forces are the sum of all forces except gravity acting on the aircraft per unit mass. They are also typically corrupted by sensor bias and noise. Mathematically, they can be written as

$$\begin{aligned} \mathbf{f} &= \frac{\sum \mathbf{F} - \mathbf{F}_{\text{gravity}}}{m} + \mathbf{b}_a + \mathbf{n}_a \\ &= \frac{(\mathbf{F}_{\text{Aero}} + \mathbf{F}_{\text{Propulsion}})}{m} + \mathbf{b}_a + \mathbf{n}_a \end{aligned} \tag{4.3}$$

Both aerodynamic forces $\mathbf{F}_{\text{Aero}}$ and propulsion force $\mathbf{F}_{\text{Propulsion}}$ are typically functions of $\mathbf{V}_{WB}^B$, $\boldsymbol{\omega}^B$, and $\boldsymbol{\mathcal{U}}$, or

$$\begin{aligned} \mathbf{F}_{\text{Aero}} &= \mathbf{F}_{\text{Aero}}\left(\mathbf{V}_{WB}^B, \boldsymbol{\omega}^B, \boldsymbol{\mathcal{U}}\right) \\ \mathbf{F}_{\text{Propulsion}} &= \mathbf{F}_{\text{Propulsion}}\left(\mathbf{V}_{WB}^B, \boldsymbol{\omega}^B, \boldsymbol{\mathcal{U}}\right) \end{aligned} \tag{4.4}$$

As will be shown later in this chapter, this architecture fails to estimate V, α, and β accurately when low cost inertial sensors are used. To understand why this is the case, we look at a two-dimensional (2-D) analysis of the problem. This simplification allows us to gain insight into the issues without the complexity of a 3-D problem nor the loss of generality. In the 2-D plane, the aircraft is constrained to fly in the North-East plane and we are interested in estimating the 2-D components of the airspeed vector, u and v, from North and East ground velocity observations. The relationships between u, v, V_N, and V_E are shown on Equation (4.5).

$$\begin{aligned} V_N(t) &= u(t)\cos\psi(t) - v(t)\sin\psi(t) + \widetilde{W}_N(t) \\ V_E(t) &= u(t)\sin\psi(t) + v(t)\cos\psi(t) + \widetilde{W}_E(t) \end{aligned} \tag{4.5}$$

Assuming constant airspeed, steady atmosphere, and *known* yaw angle, Equation (4.5) can be recast in a matrix form as follows:

$$\underbrace{\begin{bmatrix} V_N(t_1) \\ V_E(t_1) \\ V_N(t_2) \\ V_E(t_2) \end{bmatrix}}_{\mathbf{y}} = \underbrace{\begin{bmatrix} \cos\psi(t_1) & -\sin\psi(t_1) & 1 & 0 \\ \sin\psi(t_1) & \cos\psi(t_1) & 0 & 1 \\ \cos\psi(t_2) & -\sin\psi(t_2) & 1 & 0 \\ \sin\psi(t_2) & \cos\psi(t_2) & 0 & 1 \end{bmatrix}}_{\mathcal{H}} \underbrace{\begin{bmatrix} u \\ v \\ \widetilde{W}_N \\ \widetilde{W}_E \end{bmatrix}}_{\mathbf{x}} \tag{4.6}$$

When $\psi(t_1) \neq \psi(t_2)$, $\mathcal{H}$ is full rank and can be inverted to solve for the state vector $\mathbf{x}$. To account for noise in the ground velocity measurements, least squares techniques can be employed. For example, Equation (4.7) can be used in processing a batch of measurements to estimate u, v, W_N, and W_E.

$$\hat{\mathbf{x}} = \left(\mathcal{H}^T \mathbf{R}^{-1} \mathcal{H}\right)^{-1} \mathcal{H}^T \mathbf{R}^{-1} \mathbf{y} \tag{4.7}$$

The matrix $\mathbf{R}$ is the noise covariance matrix of the ground velocity measurements coming from GPS. The above argument shows that it is possible to estimate airspeed vector from groundspeed vector measurements when there is change in the aircraft's heading. In the 3-D case, change in airplane's attitude is required for observability. Conversely, airspeed is not observable during a straight flight.

The requirement to know heading perfectly is unrealistic. In reality, the measurement would be corrupted by noise or even biased which would make the assumption in the earlier argument invalid. We model this situation by adding a bias term that would account for unmodeled heading errors. Applying this modification to Equation (4.5), we have:

$$\begin{aligned} V_N(t) &= u(t)\cos\left[\psi_m(t) - \psi_b(t)\right] - v(t)\sin\left[\psi_m(t) - \psi_b(t)\right] + \widetilde{W}_N(t) \\ V_E(t) &= u(t)\sin\left[\psi_m(t) - \psi_b(t)\right] + v(t)\cos\left[\psi_m(t) - \psi_b(t)\right] + \widetilde{W}_E(t) \end{aligned} \tag{4.8}$$

Now the state vector is given by $\mathbf{x} = [\ u \ \ v \ \ \psi_b \ \ \widetilde{W}_N \ \ \widetilde{W}_E\ ]^T$. This modification makes Equation (4.8) nonlinear but can be solved iteratively by linearizing about an *a priori*

estimate of $\mathbf{x}$.

Linearizing Equation (4.8) about the estimate of $\mathbf{x}$ (denoted as $\hat{\mathbf{x}}$):

$$\begin{bmatrix} \delta V_N(t_1) \\ \delta V_E(t_1) \\ \delta V_N(t_2) \\ \delta V_E(t_2) \\ \vdots \end{bmatrix} = \underbrace{\begin{bmatrix} \cos\hat{\psi}(t_1) & -\sin\hat{\psi}(t_1) & \hat{u}\sin\hat{\psi}(t_1) + \hat{v}\cos\hat{\psi}(t_1) & 1 & 0 \\ \sin\hat{\psi}(t_1) & \cos\hat{\psi}(t_1) & -\hat{u}\cos\hat{\psi}(t_1) + \hat{v}\sin\hat{\psi}(t_1) & 0 & 1 \\ \cos\hat{\psi}(t_2) & -\sin\hat{\psi}(t_2) & \hat{u}\sin\hat{\psi}(t_2) + \hat{v}\cos\hat{\psi}(t_2) & 1 & 0 \\ \sin\hat{\psi}(t_2) & \cos\hat{\psi}(t_2) & -\hat{u}\cos\hat{\psi}(t_2) + \hat{v}\sin\hat{\psi}(t_2) & 0 & 1 \\ & & \vdots & & \end{bmatrix}}_{\mathcal{H}} \begin{bmatrix} \delta u \\ \delta v \\ \delta\psi_b \\ \delta\widetilde{W}_N \\ \delta\widetilde{W}_E \end{bmatrix} \tag{4.9}$$

where $\hat{\psi}(t) = \psi_m(t) - \hat{\psi}_b$. The left hand side of Equation (4.9) is the innovation process and it is calculated as follows:

$$\begin{aligned} \delta V_N(t) &= V_N(t) - [\hat{u}\cos\hat{\psi}(t) - \hat{v}\sin\hat{\psi}(t) + \hat{\widetilde{W}}_N] \\ \delta V_E(t) &= \underbrace{V_E(t)}_{\text{GPS}} - \underbrace{[\hat{u}\sin\hat{\psi}(t) + \hat{v}\cos\hat{\psi}(t) + \hat{\widetilde{W}}_E]}_{\text{Filter Estimates}} \end{aligned} \tag{4.10}$$

This, however, will not result in a converging $\hat{\mathbf{x}}$ because $\mathcal{H}$ in Equation (4.9) is rank deficient; the third column of $\mathcal{H}$ is a linear combination of its first and second columns. In this formulation, heading error is unobservable. Stated differently, it is not possible to estimate both airspeed and attitude solely from ground velocity measurements.

This problem can only be overcome by bringing in new measurements that would provide an information path to estimate the unobservable state which in this case is the heading error state. Here, accelerometers and gyros are the candidate sensors. Gyro measurements are functions neither of heading angle nor of the velocity components and thus would not make $\mathcal{H}$ full rank.

Accelerometer measurements, however, are functions of u and v (and, in 3-D w) and so have the potential to make this problem fully observable. Ignoring the accelerometer bias for now, Equation (4.3) linearized about $\hat{\mathbf{x}}$ is shown in Equation

(4.11).

$$\begin{bmatrix} \delta f_x \\ \delta f_y \end{bmatrix} = \underbrace{\begin{bmatrix} \frac{\partial(F_{x,\text{Aero}} + F_{x,\text{Propulsion}})}{\partial u} & \frac{\partial(F_{x,\text{Aero}} + F_{x,\text{Propulsion}})}{\partial v} & 0 & 0 & 0 \\ \frac{\partial(F_{y,\text{Aero}} + F_{y,\text{Propulsion}})}{\partial u} & \frac{\partial(F_{y,\text{Aero}} + F_{y,\text{Propulsion}})}{\partial v} & 0 & 0 & 0 \end{bmatrix}}_{\mathcal{H}_a} \begin{bmatrix} \delta u \\ \delta v \\ \delta\psi_b \\ \delta\widetilde{W}_N \\ \delta\widetilde{W}_E \end{bmatrix} \tag{4.11}$$

Stacking $\mathcal{H}$ and $\mathcal{H}_a$ indeed makes this estimation problem fully observable. This, however, is not very robust because it depends highly on the fidelity of the dynamic model to estimate the state vector $\mathbf{x}$. Additionally, when a low cost MEMS IMU is used, sensor biases are not small and cannot be ignored. When $\mathbf{x}$ includes accelerometer biases, so that the augmented state vector $\mathbf{x}' = \begin{bmatrix} \mathbf{x}^T & b_{ax} & b_{ay} \end{bmatrix}^T$, the augmented observation matrix, $\mathcal{H}'_a$, has the form of

$$\mathcal{H}'_a = \begin{bmatrix} \mathcal{H}_a & \mathbf{I}_2 \end{bmatrix} \tag{4.12}$$

where $\mathbf{I}_2$ is a 2×2 identity matrix. In this case, the problem is again unobservable because errors in u and v are indistinguishable from the accelerometer biases. When high quality inertial sensors are used, b_{ax} and b_{ay} are assumed to be very small or zero which makes the problem observable.

4.2 Federated Filter Architecture

A very similar problem to the one discussed in the previous section (from a filter design point of view) was encountered in [58] where conventional Kalman filter architecture is unable to estimate attitude and gyro bias during GPS outages. In that work, a cascaded filter architecture was used to constrain the estimation of different bias terms to their respective sub-system. It is shown that this method improves the quality of the estimates in GPS outages during which heading was unavailable (it was estimated using multiple antenna GPS system). Breaking a problem that involves estimating

several bias terms into two filters are not new. This approach has been studied in other context in the past [59, 60] and formally justified by Kasdin et al. [61]

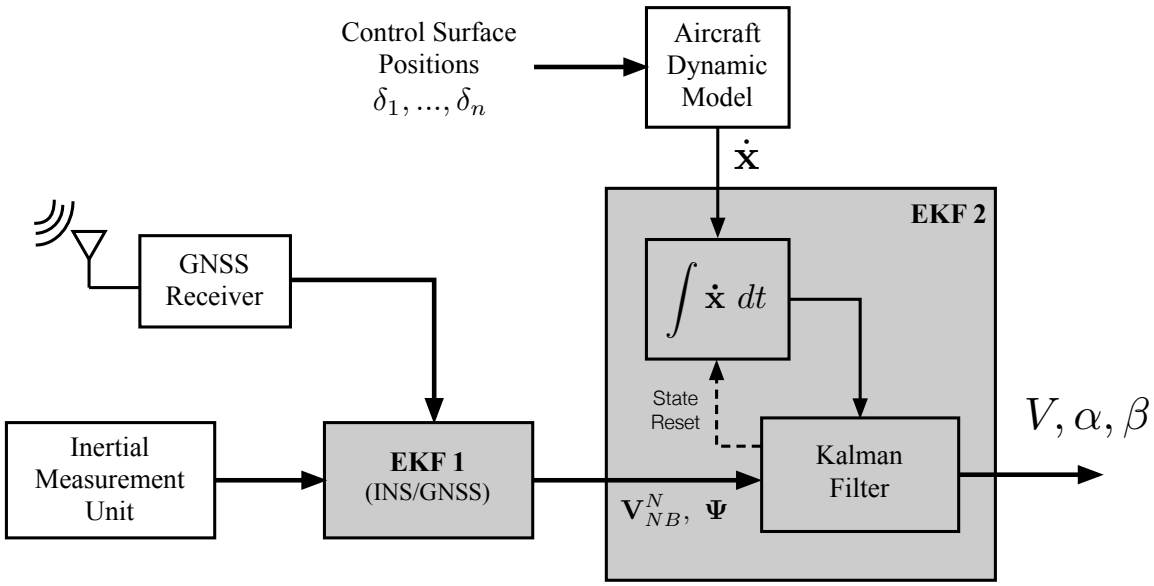

Figure 4.2: Federated filter architecture for synthetic air data estimation

In view of the above noted prior work, we propose a cascaded, two-filter architecture along the line of [58] to estimate V, α, and β. Figure 4.2 shows the functional block diagram of this architecture. In this formulation of the synthetic air data estimator, the low cost INS is fused with GPS in one filter. This filter generates an estimate of the airplane's position, groundspeed, and attitude as well as inertial sensor biases. Such filters are not new and have been the subject of many papers and books in the last decade, such as [43, 57, 62, 63]. The second filter uses the aircraft dynamic model for its time update equations and the outputs of the first filter as its measurement vector.

Although no new sensor is used in this architecture, it uses both the position and ground velocity measurements from the GPS receiver to estimate airspeed, angle of attack, and sideslip angle. In contrast, the architecture described in Section 4.1 only uses the ground velocity measurements. The addition of position information eliminates the unobservable mode described previously. Additionally, it prevents aircraft dynamic modeling error to corrupt the state estimates by not using raw

accelerometer measurements in the measurement update equation. Stated differently, the linearized observation matrix $\mathbf{H}$ would not be corrupted by any aircraft modeling error.

Since successive outputs of the first filter are correlated, this time correlation must be accounted for explicitly in the second filter. Although these additional states complicate the structure of the estimator, the added complexity is out-weighed by the ease with which one can impose state constraints thereby ensuring reasonably accurate estimates of V, α, and β.

When INS and GPS are combined, the blended navigation solution has the high bandwidth of the inertial sensors and the drift-free long term stability of the GPS solution. [43,57,62,63] The INS/GPS navigation solution consists of absolute position, velocity, and attitude that fully describe the aircraft's kinematics state. For the work described here, the INS/GPS filter is a 15-state extended Kalman filter like the one described in [57]. The output of this filter is the following state vector:

$$\mathbf{x}_1 = \begin{bmatrix} \mathbf{p} \\ \mathbf{V}_{NB}^N \\ \boldsymbol{\Psi} \\ \mathbf{b}_a \\ \mathbf{b}_g \end{bmatrix} \tag{4.13}$$

where $\mathbf{p}$ is the position vector containing the aircraft's latitude, longitude, and altitude. A subset of $\mathbf{x}_1$ is used as a measurement in the second filter. This is denoted $\mathbf{y}_2$ and is given by:

$$\mathbf{y}_2 = \begin{bmatrix} \mathbf{V}_{NB}^N \\ \boldsymbol{\Psi} \end{bmatrix} \tag{4.14}$$

The second filter extracts V, α, and β from the first filter using flight control inputs along with groundspeed and attitude estimates from the first navigation filter. As has been mentioned earlier, $\mathbf{y}_2$ is time-correlated. This time correlation will be accounted for by augmenting Filter 2 with six additional states. Therefore, the state

vector in the second filter consists of the following states:

$$\mathbf{x}_2 = \begin{bmatrix} \mathbf{V}_{WB}^B \\ \boldsymbol{\omega}^B \\ \boldsymbol{\Psi} \\ \mathbf{W}^N \\ \mathbf{b}_{\boldsymbol{\Psi}} \end{bmatrix} \tag{4.15}$$

Here, $\mathbf{W}^N = [\ W_N \ \ W_E \ \ W_D\ ]^T$, $\mathbf{b}_{\boldsymbol{\Psi}} = [\ b_\phi \ \ b_\theta \ \ b_\psi\ ]^T$ are terms that account for the time correlation in the measurements used in the second filter. Because the time correlation of the groundspeed estimates from the first filter is not separable from the wind, $\mathbf{W}^N$ is called the pseudo-wind estimate since it includes both the the wind ($\widetilde{\mathbf{W}}^N$) and the groundspeed measurements' correlation. These states are also modeled as first-order Gauss Markov process [49].

After augmenting the state with six additional correlated error states, the nonlinear measurement equation can be written as:

$$\mathbf{y}_2 = \mathbf{h}(\mathbf{x}_2) + \mathbf{n}_y \tag{4.16}$$

$$\underbrace{\begin{bmatrix} \mathbf{V}_{NB}^N \\ \boldsymbol{\Psi} \end{bmatrix}}_{\text{Filter 1}} = \begin{bmatrix} \mathbf{C}_B^N & \mathbf{0}_{3\times3} \\ \mathbf{0}_{3\times3} & \mathbf{I}_{3\times3} \end{bmatrix} \begin{bmatrix} \mathbf{V}_{WB}^B \\ \boldsymbol{\Psi} \end{bmatrix} + \begin{bmatrix} \mathbf{W}^N \\ \mathbf{b}_{\boldsymbol{\Psi}} \end{bmatrix} + \mathbf{n}_y \tag{4.17}$$

where $\mathbf{n}_y$ denotes the measurement noise or the uncertainty in the groundspeed and attitude measurements. After separating the time correlated error from the total uncertainty in the measurement, $\mathbf{n}_y$ can be assumed to be uncorrelated in time (i.e., white) but its elements are still correlated with each other. This inter-state correlation is captured in the state covariance from the first filter. Hence the measurement noise covariance matrix $\mathbf{R} = \mathbb{E}\left(\mathbf{n}_y \mathbf{n}_y^T\right)$ can be extracted from it. Mathematically,

$$\mathbf{R} = \begin{bmatrix} \mathbf{P}_1(4,4) & \cdots & \mathbf{P}_1(4,9) \\ & \ddots & \\ \mathbf{P}_1(9,4) & \cdots & \mathbf{P}_1(9,9) \end{bmatrix} \tag{4.18}$$

where $\mathbf{P}_1(i,j)$ denotes the (i,j)-th element $(i,j=1,\ldots,15)$ of the matrix $\mathbf{P}_1$.

To use Equation (4.17) in the error state EKF setting, it must be linearized and expressed in terms of the error state $\delta\mathbf{x}_2$, such that

$$\delta\mathbf{y}_2 = \mathbf{H}(\hat{\mathbf{x}}_2)\cdot\delta\mathbf{x}_2 + \mathbf{n}_y \tag{4.19}$$

where

$$\begin{aligned}\delta\mathbf{y}_2 &= \mathbf{y}_2 - \mathbf{h}(\hat{\mathbf{x}}_2)\\ &= \begin{bmatrix}\delta\mathbf{y}_{\mathrm{GS}}\\ \delta\mathbf{y}_{\Psi}\end{bmatrix}\end{aligned} \tag{4.20}$$

Both $\delta\mathbf{y}_{\mathrm{GS}}$ and $\delta\mathbf{y}_{\Psi}$ are defined as follows:

$$\begin{aligned}\delta\mathbf{y}_{\mathrm{GS}} &= \mathbf{V}_{NB}^{N}\big|_{\text{Filter 1}} - \left(\hat{\mathbf{C}}_B^N\hat{\mathbf{V}}_{WB}^B + \hat{\mathbf{W}}^N\right)\\ \delta\mathbf{y}_{\Psi} &= \begin{bmatrix}-\delta\check{\mathbf{C}}(2,3) & \delta\check{\mathbf{C}}(1,3) & -\delta\check{\mathbf{C}}(1,2)\end{bmatrix}^T - \hat{\mathbf{b}}_{\boldsymbol{\Psi}}\end{aligned} \tag{4.21}$$

and $\delta\check{\mathbf{C}}$ is defined as:

$$\delta\check{\mathbf{C}} = \mathbf{C}_B^N\big|_{\text{Filter 1}}\,\hat{\mathbf{C}}_N^B - \mathbf{I}_{3\times3} \tag{4.22}$$

The linearized measurement matrix $\mathbf{H}(\hat{\mathbf{x}}_2)$ is given by:

$$\mathbf{H} = \begin{bmatrix}\hat{\mathbf{C}}_B^N & \mathbf{0}_{3\times3} & \left[\left(\hat{\mathbf{C}}_B^N\hat{\mathbf{V}}_{WB}^B\right)\times\right] & \mathbf{I}_{3\times3} & \mathbf{0}_{3\times3}\\ \mathbf{0}_{3\times3} & \mathbf{0}_{3\times3} & \mathbf{I}_{3\times3} & \mathbf{0}_{3\times3} & \mathbf{I}_{3\times3}\end{bmatrix} \tag{4.23}$$

where $[\mathbf{a}\times]$ denotes the skew symmetric matrix:

$$[\mathbf{a}\times] = \begin{bmatrix}0 & -a_3 & a_2\\ a_3 & 0 & -a_1\\ -a_2 & a_1 & 0\end{bmatrix} \tag{4.24}$$

The measurement update at time step k is done as follows: The Kalman gain $\mathbf{K}$

and error state covariance matrix are calculated using:

$$\begin{aligned}\mathbf{K}(k) &= \mathbf{P}_2^-(k)\mathbf{H}^T(k)\left[\mathbf{H}(k)\mathbf{P}_2^-(k)\mathbf{H}^T(k)+\mathbf{R}(k)\right]^{-1}\\ \mathbf{P}_2^+(k) &= (\mathbf{I}-\mathbf{K}(k)\mathbf{H}(k))\mathbf{P}_2^-(k)\end{aligned} \tag{4.25}$$

where the superscript $-$ and $+$ indicates the quantity before and after the measurement update. The error state are calculated using:

$$\delta\hat{\mathbf{x}}_2(k) = \mathbf{K}(k)\delta\mathbf{y}_2(k) \tag{4.26}$$

And after updating $\hat{\mathbf{x}}_2$, the error state $\delta\hat{\mathbf{x}}_2$ is reset to zero [41]. The actual state vector is updated as follows:

$$\begin{aligned}\hat{\mathbf{V}}_{WB}^{B\,+} &= \hat{\mathbf{V}}_{WB}^{B\,-} + \delta\hat{\mathbf{V}}_{WB}^{B}\\ \hat{\boldsymbol{\omega}}^{B\,+} &= \hat{\boldsymbol{\omega}}^{B\,-} + \delta\hat{\boldsymbol{\omega}}^{B}\\ \hat{\mathbf{C}}_B^{N\,+} &= \left(\mathbf{I}-\left[\delta\hat{\boldsymbol{\Psi}}\times\right]\right)\hat{\mathbf{C}}_B^{N\,-}\\ \hat{\mathbf{W}}^{N\,+} &= \hat{\mathbf{W}}^{N\,-} + \delta\hat{\mathbf{W}}^{N}\\ \hat{\mathbf{b}}_{\boldsymbol{\Psi}}{}^{+} &= \hat{\mathbf{b}}_{\boldsymbol{\Psi}}{}^{-} + \delta\hat{\mathbf{b}}_{\boldsymbol{\Psi}}\end{aligned} \tag{4.27}$$

4.3 Architecture Validation

Both filter architectures described above are validated using a series of simulation flight tests. The simulated flight data was obtained using an ATC 710 M flight simulator which is a single-engine FAA level 3 flight training device that uses Flight Gear as its core simulator. The data simulates a Cessna 172 maneuvering at an altitude of approximately 1000 ft. The aerodynamic model of the aircraft is known from the aircraft configuration files. Appendix A lists the aerodynamic coefficients used in the force and moment computation. The maneuvers executed during the flight are summarized in Table 4.1 and depicted on Figure 4.3.

Some of these are aggressive maneuvers in that they involve large changes in angles of attack, sideslip and attitude. Since the simulator was handflown, the numbers mentioned above are approximate values as the true value changes during the ma-

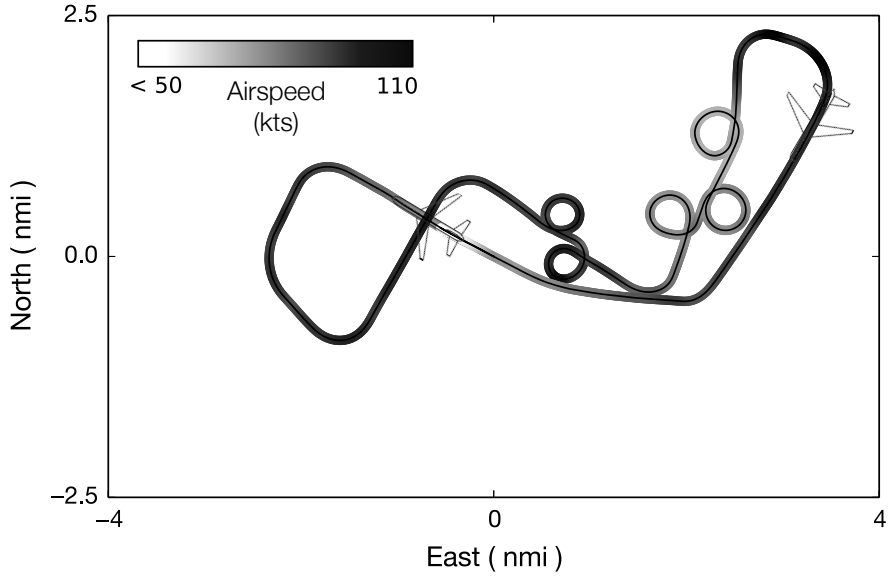

4.3(a)

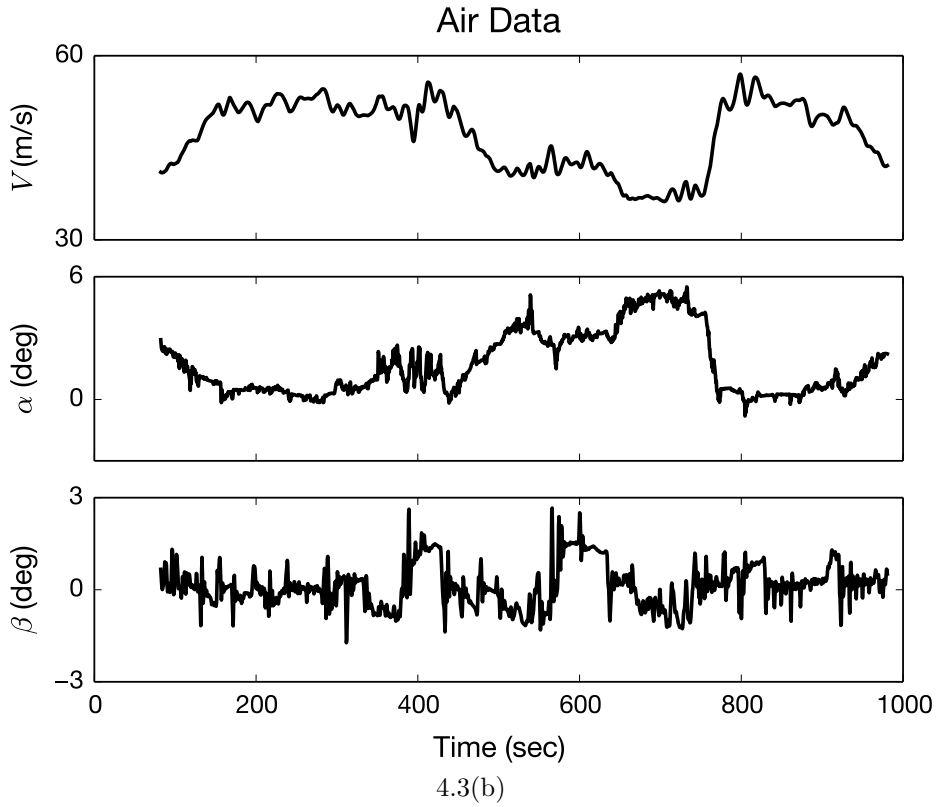

4.3(b)

Figure 4.3: Simulation trajectory depicting position and airspeed correlation

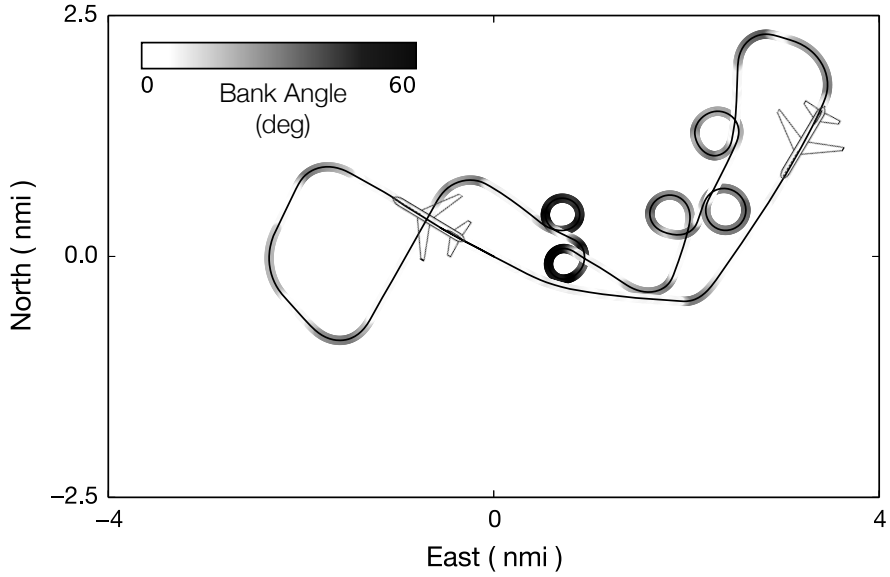

4.3(c)

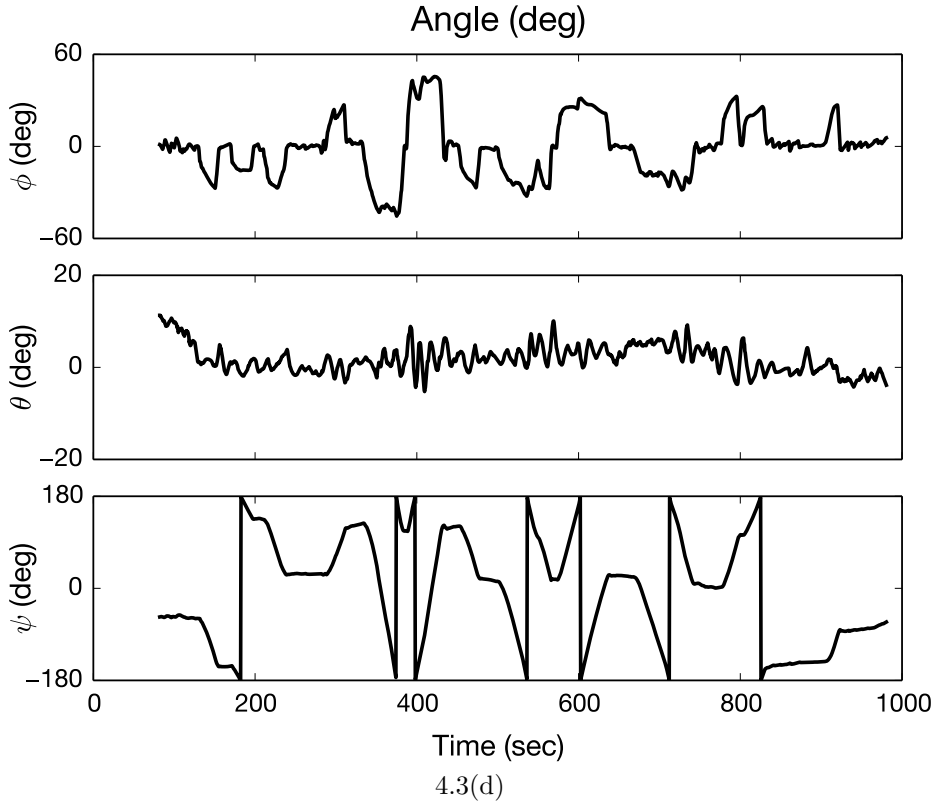

4.3(d)

Figure 4.3: Simulation Trajectory

Maneuver 1:	200-400 sec 500-600 sec 1000-1200 sec	± 30° bank, 100 knots.
Maneuver 2:	400-500 sec	± 50° bank turns, 100 knots.
Maneuver 3:	600-800 sec	± 30° bank turns, 70 knots.
Maneuver 4:	800-950 sec	± 30° bank turns, 80 knots.

Table 4.1: Simulation Maneuvers

neuver as a function of pilot skill. In the simulation, the wind was blowing from the North at 5 knots.

Because the dynamic model does not include ground reaction forces, the synthetic air data filter can only run after the aircraft is airborne. There are two ways in which we can detect whether the airplane is airborne. First, we can assume that airplane is not airborne until the speed is about 1.2 times greater than the airplane's stall speed. An alternative method would be to start the filter by looking at the first time the aircraft has a positive climb rate. The first approach is used in the following simulation studies. In the cascaded filter architecture, the first filter runs independently of the second filter, and the second filter is initialized as soon as the aircraft gets airborne.

The Filter 2 parameters described in Section 4.2 (and Chapter 3) used in this simulation study are described as follows. The state vector $\hat{\mathbf{x}}_2$ is initialized partially using estimates from the first filter. Unknown quantities like angle of attack, sideslip angle, and wind are initialized at zero. This is compensated by putting a rather large initial variance on each of these unknown states. The initial estimate of $\mathbf{x}_2$ is shown on Equation (4.28).

$$\begin{aligned} \hat{\mathbf{V}}_{WB}^{B} &= \left[\begin{array}{ccc} \sqrt{V_N^2 + V_E^2 + V_D^2} & 0 & 0 \end{array} \right]_{\text{Filter 1}} \\ \hat{\boldsymbol{\omega}}^{B} &= \boldsymbol{\omega}_{\text{gyro}} - \mathbf{b}_g|_{\text{Filter 1}} \\ \hat{\boldsymbol{\Psi}} &= \hat{\boldsymbol{\Psi}}\Big|_{\text{Filter 1}} \\ \hat{\mathbf{W}}^{N} &= \hat{\mathbf{b}}_{\boldsymbol{\Psi}} = 0 \end{aligned} \tag{4.28}$$

The initial covariance is assumed to be diagonal with the following components.

$$\begin{aligned}\mathbf{P}_2 = \text{diag}\,[\; &\underbrace{(5\text{m/s})^2 \quad (2\text{m/s})^2 \quad (2\text{m/s})^2}_{\text{Airspeed}} \quad \dots \\ &\underbrace{\sigma_{gx}^2 \quad \sigma_{gy}^2 \quad \sigma_{gz}^2}_{\text{Body rates}} \quad \dots \\ &\underbrace{\mathbf{P}_1(7,7) \quad \mathbf{P}_1(8,8) \quad \mathbf{P}_1(9,9)}_{\text{Attitude}} \quad \dots \\ &\underbrace{(5\text{ m/s})^2 \quad (5\text{ m/s})^2 \quad (3\text{ m/s})^2}_{\text{Pseudo-wind}} \quad \dots \\ &\underbrace{(0.1^\circ)^2 \quad (0.1^\circ)^2 \quad (0.1^\circ)^2}_{\text{Correlated error}}\;] \end{aligned} \tag{4.29}$$

where σ_{gx}, σ_{gy}, and σ_{gz} are the standard deviations of the wide band noise on each of the rate gyro axis. In reality, the diagonal assumption on the initial covariance matrix is not generally true. However, the correlations among the initial states are often unavailable. The common practice is to let the filter resolve the correlation as it approaches steady state. The initial covariance of the airspeed should reflect the uncertainty of the wind field around the aircraft. Although the filter is not very sensitive to the initial variances of the airspeed and wind states, overconfidence on the initial wind estimate (i.e. small variance) leads to a slower convergence. The variances of the body rates are initialized using the noise level on the rate gyro used in simulation. On the other hand, since attitude is initialized as is using the first filter estimates, their variances can be directly taken from the first filter.

In this simulation, the flight control sampling frequency is 50 Hz ($T_s = 0.02$ sec), and the measurement update of the synthetic airdata system runs at 2.5 Hz. The process noise covariance and correlation times of the correlated error states are used as filter tuning parameter. This technique is commonly used to account for modeling uncertainty and linearization error. The result shown here will be for the following

process noise parameters.

$$\begin{gathered}\sigma_e = \sigma_a = \sigma_r = 0.5^\circ \\ \sigma_f = 200 \text{ rpm} \\ \sigma_{w_N} = \sigma_{w_E} = 0.1 \text{ m/s}, \quad \tau_{w_N} = \tau_{w_E} = 50 \text{ sec} \\ \sigma_{b_D} = 0.02 \text{ m/s}, \quad \tau_{b_D} = 100 \text{ sec} \\ \sigma_{b_\phi} = \sigma_{b_\theta} = \sigma_{b_\psi} = 0.01^\circ \ , \quad \tau_{b_\phi} = \tau_{b_\theta} = \tau_{b_\psi} = 100 \text{ sec}\end{gathered} \tag{4.30}$$

The result of running the single filter architecture described in Section 4.1 is shown in Figure 4.4. In this simulation, the noise in the control surface deflection measurements has the standard deviation of 0.7° and a low cost MEMS IMU is used. Plotted on Figure 4.4 are the airspeed error (δV), angle of attack error ($\delta\alpha$), and sideslip angle error ($\delta\beta$); and also the 3-σ bounds estimated by the EKF. This figure shows that this architecture results in diverging estimates. In contrast, when the inertial sensor biases are small and can be ignored (i.e., high quality IMU is used), the results shown on Figure 4.5 is obtained.

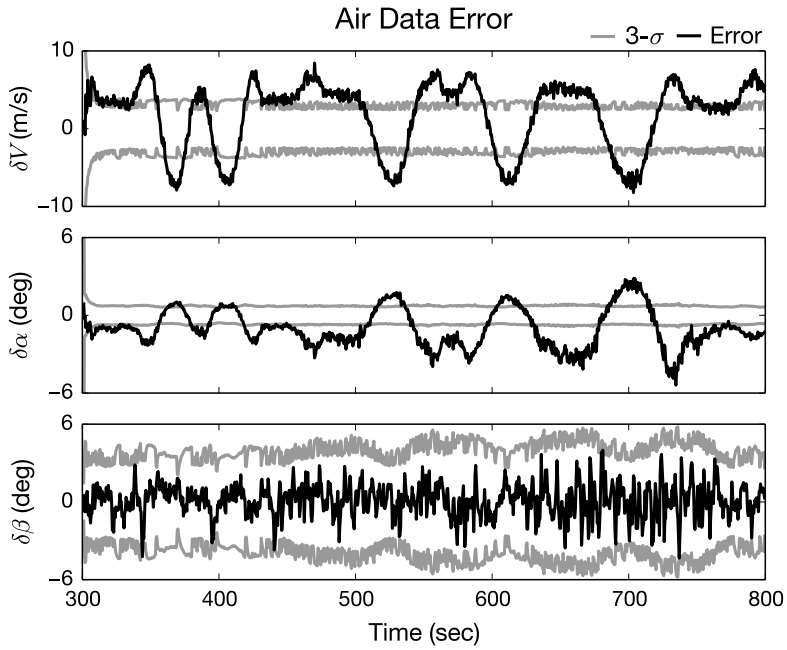

Figure 4.4: Accuracy of air data estimates using single filter architecture

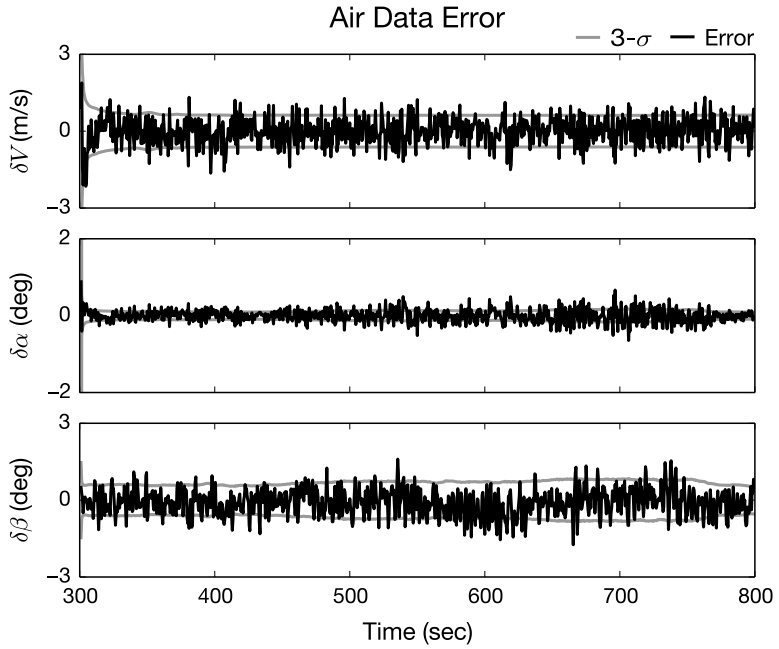

Figure 4.5: Accuracy of air data estimates with a high quality IMU ($\sigma_{\text{Accel}} = 0.5$ mg) and a high fidelity dynamic model

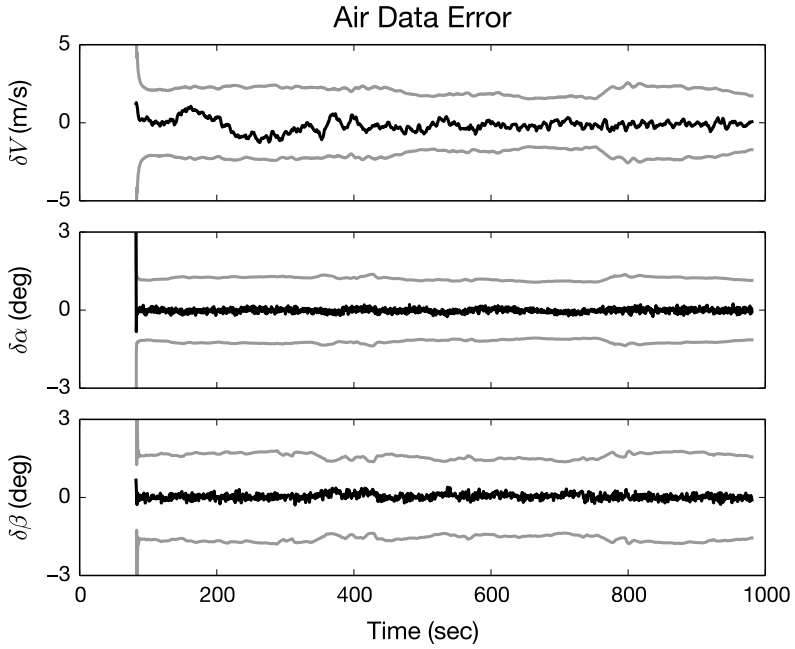

Figure 4.6: Performance of the federated architecture

Figures 4.4 and 4.5 are demonstrations of the issues higlighted in Section 4.1. The cascaded filter architecture, however, is robust to the sensor quality variation (cf. Section 4.2). Figure 4.6 plots the estimation error of V, α, and β and the 3-σ bound obtained from the filter. The transient experienced by the filter is relatively short and the estimated covariance is conservative. The error in airspeed estimate is, however, correlated, indicating that this architecture is not optimal.

4.4 Summary

The issues depicted in Figures 4.4 to 4.6 can be summarized in Figure 4.7. The quality of the sensor and dynamic model information used in the synthetic air data estimator has an effect on the choice of filter architecture. As the dynamic model becomes more inaccurate, the single filter architecture becomes less accurate and as the IMU quality degrades, more error states must be added which makes the problem unobservable. This tradeoff is depicted on Figure 4.7.

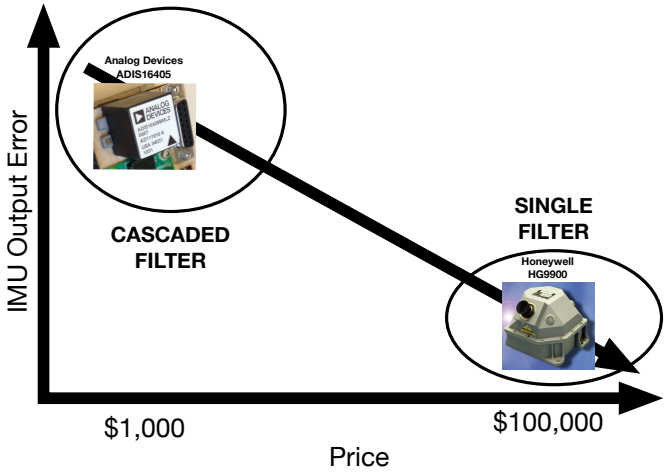

Figure 4.7: Sensor quality and filter architecture

Chapter 5

Experimental Validation

5.1 Flight Test Setup

Experimental validation of the synthetic airdata estimator was accomplished by post processing flight test data collected on an Ultra Stick 120[1] testbed. The Ultra Stick 120 used in this experiment is shown on Figure 5.1(a). It is a small uninhabited aerial vehicle formerly operated by NASA under the name FASER or Free-flying Aircraft for Sub-scale Experimental Research [64].

The airframe is a fixed-wing, radio controlled aircraft with standard elevator, aileron, and rudder control surfaces. These surfaces are actuated by means of electric servos, with a maximum deflection of 25 degrees in each direction. Thrust is generated by an Actro 40-4 brushless DC motor and regulated by a Castle Creations ICE2 HV80 speed controller. The motor is powered by two lithium polymer batteries in series which give endurance of approximately 30 minutes. The propeller used in this experiment is the APC 18×12 which performance has been measured through independent wind tunnel testings at the University.

The aircraft carries the Goldy flight control system (FCS). The Goldy FCS is a University of Minnesota custom flight control system that has an Analog Device ADIS16405 IMU and a Hemisphere Crescent GPS receiver as primary navigation sensors. The air data system consists of AMS 5812 pressure transducers that make up the pitot-static system, and wingtip vanes [65] to measure angle of attack and

[1]URL: http://www.horizonhobby.com/products/ultra-stick-lite-120-arf-HAN2325

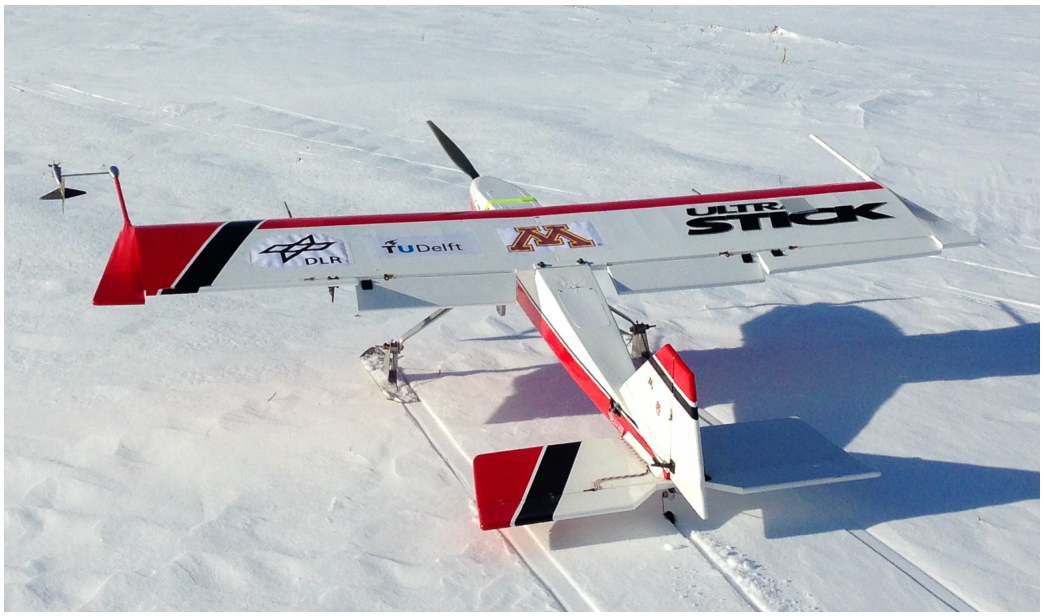

5.1(a)

5.1(b)

Figure 5.1: Ultra Stick 120 Testbed: Airframe 5.1(a), aerodynamic angle vane 5.1(b)

sideslip angle (Figure 5.1(b)). Analog potentiometers are used to measure actual control surface deflections during flight. The propeller rotational speed (measured in

RPM) is logged by the electronic speed controllers at 5 Hz. The data is synchronized and interpolated to the 50 Hz data acquisition rate of the FCS. The University of Minnesota UAV Laboratory website has the most updated information about the test platform used in the lab [66].

The main motivation behind using the Ultra Stick 120 for this flight test campaign is the availability of baseline wind tunnel measurement of the aerodynamic forces and moments [64,67]. However, since modifications and wear and tear over the years might have altered the aircraft dynamical characteristics, flight test based validation of the model was accomplished.

The goals of this experiment are twofolds. First, this experiment will validate the synthetic air data estimator using real sensor data. Secondly, it will analyze the performance and limitation of the cascaded architecture that uses a linear aircraft dynamic model in the time update process of the second filter. This last contribution is important because the linear model is simple to obtain and thus very practical to implement. To obtain the model, the aircraft is first trimmed to its nominal flight condition. Doublet excitations are added to the nominal trim flight control inputs to excite each of the aircraft's axis. Aircraft's response as recorded by the sensors are used to identify the **A** and **B** matrices of the longitudinal and lateral/directional model using the output error method described in Chapter 3. The linear model derived from these system identification flights are documented in Appendix D.

5.2 Nominal Filter Performance

The filter is initialized similarly to the simulation, that is using Equations (4.28) and (4.29), except there are six additional states in the vector $\mathbf{b}_{\text{Aero}}$ that are initialized at zero with the following covariance matrix:

$$\mathbf{P}_{\mathbf{b}_{\text{Aero}}} = \text{diag}\big[\ \big[\ 0.1(m/s)^2\ \big]^2 \quad \big[\ 0.1(m/s)^2\ \big]^2 \quad \big[\ 0.1(m/s)^2\ \big]^2 \quad \ldots \\ \big[\ 0.2^\circ/\text{sec}^2\ \big]^2 \quad \big[\ 0.2^\circ/\text{sec}^2\ \big]^2 \quad \big[\ 0.2^\circ/\text{sec}^2\ \big]^2 \quad \big] \tag{5.1}$$

The process noise values used in the filter is given by Equation (5.2). The differences in the parameters used for the simulation and flight testings are expected due to different aircraft platform and model used in these studies.

$$\begin{gathered}
\sigma_e = \sigma_a = \sigma_r = 0.8^\circ \ , \quad \sigma_f = 400 \text{ rpm} \\
\sigma_{w_N} = \sigma_{w_E} = 0.05 \text{ m/s}, \quad \tau_{w_N} = \tau_{w_E} = 50 \text{ sec} \\
\sigma_{W_D} = 0.02 \text{ m/s}, \quad \tau_{W_D} = 100 \text{ sec} \\
\sigma_{b_\phi} = \sigma_{b_\theta} = \sigma_{b_\psi} = 0.01^\circ \ , \quad \tau_{b_\phi} = \tau_{b_\theta} = \tau_{b_\psi} = 100 \text{ sec} \\
\sigma_X = \sigma_Y = \sigma_Z = 0.05 \text{ m/s}^2, \quad \tau_X = \tau_Y = \tau_Z = 50 \text{ sec} \\
\sigma_{\mathcal{L}} = \sigma_{\mathcal{M}} = \sigma_{\mathcal{N}} = 0.05^\circ/\text{sec}^2, \quad \tau_{\mathcal{L}} = \tau_{\mathcal{M}} = \tau_{\mathcal{N}} = 50 \text{ sec}
\end{gathered} \tag{5.2}$$

Figure 5.2 depicts the performance of the synthetic air data estimator that uses a linear aircraft model for its time update process. This figure is obtained by incorporating *only* the nonlinear attitude kinematics equation for the time update suggested in Chapter 3. This is necessary because the linear equations give inaccurate attitude estimates that effectively make the constraint needed by Equation (3.1) unusable. The flight data for this run is obtained from Flight 26 between 350 sec $< t <$ 550 sec. Information about this flight test including the aircraft's airspeed and attitude history is shown on Appendix E. Except for momentary excursions, the aircraft maintains bank angle less than 45° for the most part of the flight duration. Figure 5.2 shows that the errors are bounded by the 3-σ covariances estimated by the EKF.

This performance, however, does not extend to cases where the aircraft is in a sustained roll. For example, the plot shown on Figure 5.3 shows that this simple architecture falls apart during sustained turns made at 45° bank angle (highlighted). The airspeed estimate is biased, but when the airplane rolls back to level, such as in between the two sustained turns, the error trend seems to be self-correcting.

After implementing all of the modifications suggested in Chapter 3 to the flight data shown on Figure 5.3, the result shown on Figure 5.4 is obtained. Here, the performance has been significantly improved and the errors are bounded by the estimated 3-σ values. Adding $\mathbf{b}_{\text{Aero}}$ is crucial to the accuracy of the airspeed estimate. Histograms of each of V, α, and β estimates are shown next to each axes. Closer

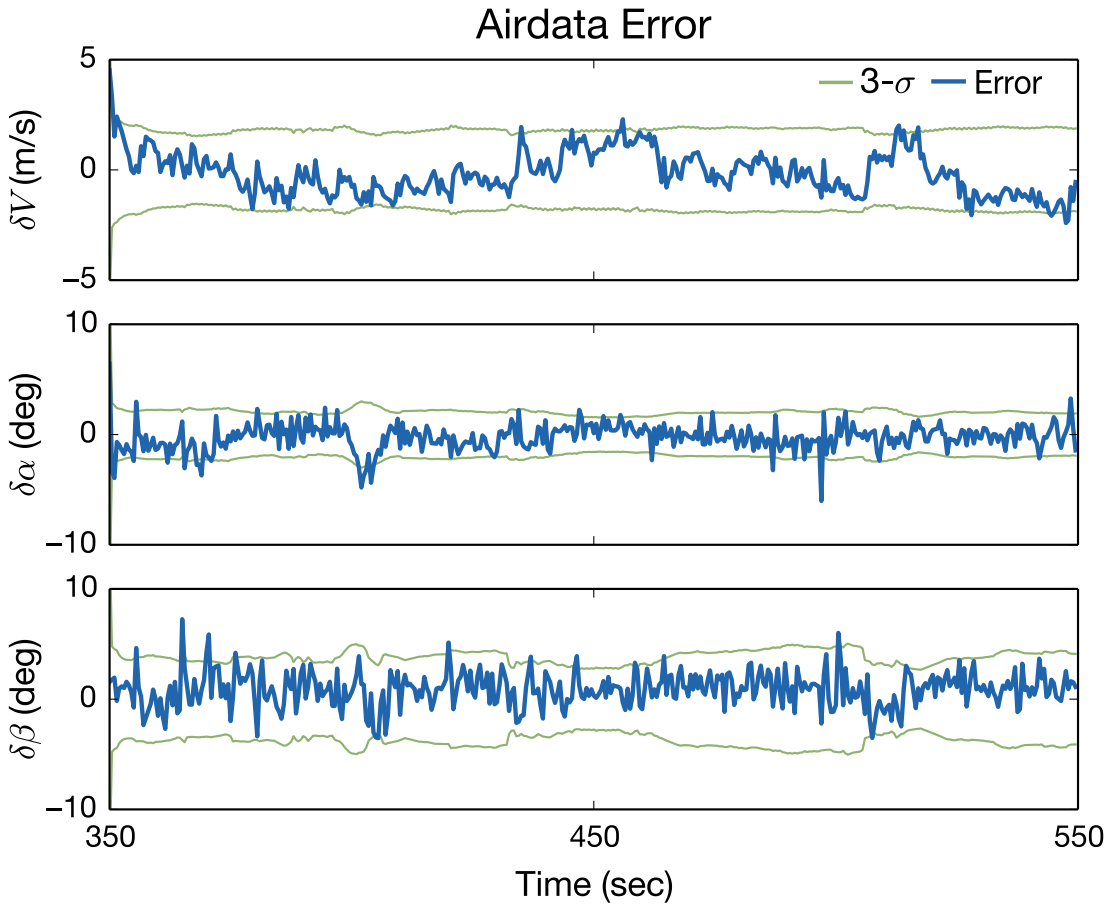

Figure 5.2: Performance of the synthetic air data estimator

examination on the histogram, however, shows that the errors have heavier tails than a Gaussian probability density function. This is not surprising because EKF only propagates up to second order statistics.

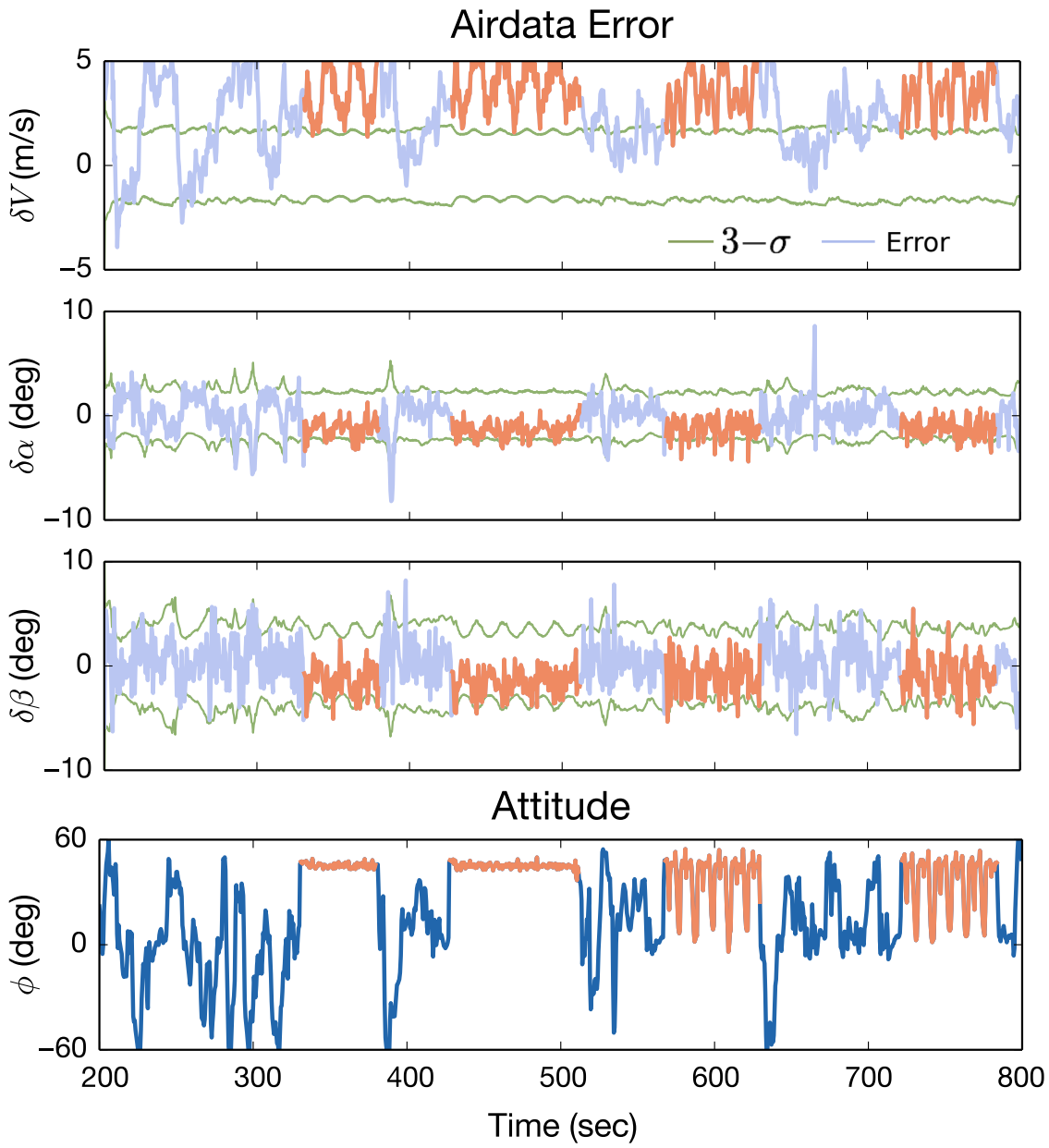

Figure 5.3: Performance of the synthetic air data estimator during steep turns. Flight description can be found on Appendix E.1

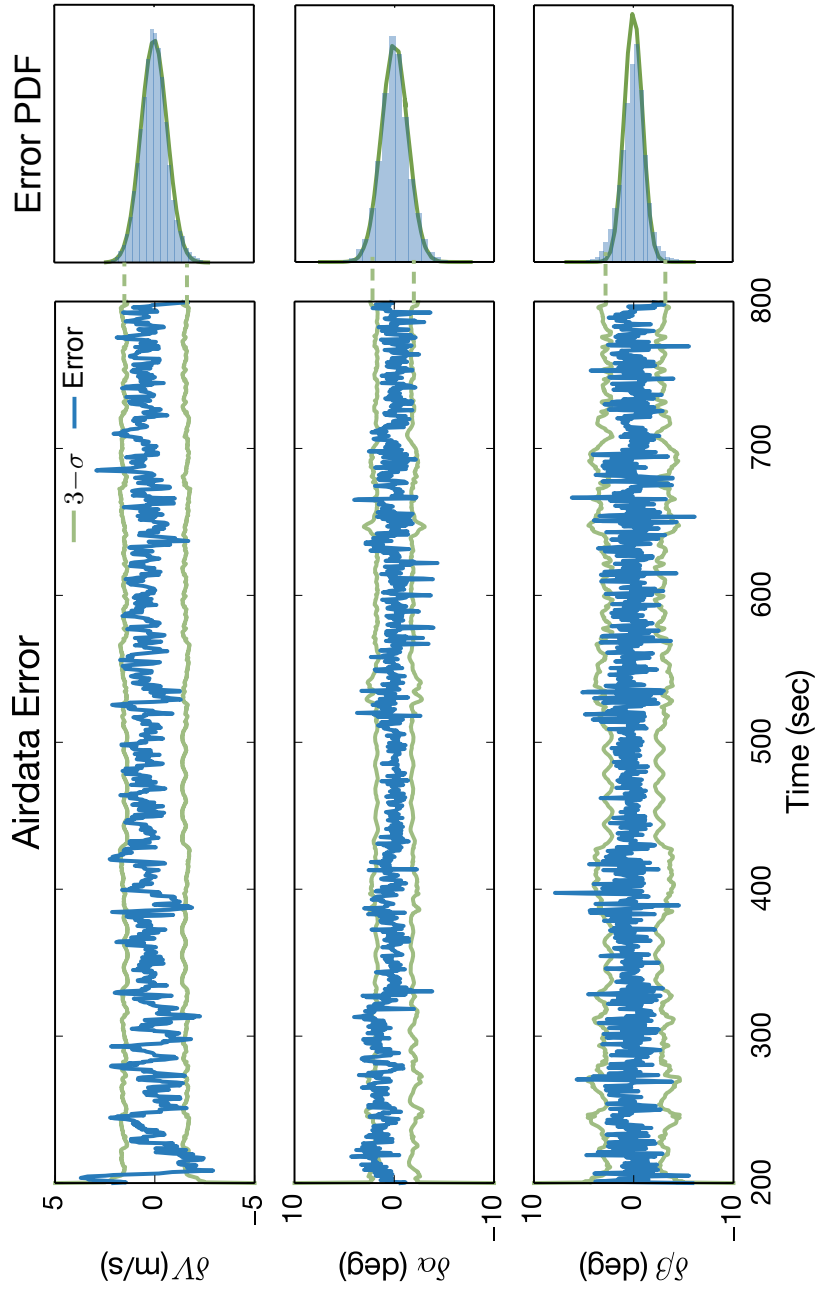

Figure 5.4: Improved filter performance during steep turns

5.3 Limitation

Although these improvements work very well to alleviate errors caused by large attitude difference from trim condition, they do not solve the errors caused by the aircraft flying at a speed that is very different from the trim airspeed at which the model was derived. The error plots on Figure 5.5 highlight this particular issue. Between 580 sec $\leq t \leq$ 670 sec, the aircraft flew a series of $\pm$ 45 $^\circ$ bank angle turns during which the airspeed went as low as 13 m/s. The trim condition for the Ultra Stick 120 used in the modeling was 21 m/s. Thus 13 m/s represents a 38% change in airspeed. The plot shows that the accuracy of sideslip angle estimate is greatly affected by this airspeed difference. Even though not as sensitive as β, the same observation can also be made to the angle of attack estimate. These observations are also found in Figure 5.2 at $t = 400$ sec. The reduction in accuracy of the angle of attack estimate can be correlated to the dip in the airspeed. Finally, a closer examination of Figure 5.4 shows that the estimates of α and β are significantly better when the aircraft flies close to the trim airspeed of 21 m/s.

Interestingly, this change in accuracy is less obvious when the airspeed changes in the other direction, i.e. when the airspeed is greater than 21 m/s. Stated differently, α and β estimates are more sensitive at low airspeed. There is a physical explanation to this behavior and it has been alluded in an article by Boeing [68] that depicted a similar plot to Figure 5.6. This following simplified argument would give insight to observation in our results.

Figure 5.6 shows a relation between V and α during a steady straight and level cruise. Since the relationship is nonlinear, the gradient of this α-V curve changes with flight conditions: It is steeper at high speed (small angle of attack) and it is shallower at low speed (high angle of attack). The steeper gradient indicates higher sensitivity of α to changes in V. In other words, small error in α translates to high error in V. Similar relationship can be derived for β.

The measurement update in the synthetic air data estimator corrects *a priori* α and β estimates by looking at the (ground) velocity innovation. Stated differently, *a priori* α and β estimates are used to obtain expected (ground) velocity measurement.

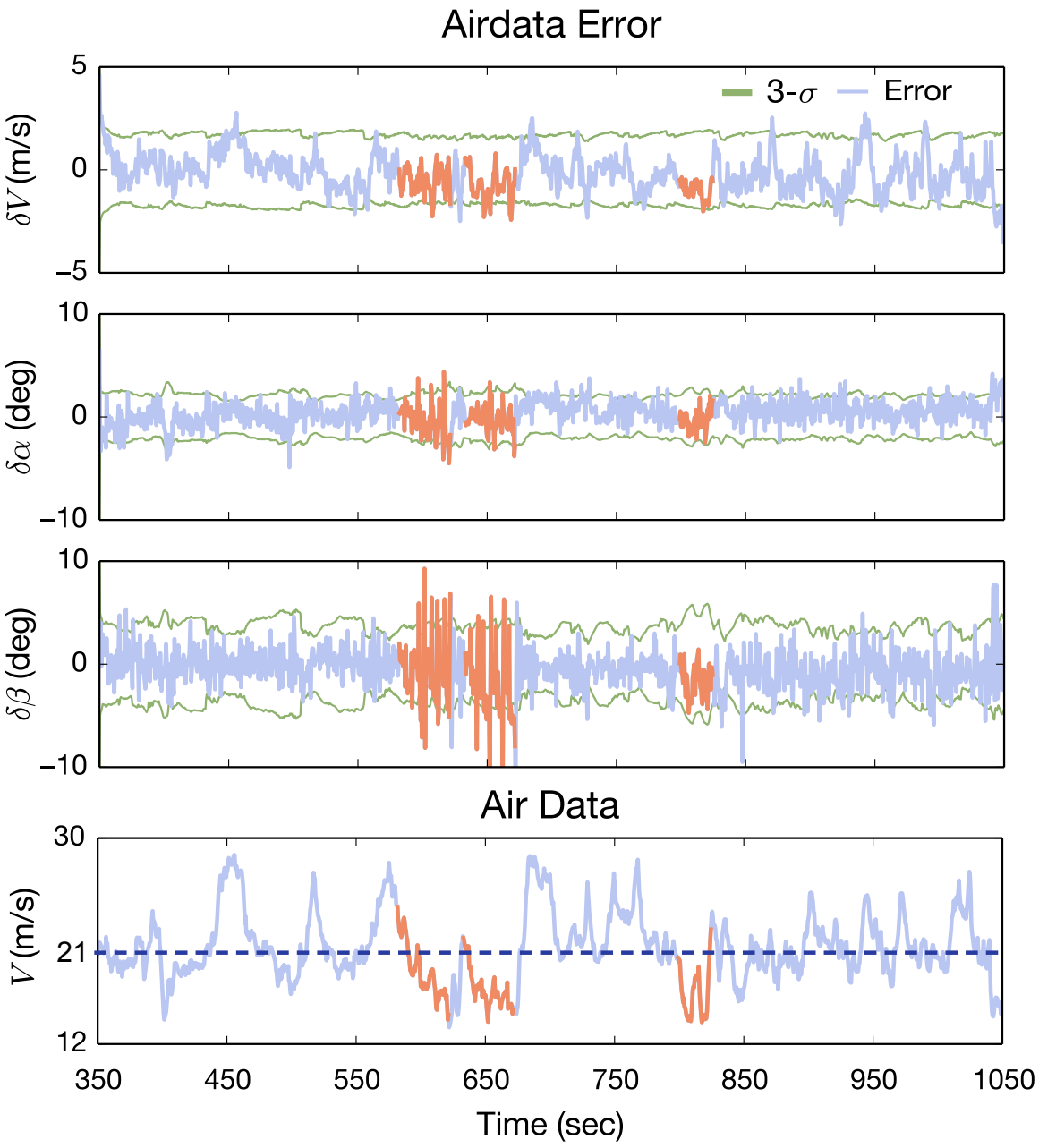

Figure 5.5: Accuracy of the air data estimate is bad at large deviation from trim airspeed (highlighted region). Flight description can be found on Appendix E.2

The difference between this expected quantity and the actual measurement is used to find the correction to the *a priori* estimates. As such, any error in the *a priori*

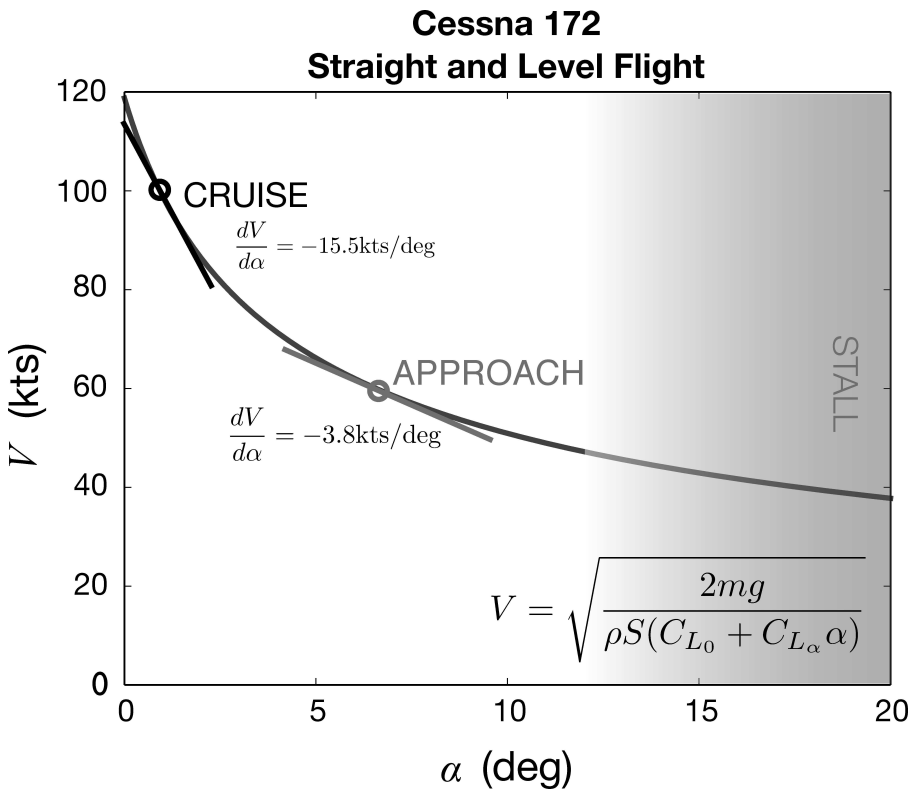

Figure 5.6: Angle of attack vs. Airspeed sensitivity

estimate must result in large enough error (in terms of signal to noise ratio) in the expected measurements so that useful corrections can be calculated. The worsening accuracy in α and β estimates at low airspeed is precisely because of the shallower gradient in this region.

Unfortunately, this low airspeed, high angle of attack region is the region at which the synthetic air data estimator is extremely important. This problem cannot be eliminated simply by using a single linear model of the aircraft because of the aerodynamic forces and moments are inherently a function of airspeed. One can solve this problem either by using the nonlinear aircraft dynamic model like shown on Chapter 4 or by scheduling the linear model based on the airspeed estimate. Model scheduling is a subject of future work.

Chapter 6

Conclusion

6.1 Conclusion

This work has presented a method for synthetic estimation of airspeed, angle of attack and sideslip. The estimator does not rely on the conventional pitot-static-vane air data systems and thus does not suffer from the same error mode as the conventional systems. On the other hand, it depends on the aircraft's equations of motion to estimate the air data triplet from groundspeed vector observations. As such, different considerations have to be taken into account when devising this estimator.

Sensor error characteristics and aircraft dynamic model uncertainty has a key role in determining the accuracy of the synthetic airspeed, angle of attack, and sideslip estimates. Particularly, they dictate the choice of filter architecture that has to be used to get an accurate estimate of the air data estimates. The analysis presented in this dissertation shows why single filter architecture is only suitable when high quality IMU is used. This is because inertial sensor biases are small and stable that they can be precalibrated and thus do not need to be part of the states that must be estimated. On the other hand, a low cost IMU requires a federated architecture to give accurate estimates of the air data triplets.

The federated filter architecture is robust to sensor error variation and aircraft dynamic model uncertainty. Separating the states of interest into two state vectors effectively adds constraints that allow estimating sensor biases accurately. Moreover, because raw acceleration measurements are not used directly, the effect of dynamic

modeling error on the air data accuracy is minimal.

The feasibility of using a linear aircraft dynamic model in the estimator is also investigated. Due to its localized accuracy, several modifications are required to avoid filter divergence caused by large deviations from the trim condition, such as during steep turns. The estimator shows good performance on both simulated flight data and real flight data. The result on the flight test data on Ultra Stick 120 shows that the air data estimates compares very well against the conventional air data sensors on board. Moreover, the filter appears to be insensitive to modeling error as shown in the good performance of the filter despite using linearized equations of motion. The 3-σ accuracy for the airspeed, angle of attack, and sideslip estimates are less than 2 m/s, 3° , and 5° , respectively. The linear model, however, is unable to handle the situation when the aircraft's speed deviates far from the trim velocity.

It is judged that the method such as presented in this paper will be indispensable in applications such as small UAVs or general aviation aircrafts where the luxury of having multiple airdata system is often unaffordable. In these instances, an approach like the one discussed in this paper can be used to provide analytical redundancy in addition to a traditional airdata system or serve as a backup to an existing traditional airdata system.

6.2 Future Work

In addition to the work presented in this dissertation, there are other aspects of the estimator that should be addressed to improve its performance and utility in modern avionics system. Here, we list three future research areas that would benefit the synthetic air data estimator.

The first area is in dynamic modeling, in particular, stochastic dynamic modeling. Any model-based estimators, such as the subject of this dissertation, require modeling of the equations of motion's output uncertainty. In this work, a simplified stochastic model that relies on input uncertainty overbounding has been proposed. A better model such as proposed by [69] for the thrust model has the potentials to improve the accuracy and reliability of the synthetic air data estimator.

Additionally, issues related to model scheduling has to be investigated. In the case of the linear model, this is a very crucial issue because the estimator has been shown to be sensitive to the airspeed at which the model is linearized about. By optimally selecting the valid model for the filter, it is possible to design a robust synthetic air data estimator that is easy to reconfigure for modeling variation.

Another important research area is with regards to the situaton that demands the use of this estimator in a closed loop configuration, i.e., with an autopilot. Although the synthetic air data system is conceived to be a standby (or a backup) system providing the much needed redundancy on size, weight, and power constrained aircraft, it is not inconceivable that it be used to control the airplane. Because the estimator uses flight control input to derive its estimate of airspeed, angle of attack, and sideslip angle; it is possible that using the synthetic estimate in closed loop may result in instability. This has not been studied in this work.

There are other aspects of this synthetic air data estimator that could be improved. The groundwork laid by this work provides a starting point that enables reliable future avionics design.

Appendix A

Simulation Model

A.1 Force and Moment Coefficient Model

Propulsion

$$C_T = C_{T_0} + C_{T_1} J + C_{T_2} J^2 + C_{T_3} J^3$$
$$C_P = C_{P_0} + C_{P_1} J + C_{P_2} J^2 + C_{P_3} J^3 + \cdots + C_{P_9} J^9$$

Aerodynamic Forces

$$C_D = C_{D_0} + C_{D_\beta} |\beta| + C_{D_\alpha} \alpha + C_{D_{\alpha^2}} \alpha^2 + C_{D_{\delta_e}} \delta_e$$
$$C_Y = C_{Y_\beta} \beta + C_{Y_p} \frac{pb}{2V} + C_{Y_r} \frac{rb}{2V} + C_{Y_{\delta_r}} \delta_r$$
$$C_L = C_{L_0} + C_{L_\alpha} \alpha + C_{L_q} \frac{q\bar{c}}{2V} + C_{L_{\dot{\alpha}}} \frac{\dot{\alpha}\bar{c}}{2V} + C_{L_{\delta_e}} \delta_e$$

Aerodynamic Moments

$$C_l = C_{l_\beta} \beta + C_{l_p} \frac{pb}{2V} + C_{l_r} \frac{rb}{2V} + C_{l_{\delta_r}} \delta_r + C_{l_{\delta_a}} \delta_a$$
$$C_m = C_{m_0} + C_{m_\alpha} \alpha + C_{m_q} \frac{q\bar{c}}{2V} + C_{m_{\dot{\alpha}}} \dot{\alpha} + C_{m_{\delta_e}} \delta_e$$
$$C_n = C_{n_\beta} \beta + C_{n_p} \frac{pb}{2V} + C_{n_r} \frac{rb}{2V} + C_{n_{\delta_r}} \delta_r + C_{n_{\delta_a}} \delta_a$$

A.2 Cessna 172 Properties

C_{T_0}	0.0677	C_{D_0}	0.0356	C_{l_β}	-0.0923
C_{T_1}	0.0048	C_{D_α}	0.2543	C_{l_p}	-0.4840
C_{T_2}	-0.0204	$C_{D_{\alpha^2}}$	1.7283	C_{l_r}	0.1869
C_{T_3}	-0.0342	C_{D_β}	0.1700	$C_{l_{\delta_r}}$	0.0147
C_{P_0}	0.0571	$C_{D_{\delta_e}}$	0.0000	$C_{l_{\delta_a}}$	0.2290
C_{P_1}	0.2080	C_{Y_β}	-0.3926	C_{m_0}	0.1000
C_{P_2}	-1.8704	C_{Y_p}	-0.1450	C_{m_α}	-1.8000
C_{P_3}	6.3336	C_{Y_r}	0.2670	C_{m_q}	-12.4000
C_{P_4}	-11.1477	$C_{Y_{\delta_r}}$	0.1870	$C_{m_{\delta_e}}$	-1.1220
C_{P_5}	10.9467	C_{L_0}	0.2685	C_{n_β}	0.0587
C_{P_6}	-6.1841	C_{L_α}	5.0411	C_{n_p}	-0.0278
C_{P_7}	1.9859	$C_{L_{\dot{\alpha}}}$	0.0000	C_{n_r}	-0.0937
C_{P_8}	-0.3339	C_{L_q}	3.9000	$C_{n_{\delta_r}}$	-0.0430
C_{P_9}	0.0225	$C_{L_{\delta_e}}$	0.4300	$C_{n_{\delta_a}}$	-0.0053

Table A.1: Simulated Cessna 172 Aerodynamic Parameters

Mass, m	[kg]	881.4598
Wing Span, b	[m]	10.9118
Wing Area, S	[m^2]	16.1651
Mean Aerodynamic Chord, $\bar{c}$	[m]	1.4935
Moment of Inertia, I_{xx}	[kg.m^2]	1285.3154
Moment of Inertia, I_{yy}	[kg.m^2]	1824.9310
Moment of Inertia, I_{zz}	[kg.m^2]	2666.8939
Propeller Coordinate, r_x	[m]	0.9576
Propeller Coordinate, r_y	[m]	0.0000
Propeller Coordinate, r_z	[m]	-0.6756

Table A.2: Physical and Geometric Properties of Simulated Cessna 172

Appendix B

Nonlinear Dynamics Covariance Propagation Model

B.1 Jacobian matrix

If the EOM's error state vector is defined as:

$$\begin{aligned}\mathbf{x}_{\text{ac}} &= \begin{bmatrix} \delta\mathbf{V}_{WB}^{B} \\ \delta\boldsymbol{\omega}^{B} \\ \delta\boldsymbol{\Psi} \end{bmatrix} \\ &= \begin{bmatrix} \mathbf{V}_{WB}^{B} - \hat{\mathbf{V}}_{WB}^{B} \\ \boldsymbol{\omega} - \hat{\boldsymbol{\omega}} \\ \hat{\mathbf{C}}_{B}^{N}\mathbf{C}_{N}^{B} - \mathbf{I}_{3} \end{bmatrix}\end{aligned} \tag{B.1}$$

then, the state Jacobian matrix is given by:

$$\boldsymbol{\Phi}_{\text{ac}} = \frac{\partial \boldsymbol{\mathcal{F}}}{\partial \mathbf{x}_{\text{ac}}} = \exp\left(\mathbf{F}_{\text{ac}} \cdot T_s\right) \tag{B.2}$$

where the matrix $\mathbf{F}_{\text{ac}}$ is defined as:

$$\mathbf{F}_{\text{ac}} = \begin{bmatrix} \mathbf{F}_{11} & \mathbf{F}_{12} & \mathbf{F}_{13} \\ \mathbf{F}_{21} & \mathbf{F}_{22} & \mathbf{0}_{3\times3} \\ \mathbf{0}_{3\times3} & \mathbf{F}_{32} & \mathbf{0}_{3\times3} \end{bmatrix} \tag{B.3}$$

The block matrices inside $\mathbf{F}_{\text{ac}}$ are given by the followings:

$$\mathbf{F}_{11} = \frac{1}{m}\begin{bmatrix} \frac{\partial X}{\partial u} & \frac{\partial X}{\partial v} & \frac{\partial X}{\partial w} \\ \frac{\partial Y}{\partial u} & \frac{\partial Y}{\partial v} & 0 \\ \frac{\partial Z}{\partial u} & 0 & \frac{\partial Z}{\partial w} \end{bmatrix} \tag{B.4}$$

$$\mathbf{F}_{12} = \frac{1}{m}\begin{bmatrix} 0 & 0 & 0 \\ \frac{\partial Y}{\partial p} & 0 & \frac{\partial Y}{\partial r} \\ 0 & \frac{\partial Z}{\partial q} & 0 \end{bmatrix} \tag{B.5}$$

$$\mathbf{F}_{13} = \mathbf{C}_N^B\,[\mathbf{g}\times] = \mathbf{C}_N^B \cdot \begin{bmatrix} 0 & -9.81 & 0 \\ 9.81 & 0 & 0 \\ 0 & 0 & 0 \end{bmatrix} \tag{B.6}$$

$$\mathbf{F}_{21} = \begin{bmatrix} I_{xx} & 0 & I_{xz} \\ 0 & I_{yy} & 0 \\ I_{xz} & 0 & I_{yy} \end{bmatrix}^{-1} \begin{bmatrix} \frac{\partial \mathcal{L}}{\partial u} & \frac{\partial \mathcal{L}}{\partial v} & 0 \\ \frac{\partial \mathcal{M}}{\partial u} & 0 & \frac{\partial \mathcal{M}}{\partial w} \\ \frac{\partial \mathcal{N}}{\partial u} & \frac{\partial \mathcal{N}}{\partial v} & 0 \end{bmatrix}$$

$$\mathbf{F}_{22} = \begin{bmatrix} I_{xx} & 0 & I_{xz} \\ 0 & I_{yy} & 0 \\ I_{xz} & 0 & I_{yy} \end{bmatrix}^{-1} \begin{bmatrix} \frac{\partial \mathcal{L}}{\partial p} & 0 & \frac{\partial \mathcal{L}}{\partial r} \\ 0 & \frac{\partial \mathcal{M}}{\partial q} & 0 \\ \frac{\partial \mathcal{N}}{\partial p} & 0 & \frac{\partial \mathcal{N}}{\partial r} \end{bmatrix} \tag{B.7}$$

$$\mathbf{F}_{32} = -\mathbf{C}_B^N = -\left(\mathbf{C}_N^B\right)^T \tag{B.8}$$

The direction cosine matrix $\mathbf{C}_N^B$ is the 3-2-1 rotation matrix from the NED frame to the body frame. In terms of the Euler angles $\mathbf{\Psi} = [\ \phi\ \ \theta\ \ \psi\ ]^T$, it is written as:

$$\mathbf{C}_N^B = \begin{bmatrix} 1 & 0 & 0 \\ 0 & \cos\phi & \sin\phi \\ 0 & -\sin\phi & \cos\phi \end{bmatrix} \begin{bmatrix} \cos\theta & 0 & -\sin\theta \\ 0 & 1 & 0 \\ \sin\theta & 0 & \cos\theta \end{bmatrix} \begin{bmatrix} \cos\psi & \sin\psi & 0 \\ -\sin\psi & \cos\psi & 0 \\ 0 & 0 & 1 \end{bmatrix} \tag{B.9}$$

B.2 Noise Shaping matrix

If the aircraft control input vector is defined as:

$$\boldsymbol{\mathcal{U}} = \begin{bmatrix} \delta_e \\ \delta_a \\ \delta_r \\ f \end{bmatrix} \tag{B.10}$$

the noise shaping matrix is given by:

$$\begin{aligned} \mathbf{G}_{\text{ac}} &= \frac{\partial \boldsymbol{F}}{\partial \boldsymbol{\mathcal{U}}} \\ &\approx \begin{bmatrix} 0 & 0 & 0 & \frac{1}{m}\frac{\partial X}{\partial \delta_f} \\ 0 & 0 & \frac{1}{m}\frac{\partial Y}{\partial \delta_r} & 0 \\ \frac{1}{m}\frac{\partial Z}{\partial \delta_e} & 0 & 0 & 0 \\ 0 & \frac{1}{I_{xx}}\frac{\partial \mathcal{L}}{\partial \delta_a} & \frac{1}{I_{xx}}\frac{\partial \mathcal{L}}{\partial \delta_r} & 0 \\ \frac{1}{I_{yy}}\frac{\partial \mathcal{M}}{\partial \delta_e} & 0 & 0 & 0 \\ 0 & \frac{1}{I_{zz}}\frac{\partial \mathcal{N}}{\partial \delta_a} & \frac{1}{I_{zz}}\frac{\partial \mathcal{N}}{\partial \delta_r} & 0 \end{bmatrix} \end{aligned} \tag{B.11}$$

B.3 Aerodynamic derivatives

$$
\begin{aligned}
\frac{\partial X}{\partial u} &= \frac{3C_{T_3}\rho u^2 d}{f} + 2C_{T_2}\rho u d^2 + \cdots \\
&\quad + \rho C_{T_0} f d^3 - \rho u S C_D + \cdots \\
&\quad + \frac{1}{2}\rho w S C_{D_\alpha} \\
\frac{\partial X}{\partial v} &= \frac{1}{2}\rho u S C_{D_\beta}\mathrm{sgn}(v) \\
\frac{\partial X}{\partial w} &= \frac{1}{2}u S C_{D_\alpha} + \rho w S C_{D_{\alpha^2}} \\
\frac{\partial X}{\partial f} &= \rho u C_{T_1} d^3 \\
\frac{\partial Y}{\partial u} &= \rho u S C_Y - \frac{1}{2}\rho v S C_{Y_\beta} + \cdots \\
&\quad - \frac{1}{2}\rho S C_{Y_p}\frac{bp}{2} - \frac{1}{2}\rho S C_{Y_r}\frac{br}{2} \\
\frac{\partial Y}{\partial v} &= \frac{1}{2}\rho u S C_{Y_\beta} \\
\frac{\partial Y}{\partial p} &= \frac{1}{2}\rho u^2 S C_{Y_p}\left(\frac{b}{2u}\right) \\
\frac{\partial Y}{\partial r} &= \frac{1}{2}\rho u^2 S C_{Y_r}\left(\frac{b}{2u}\right) \\
\frac{\partial Y}{\partial \delta_r} &= \frac{1}{2}\rho u^2 S C_{Y_{\delta_r}} \\
\frac{\partial Z}{\partial u} &= -\rho u S C_L + \frac{1}{2}\rho w S C_{L_\alpha} \\
\frac{\partial Z}{\partial w} &= -\frac{1}{2}\rho u S C_{L_\alpha} - \rho w S C_{L_{\alpha^2}} \\
\frac{\partial Z}{\partial q} &= -\frac{1}{2}\rho u^2 S C_{L_q}\left(\frac{\bar{c}}{2u}\right) \\
\frac{\partial Z}{\partial \delta_e} &= -\frac{1}{2}\rho u^2 S C_{L_{\delta_e}}
\end{aligned}
$$

$$
\begin{aligned}
\frac{\partial \mathcal{L}}{\partial u} &= \rho u S b C_l \\
\frac{\partial \mathcal{L}}{\partial v} &= \frac{1}{2}\rho u S b C_{l_\beta} \\
\frac{\partial \mathcal{L}}{\partial p} &= \frac{1}{2}\rho u^2 S b C_{l_p}\left(\frac{b}{2u}\right) \\
\frac{\partial \mathcal{L}}{\partial r} &= \frac{1}{2}\rho u^2 S b C_{l_r}\left(\frac{b}{2u}\right) \\
\frac{\partial \mathcal{L}}{\partial \delta_a} &= \frac{1}{2}\rho u^2 S b C_{n_r}\left(\frac{b}{2u}\right) \\
\frac{\partial \mathcal{L}}{\partial \delta_r} &= \frac{1}{2}\rho u^2 S b C_{n_r}\left(\frac{b}{2u}\right) \\
\frac{\partial \mathcal{M}}{\partial u} &= \rho u S \bar{c} C_m \\
\frac{\partial \mathcal{M}}{\partial w} &= \frac{1}{2}\rho u S \bar{c} C_{m_\beta} \\
\frac{\partial \mathcal{M}}{\partial q} &= \frac{1}{2}\rho u^2 S \bar{c} C_{m_q}\left(\frac{\bar{c}}{2u}\right) \\
\frac{\partial \mathcal{M}}{\partial \delta_e} &= \frac{1}{2}\rho u^2 S \bar{c} C_{m_{\delta_e}}\left(\frac{\bar{c}}{2u}\right) \\
\frac{\partial \mathcal{N}}{\partial u} &= \rho u S b C_n \\
\frac{\partial \mathcal{N}}{\partial v} &= \frac{1}{2}\rho u S b C_{n_\beta} \\
\frac{\partial \mathcal{N}}{\partial p} &= \frac{1}{2}\rho u^2 S b C_{n_p}\left(\frac{b}{2u}\right) \\
\frac{\partial \mathcal{N}}{\partial r} &= \frac{1}{2}\rho u^2 S b C_{n_r}\left(\frac{b}{2u}\right) \\
\frac{\partial \mathcal{N}}{\partial \delta_a} &= \frac{1}{2}\rho u^2 S b C_{n_r}\left(\frac{b}{2u}\right) \\
\frac{\partial \mathcal{N}}{\partial \delta_r} &= \frac{1}{2}\rho u^2 S b C_{n_r}\left(\frac{b}{2u}\right)
\end{aligned}
$$

Appendix C

Linear Dynamics Covariance Propagation Model

C.1 Jacobian matrix

The entries of $\mathbf{\Phi}_{\text{ac}}$ for the linear aircraft dynamic model is given as follows.

$$\mathbf{\Phi}_{\text{ac}} = \exp\left(\mathbf{F}_{\text{ac}} \cdot T_s\right) \tag{C.1}$$

where the matrix $\mathbf{F}_{\text{ac}}$ is defined as:

$$\mathbf{F}_{\text{ac}} = \begin{bmatrix} \mathbf{F}_{11} & \mathbf{F}_{12} & \mathbf{F}_{13} & \mathbf{0}_{3\times3} \\ \mathbf{F}_{21} & \mathbf{F}_{22} & \mathbf{0}_{3\times3} & \mathbf{0}_{3\times3} \\ \mathbf{0}_{3\times3} & \mathbf{F}_{32} & \mathbf{0}_{3\times3} & \mathbf{0}_{3\times3} \\ \mathbf{0}_{3\times3} & \mathbf{0}_{3\times3} & \mathbf{0}_{3\times3} & \mathbf{\Phi}_b \end{bmatrix} \tag{C.2}$$

The block matrices inside $\mathbf{F}_{\text{ac}}$ are given by the followings:

$$\mathbf{F}_{11} = \begin{bmatrix} X_u & 0 & X_w \\ 0 & Y_v & 0 \\ Z_u & 0 & Z_w \end{bmatrix} \tag{C.3}$$

$$\mathbf{F}_{12} = \begin{bmatrix} 0 & X_q & 0 \\ Y_p & 0 & Y_r \\ 0 & Z_q & 0 \end{bmatrix} \tag{C.4}$$

$$\mathbf{F}_{13} = \mathbf{C}_N^B \left[\mathbf{g}\times\right] = \mathbf{C}_N^B \cdot \begin{bmatrix} 0 & -9.81 & 0 \\ 9.81 & 0 & 0 \\ 0 & 0 & 0 \end{bmatrix} \tag{C.5}$$

$$\mathbf{F}_{21} = \begin{bmatrix} 0 & \mathcal{L}_v & 0 \\ \mathcal{M}_u & 0 & \mathcal{M}_w \\ 0 & \mathcal{N}_v & 0 \end{bmatrix}$$

$$\mathbf{F}_{22} = \begin{bmatrix} \mathcal{L}_p & 0 & \mathcal{L}_r \\ 0 & \mathcal{M}_q & 0 \\ \mathcal{N}_p & 0 & \mathcal{N}_r \end{bmatrix} \tag{C.6}$$

$$\mathbf{F}_{32} = -\mathbf{C}_B^N = -\left(\mathbf{C}_N^B\right)^T \tag{C.7}$$

C.2 Noise Shaping matrix

If the aircraft control input vector is defined as:

$$\boldsymbol{\mathcal{U}} = \begin{bmatrix} \delta_e \\ \delta_a \\ \delta_r \\ f \end{bmatrix} \tag{C.8}$$

the noise shaping matrix is given by:

$$\mathbf{G}_{\text{ac}} = \begin{bmatrix} X_{\delta_e} & 0 & 0 & \frac{1}{m}\frac{\partial T}{\partial f} \\ 0 & Y_{\delta_a} & Y_{\delta_r} & 0 \\ Z_{\delta_e} & 0 & 0 & 0 \\ 0 & \mathcal{L}_{\delta_a} & \mathcal{L}_{\delta_r} & \frac{1}{I_x}\frac{\partial \mathcal{T}}{\partial f} \\ \mathcal{M}_{\delta_e} & 0 & 0 & 0 \\ 0 & \mathcal{N}_{\delta_a} & \mathcal{N}_{\delta_r} & 0 \end{bmatrix} \tag{C.9}$$

Appendix D

Ultra Stick 120 Model

D.1 Aircraft's Geometry

Mass, m	[kg]	8.338
Wing Span and Area, b, S	[m], [m^2]	1.9172, 0.7692
Mean Aerodynamic Chord, $\bar{c}$	[m]	0.4336
Moment of Inertia, I_{xx}	[kg.m^2]	0.8568
Moment of Inertia, I_{yy}	[kg.m^2]	1.0095
Moment of Inertia, I_{zz}	[kg.m^2]	1.7005

Table D.1: Physical and Geometric Properties of Ultrastick 120

D.2 Propeller Model

Type		APC 18×12
Diameter, d	[inch]	18

Thrust coefficient:

$$C_T = -0.0696J + 0.1364 \tag{D.1}$$

Power coefficient:

$$C_P = -0.0441J + 0.0861 \tag{D.2}$$

D.3 Trim Condition

$$\bar{V} = 19.20 \text{ m/s}, \qquad \bar{\alpha} = 4.47^\circ\ , \qquad \bar{\beta} = -1.01^\circ$$

$$\bar{p} = \bar{q} = \bar{r} = 0$$

$$\bar{\phi} = -1.35^\circ\ , \qquad \bar{\theta} = 5.47^\circ$$

$$\bar{\delta}_e = -4.37^\circ\ , \qquad \bar{\delta}_a = -3.48^\circ\ , \qquad \bar{\delta}_r = -0.10^\circ$$

$$\bar{f} = 1974.15 \text{ RPM}$$

D.4 Stability Derivatives

X_u	-0.437	M_u	-0.112	L_v	-1.221
X_w	-0.621	M_w	-2.008	L_p	-7.730
X_q	6.777	M_q	-3.535	L_r	0.190
X_θ	–9.765	M_{δ_e}	-37.329	L_{δ_a}	-68.917
X_{δ_e}	13.444	Y_v	-0.644	L_{δ_r}	-1.922
Z_u	-0.605	Y_p	1.660	N_v	0.375
Z_w	-4.236	Y_r	-19.180	N_p	-0.370
Z_q	18.149	Y_ϕ	9.770	N_r	-1.660
Z_θ	-0.940	Y_{δ_a}	-2.082	N_{δ_a}	0.620
Z_{δ_e}	1.077	Y_{δ_r}	2.238	N_{δ_r}	-12.988

Table D.2: Identified Stability Derivatives

Appendix E

Flight Test Results

E.1 Ibis Flight 18

Flight 18 was conducted on December 12, 2013 at UMore Park, Rosemount, MN. The flight data can be downloaded from [70]. The flight trajectory is shown on Figure E.1 and the corresponding air data and attitude history are shown on Figures E.2 and E.3, respectively. The highlighted regions in the figures show the duration at which the airplane was sustaining a roll angle of 45° while maintaining airspeed of 21 m/s (trim).

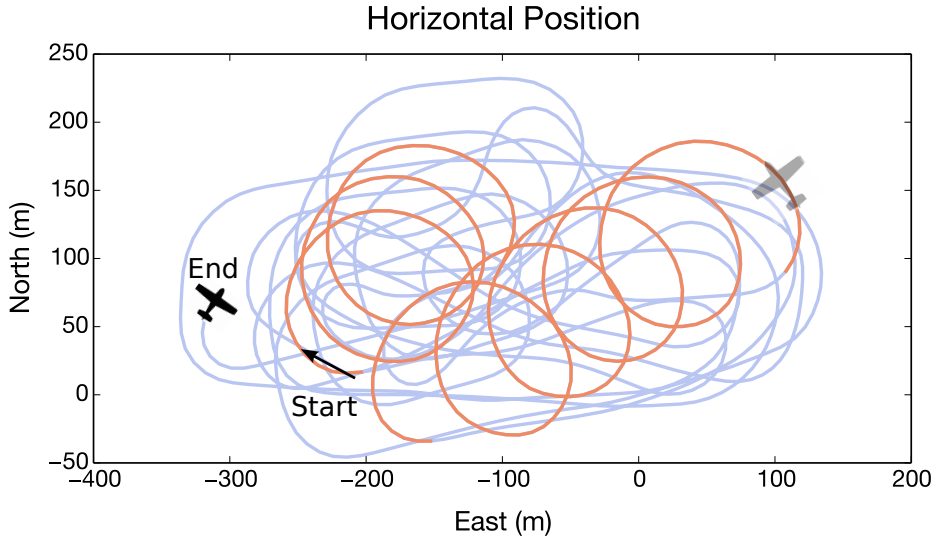

Figure E.1: Flight 18 North-East plane trajectory

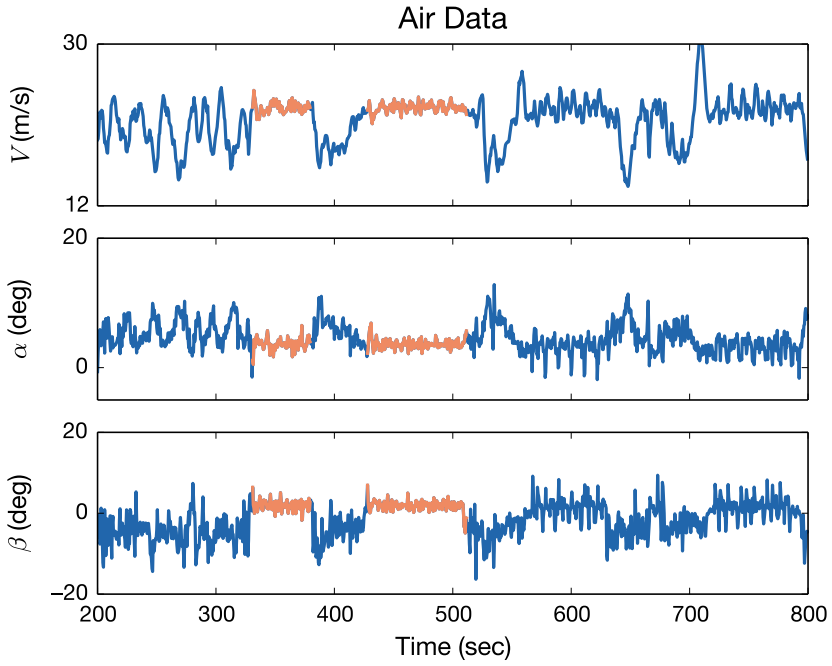

Figure E.2: Flight 18 airspeed, angle of attack, and sideslip history

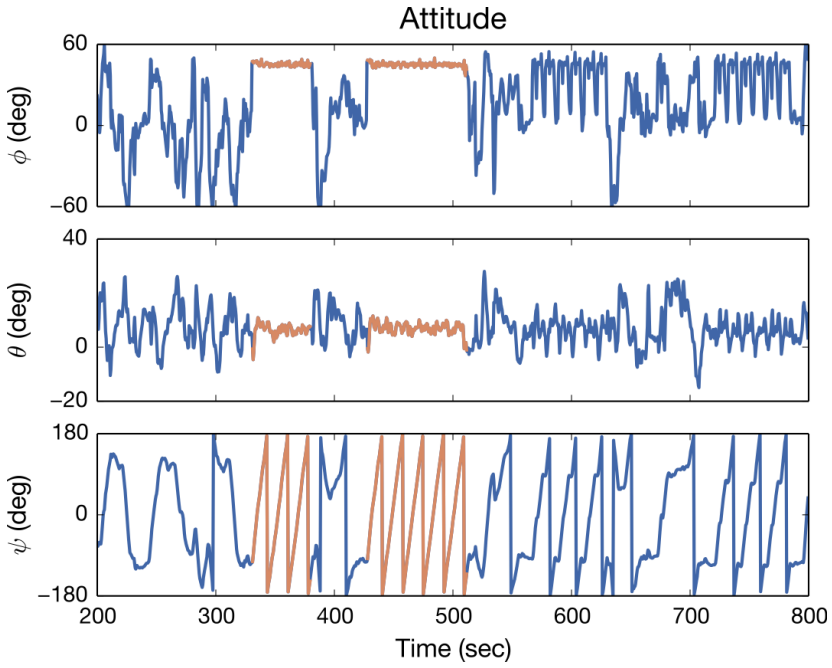

Figure E.3: Flight 18 roll, pitch, and yaw history

The goal of this flight test was to conduct the synthetic air data estimator's performance in flight conditions that are far away from trim condition. In this case, the effect of off-trim attitude was investigated while maintaing trim airspeed. After incorporating the modifications recommended in Chapter 3 to the linear aircraft dynamic model, the accuracy of the estimates is significantly improved and the estimation errors of V, α, and β are shown on Figure 5.4. When those modifications are not implemented, the estimation error is shown on Figure 5.3.

E.2 Ibis Flight 26

Flight 26 was conducted on April 5, 2014 at UMore Park, Rosemount, MN. The flight data can be downloaded from [70]. The flight trajectory is shown on Figure E.4 and the corresponding air data and attitude history are shown on Figures E.5 and E.6, respectively. The highlighted regions in the figures indicate the duration at which the airspeed was allowed to deviate from the trim condition (cf. Figure 5.5).

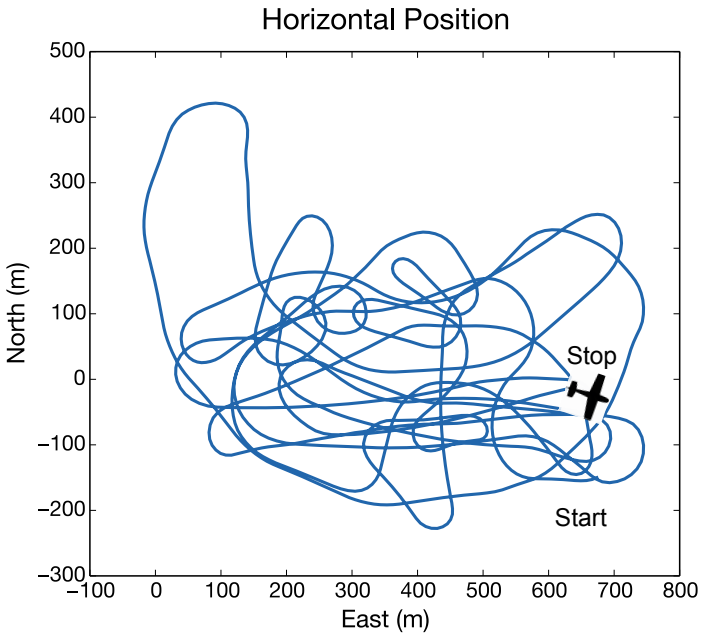

Figure E.4: Flight 26 North-East plane trajectory

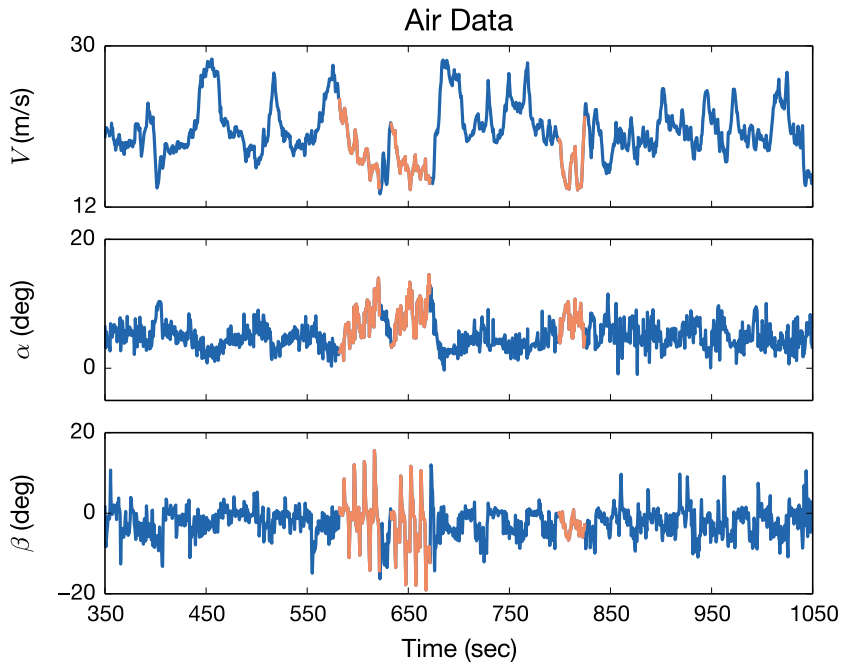

Figure E.5: Flight 18 airspeed, angle of attack, and sideslip history

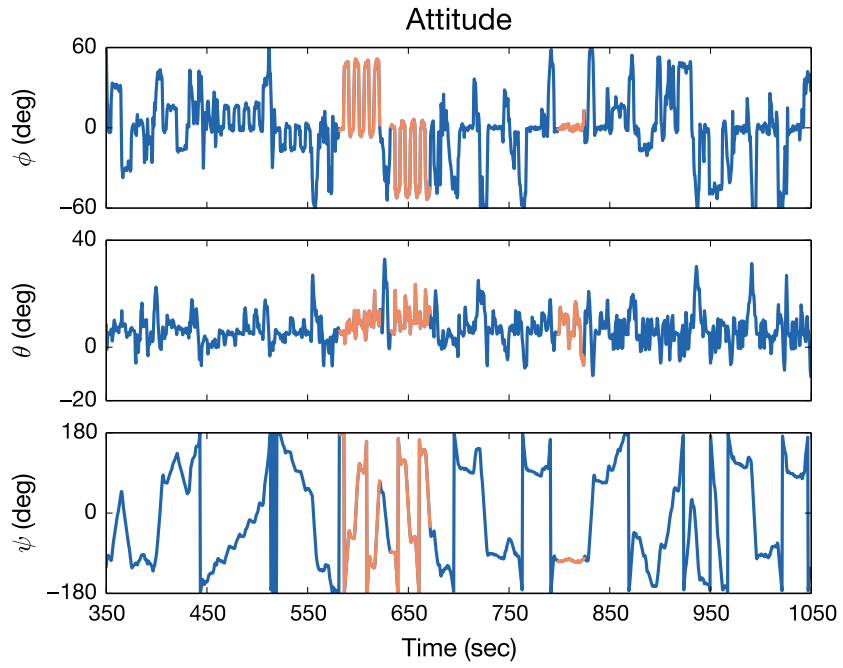

Figure E.6: Flight 18 roll, pitch, and yaw history

E.2. Ibis Flight 26

Between 550 se $< t <$ 700 sec, the aircraft is banked at 45° roll angle during which the airplane slows down to at least 13 m/s. In the second maneuver happening between 750 sec $< t <$ 800 sec, the aircraft is slowed down by cutting off the throttle while maintaining straight and level flight. During this maneuver, the airspeed also decays to about 13 m/s. The goal of this experiment is to examine the robustness of the linear model to airspeed deviation. Running the synthetic air data estimator using the linear model described in Appendix D results in errors shown in Figure 5.5.

Bibliography

[1] –, *A330 Flight Crew Operations Manual*, Airbus.

[2] Verbeek, M. J. and Jentink, H. W., "Optical Air Data System Flight Testing," NLR TP-2012-068, February 2012.

[3] Heller, M., Myschik, S., Holzapfel, F., and Sachs, G., "Low-cost approach based on navigation data for determining angles of attack and sideslip for small aircraft," *Proceedings of AIAA Guidance, Navigation, and Control Conference and Exhibit*, Austin, TX, August 2003, AIAA2003-5777.

[4] Myschik, S., Holzapfel, F., and Sachs, G., "Low-cost sensor based integrated airdata and navigation system for general aviation aircraft," *Proceedings of AIAA Guidance, Navigation, and Control Conference and Exhibit*, August 2008.

[5] Koifman, M. and Bar-Itzhack, I. Y., "Inertial Navigation System Aided by Aircraft Dynamics," *IEEE Transactions on Control Systems Technology*, Vol. 7, No. 4, July 1999, pp. 487–493.

[6] Bryson, M. and Sukkarieh, S., "Vehicle model aided inertial navigation for a UAV using low-cost sensors," *Proceedings of Australasian Conference on Robotics and Automation*, Canberra, Australia, 2004.

[7] SAE, "Air Data Computer - Minimum Performance Standard," September 1996.

[8] Seidel, G. A., Cronin, D. J., Mette, J. H., Koosmann, M. R., Schmitz, J. A., Fedele, J. R., and Kromer, D. A., "Multi-function Air Data Sensing Probe Having an Angle of Attack Vane," U.S Patent No: 6,941,805 B2, September 13, 2015.

[9] Treaster, A. L. and Yocum, A. M., "The Calibration and Application of Five-Hole Probes," NAVSEA TM 78-10, July 1978.

[10] –, "Alpha Systems AOA," URL: http://www.alphasystemsaoa.com/, Last accessed: June 16, 2014.

[11] –, "Dynon Angle of Attack/Pitot," URL: http://www.dynonavionics.com/docs/D180_Feature_AOA.html, Last accessed: June 16, 2014.

[12] –, "Garmin AOA System," URL: https://buy.garmin.com/en-US/US/in-the-air/avionics-safety/indicators/aoa-system/prod149850.html, Last accessed: June 16, 2014.

[13] –, "Press Release on ICON A5's Angle of Attack System," URL: http://www.iconaircraft.com/dl/news/pdf/20130722_ICON_Aircraft_A5_Angle_of_Attack_System.pdf, Last accessed: July 23, 2014.

[14] –, "Pilot's Handbook of Aeronautical Knowledge," FAA-H-8083-25A, 2008.

[15] Sizoo, D., "More than Just a Display: Real World Uses for Angle of Attack," *FAA Safety Briefing*, May/June 2014, pp. 25–26.

[16] Hempe, D. W. and Seipel, J. D., "Approval of Non-Required Angle of Attack (AoA) Indicator Systems Approval of Non-Required Angle of Attack (AoA) Indicator Systems," Memorandum No. AIR 100-14-110-PM01, Federal Aviation Administration, February 5, 2014.

[17] Wheeler, T. J., Seiler, P., Packard, A. K., and Balas, G. J., "Performance Analysis of Fault Detection System Based on Analytically Redundant Linear Time-Invariant Dynamics," *Proceedings of American Control Conference (ACC)*, San Francisco, CA, June 2011, pp. 214–249.

[18] BEA, "Final Report on the Accident on 1st June 2009 to the Airbus A330-203 registered F-GZCP operated by Air France Flight 447 Rio de Janeiro-Paris," July 2012.

[19] Duvivier, E., "High Altitude Icing Environment," *Proceedings of International Air Safety and Climate Change Conference*, EASA, September 2010.

[20] Schechter, E., "Detecting Pitot tube obstructions," *Aerospace America*, May 2014, pp. 16–18.

[21] Matayoshi, N., Inokuchi, H., Yazawa, K., and Okuno, Y., "Development of an Airborne Ultrasonic Velocimeter and its Application to Helicopters," *Proceedings of AIAA Atmospheric Flight Mechanics Conference*, San Francisco, CA, 2005, AIAA2005-6118.

[22] Rahm, S., "Precusor Experiment for an Active True Airspeed Sensor," *Optics Letters*, Vol. 26, No. 6, March 2001, pp. 319–321.

[23] McGann, R. L., "Flight Test Results from a Low-power Doppler Optical Air Data Sensor," *Proceedings of SPIE 2464, Air Traffic Control Technologies*, Vol. 116, 1995, doi: 10.1117/12.211483.

[24] Matayoshi, N., Asaka, K., and Okuno, Y., "Flight-Test Evaluation of A Helicopter Airborne Lidar," *AIAA Journal of Aircraft*, Vol. 44, No. 5, September-October 2007, pp. 1712–1720.

[25] Krishna, Y., O'Byrne, S., Wittig, S., and Kurtz, J. J., "Numerically Determining Mach Number and Orientation in Hypersonic Inlets Using Absorption Spectroscopy," *AIAA Journal of Propulsion and Power*, doi: 10.2514/1.B35187, Article ahead of print.

[26] O'Byrne, S. and Wittig, S., Safer Air Travel: Laser Air Speed Sensor, URL: `http://unsw.technologypublisher.com/tech?title=Safer_Air_Travel%3A_Laser_Air_Speed_Sensor`, Last accessed: June 15, 2014.

[27] Kaminski-Morrow, D., "Airbus examines possible counter to erroneous airspeed data," URL: `http://www.flightglobal.com/news/articles/airbus-examines-possible-counter-to-erroneous-airspeed-354946/`, Last accessed: July 23, 2014.

[28] Walter, S., "Method and apparatus for the automatic estimation of airspeed of an aircraft," U.S Patent No: US 20130066488 A1 (March 14, 2013) E.U Patent No: EP2568295 B1 (January 15, 2014).

[29] Dodt, T., "Introducing the 787," *Proceedings of ISASI Annual Seminar*, Salt Lake City, UT, September 2011.

[30] Zeis, J. E., *Angle-of-Attack and Sideslip Estimation using Inertial Reference Platform*, Master's thesis, Air Force Institute of Technology, 1988.

[31] Murch, A., "A Flight Control System Architecture for the NASA AirSTAR Flight Test Infrastructure," *Proceedings of AIAA Guidance, Navigation, and Control Conference and Exhibit*, Honolulu, HI, August 2008, AIAA2008-6990.

[32] Colgren, R. D., "The Feasibility of using an INS for control system feedbacks," *1998 World Aviation Congress*, August 1998.

[33] Colgren, R. D., Frye, M. T., and Olson, W. M., "A proposed system architecture for estimation of angle of attack and sideslip angle," *Proceedings of AIAA Guidance, Navigation, and Control Conference and Exhibit*, August 1999, AIAA99-4078.

[34] Colgren, R. D. and Martin, K. E., "Flight Test validation of sideslip estimation using inertial accelerations," *Proceedings of AIAA Guidance, Navigation, and Control Conference and Exhibit*, August 2000, AIAA-2000-4448.

[35] Colgren, R. D., "Method and System for Elimination and Correction of Angle of Attack and Sideslip Angle from Acceleration Measurements," U.S Patent No: 6,273,370, 14 August 2001.

[36] Wise, K. A., "Computational Air Data System using Angle-of-Attack and Angle-of-Sideslip," U.S Patent No: 6,928,341, 9 August 2005.

[37] Wise, K. A., "Flight testing of the X-45A J-UCAS Computational Alpha-Beta System," *Proceedings of AIAA Guidance, Navigation, and Control Conference and Exhibit*, August 2006, AIAA2006-6215.

[38] Hemesath, N. B., "Optimum Complementation of VOR/DME with Air Data," *AIAA Journal of Aircraft*, Vol. 8, No. 6, June 1971, pp. 456–460.

[39] Bryson, A. E. and Bobick, J. C., "Improved Navigation by Combining VOR/DME Information and Air Data," *AIAA Journal of Aircraft*, Vol. 9, No. 6, June 1972, pp. 420–426.

[40] Berman, Z. and Powell, J. D., "The Role of Dead Reckoning and Inertial Sensors in Future General Aviation Navigation," *IEEE Position Location and Navigation Symposium*, Palm Springs, CA, 1998, pp. 510–517.

[41] Maybeck, P. S., *Stochastic models, estimation, and control Vol. 1*, Vol. 141-1 of *Mathematics in Science and Engineering*, NavTech Book & Software Store, USA, 1994.

[42] Etkin, B., *Dynamics of Atmospheric Flight*, Dover Publications, Mineola, NY, 2000.

[43] Groves, P. D., *Principles of GNSS, Inertial, and Integrated Navigation Systems*, Artech House, Norwood, MA, 2008.

[44] DeCleene, B., "Defining Pseudorange Integrity - Overbounding," *Proceedings of the 13th International Technical Meeting of the Satellite Division of The Institute of Navigation (ION GPS 2000)*, Salt Lake City, UT, September 2000, pp. 1916–1924.

[45] Rife, J., Pullen, S., Pervan, B., and Enge, P., "Paired overbounding and application to GPS augmentation," *Proceedings of IEEE Position Location and Navigation Symposium (PLANS)*, Monterey, CA, April 2004, pp. 436–446.

[46] Rife, J. and Gebre-Egziabher, D., "Symmetric Overbounding of Correlated Errors," *NAVIGATION, Journal of The Institute of Navigation*, Vol. 52, No. 2, 2007, pp. 109–124.

[47] Xing, Z. and Gebre-Egziabher, D., "Comparing Non-Linear Filters for Aided Inertial Navigators," *Proceedings of the 2009 International Technical Meeting of The Institute of Navigation*, Anaheim, CA, 2009, pp. 1048–1053.

[48] Xing, Z., *Over-bounding integrated INS/GNSS output errors*, Ph.D. thesis, Department of Aerospace Engineering and Mechanics, University of Minnesota, Minneapolis, MN, 2010.

[49] Simon, D., *Optimal State Estimation: Kalman, H_∞, and Nonlinear Approaches*, Wiley, 2006.

[50] Maybeck, P. S., *Stochastic models, estimation, and control Vol. 2*, Vol. 141-2 of *Mathematics in Science and Engineering*, NavTech Book & Software Store, USA, 1994.

[51] Klein, V. and Morelli, E. A., *Aircraft System Identification: Theory And Practice*, AIAA, 1st ed., August 2006.

[52] Maine, R. and Iliff, K., "Application of Parameter Estimation to Aircraft Stability and Control," NASA RP-1168, 1986.

[53] Jategaonkar, R. and Plaetschke, E., "Identification of Moderately Nonlinear Flight Mechanics System with Additive Process and Measurement Noise," *AIAA Journal of Guidance*, Vol. 13, No. 2, 1990, pp. 277–285.

[54] Klein, V., "Maximum Likelihood Method for Estimating Airplane Stability and Control Parameters from Flight Data in Frequency Domain," NASA TP-1637, 1980.

[55] Morelli, E. A., "Real-Time Parameter Estimation in the Frequency Domain," *AIAA Journal of Guidance, Control, and Dynamics*, Vol. 23, No. 5, 2000, pp. 812–818.

[56] Stengel, R. F., *Optimal Control and Estimation*, Dover Publications, 1994.

[57] Gleason, S. and Gebre-Egziabher, D., *GNSS Applications and Methods*, Artech House, Norwood, MA, 2009.

[58] Bevly, D. M. and Parkinson, B., "Cascaded Kalman Filters for Accurate Estimation of Multiple Biases, Dead-Reckoning Navigation, and Full State Feedback Control of Ground Vehicles," *IEEE Transactions on Control Systems Technology*, Vol. 15, No. 2, 2007, pp. 199–208.

[59] Friedland, B., "Treatment of Bias in Recursive Filtering," *IEEE Transactions on Automatic Control*, Vol. 14, No. 4, August 1969, pp. 359–367.

[60] Alouani, A. T., Xia, P., Rice, T. R., and Blair, W. D., "On the optimality of two-stage state estimation in the presence of random bias," *IEEE Transactions on Automatic Control*, Vol. 38, No. 8, August 1993, pp. 1279–1282.

[61] Haupt, G. T., Kasdin, N. J., Kaiser, G. M., and Parkinson, B. W., "Optimal recursive iterative algorithm for discrete nonlinear least-squares estimation," *AIAA Journal of Guidance, Control, and Dynamics*, Vol. 19, No. 3, May-June 1996, pp. 643–649.

[62] Titterton, D. H. and Weston, J. L., *Strapdown Inertial Navigation Technology*, Institution of Engineering and Technology, Stevenage, UK, 2004.

[63] Farrell, J. and Barth, M., *The Global Positioning System and Inertial Navigation*, McGraw-Hill Professional, 1999.

[64] Owens, D. B., Cox, D. E., and Morelli, E. A., "Development of a Low-cost Sub-Scale Aircraft for Flight Research: The FASER Project," *Proceedings of 25th AIAA Aerodynamic Measurement Technology and Ground Testing Conference*, San Francisco, CA, 2006, AIAA2006-3306.

[65] Kershner, D. D., "Miniature Flow-direction and Airspeed Sensor for Airplanes and Radio-controlled Models in Spin Studies," NASA TP-1467, 1979.

[66] –, University of Minnesota UAV Laboratory, URL: http://www.uav.aem.umn.edu, Last accessed 14 July 2012.

[67] Hoe, G., Owens, D. B., and Denham, C., "Forced Oscillation Wind Tunnel Testing for FASER Flight Research Aircraft," *Proceedings of AIAA Atmospheric Flight Mechanics Conference*, Minneapolis, MN, August 2012, AIAA2012-4645.

[68] Cashman, J., Kelly, B., and Nield, B., "Operational Use of Angle of Attack on Modern Commercial Jet Airplanes," *Boeing Aero Magazine*, Vol. 12, October 2000.

[69] Tjhai, C., *Developing stochastic model of thrust and flight dynamics for small UAVs*, Master's thesis, Department of Aerospace Engineering and Mechanics, University of Minnesota, Minneapolis, MN, 2013.

[70] –, UMN Flight Data Digital Conservancy, URL: http://conservancy.umn.edu/handle/11299/163580, Last accessed: 14 Aug 2014.